

**Signatures of Majorana bound states in the electronic  
transport through finite-size topological  
superconductors**

Von der Fakultät für Elektrotechnik, Informationstechnik, Physik  
der Technischen Universität Carolo-Wilhelmina zu Braunschweig

zur Erlangung des Grades eines Doktors

der Naturwissenschaften (Dr. rer. nat.)

genehmigte Dissertation

von Alexander Schuray

aus Salzgitter

eingereicht am: 03.11.2020

Disputation am: 17.03.2021

1. Referent: Prof. Dr. Patrik Recher

2. Referent: Prof. Dr. Andrey Surzhykov

Druckjahr: 2021

**Dissertation an der Technischen Universität Braunschweig,  
Fakultät für Elektrotechnik, Informationstechnik, Physik**

# Abstract

Majorana bound states (MBSs) offer a promising route to fault-tolerant quantum computation, because of their non-Abelian anyonic exchange statistics. They emerge as protected boundary modes of one dimensional topological superconductors (TSCs). Due to the finite size of these TSCs the wave functions of the two MBSs can spread across the whole TSC which leads to the possibility to access both MBSs at the same end of the TSC.

The goal of this thesis is to propose experimental signatures of the Majorana non locality in the context of electronic transport. The setups considered in this work are a metallic lead-TSC-quantum dot setup and a Josephson junction consisting of an  $s$ -wave superconducting lead and a Majorana nanowire.

In the case of the metallic lead-TSC-quantum dot setup we first consider a spinless system in which the Majorana system is described with a Kitaev chain. Here, we show that a pair of Fano resonances arises as a function of dot level energy in the differential conductance. In an analytical low-energy description, we show that in the case of isolated MBS, i.e. only one MBS is contacted by the lead and the second MBS is only contacted by the quantum dot, these Fano resonances are invariant under a sign change of the dot level energy. This symmetry, however, is broken as soon as we allow the quantum dot to not only couple to one but also to the second MBS. In a numerical analysis using the full Kitaev chain and long range hoppings between the Kitaev chain and the lead and dot, respectively, we confirm the low-energy findings.

Next, we consider a spinful model, in which the MBS system is given by a semiconducting nanowire with Rashba spin orbit interaction, proximity induced  $s$ -wave superconductivity and an applied Zeeman field. We also include Coulomb interaction on the quantum dot which we treat using a mean field approximation. In this scenario, we find that even without a coupling to the dot the transport properties can be used to determine the different couplings to both MBSs. Furthermore, we find that the spin canting angles of the MBSs have a profound influence on the low-energy transport properties. We underline our analytical findings with a numerical treatment of the proposed transport setup where we apply the mean field approximation for the Coulomb energy selfconsistently.

For the Josephson junction we use the quasidegenerate perturbation

---

theory to obtain an effective low-energy Hamiltonian. Our calculations show that the MBSs only contribute to the equilibrium Josephson current if both of them can be addressed by electron tunneling from the lead. Moreover, we find that the critical current is oscillating as a function of applied Zeeman field and exhibits a sign change at parity crossings. We can attribute these oscillations to the rotation of the spin of the MBS more distant to the junction. A numerical analysis reveals the contributions of higher energy states due to a residual *s*-wave pairing in the topologically non-trivial regime which shadow the signatures related to the MBSs. We therefore suggest an experimental scheme that uses quasiparticle poisoning to unveil the Majorana contributions.

# Zusammenfassung

Majorana bound states (MBSs) bieten aufgrund ihrer nicht-Abelschen anyonischen Austauschstatistik einen vielversprechenden Ansatz für einen fehlertoleranten Quantencomputer. Sie entstehen als geschützte Grenzzustände von eindimensionalen topologischen Supraleitern (TSCs). Aufgrund der endlichen Größe dieser TSCs kann sich die Wellenfunktion der beiden MBSs über den gesamten TSC ausbreiten, was zu der Möglichkeit führt, auf beide MBSs am gleichen Ende des TSC zuzugreifen.

Das Ziel dieser Arbeit ist es, experimentelle Signaturen der Majorana Nicht-Lokalität im Rahmen des elektronischen Transports vorzuschlagen. Die in dieser Arbeit betrachteten Setups sind eine metallische Zuleitung-TSC-Quantenpunktanordnung und ein Josephsonkontakt bestehend aus einem  $s$ -Wellen-Supraleiter und einem Majorana-Nanodraht. Im Falle der metallischen Zuleitung-TSC-Quantenpunktanordnung betrachten wir zunächst ein spinloses System, bei dem das Majorana-System mit einer Kitaev-Kette beschrieben wird. Hier zeigen wir, dass ein Paar Fano-Resonanzen als Funktion der Quantenpunktenergie in der differentiellen Leitfähigkeit entsteht. In einer analytischen Niederenergiebeschreibung zeigen wir, dass bei isolierten MBSs, d.h. nur ein MBS wird von der Leitung und der zweite MBS wird nur von dem Quantenpunkt kontaktiert, diese Fano-Resonanzen invariant unter einer Vorzeichenänderung der Quantenpunktenergie sind. Diese Symmetrie wird jedoch gebrochen, sobald wir zulassen, dass der Quantenpunkt nicht nur an ein, sondern auch an das zweite MBS gekoppelt wird. In einer numerischen Analyse mit der gesamten Kitaev-Kette und langweitreichenden Hüpftermen zwischen der Kitaev-Kette und der Leitung bzw. dem Quantenpunkte bestätigen wir die Ergebnisse des Niederenergiemodells.

Als nächstes betrachten wir ein Modell mit Spin, bei dem das MBS-System durch einen halbleitenden Nanodraht mit Rashba-Spinorbitwechselwirkung, induzierter  $s$ -Wellen Supraleitung und einem angelegten Zeeman-Feld gegeben ist. Wir betrachten auch die Coulombwechselwirkung auf dem Quantenpunkt, die wir mit einer Molekularfeldnäherung beschreiben. In diesem Szenario stellen wir fest, dass auch ohne Kopplung an den Quantenpunkt die Transporteigenschaften genutzt werden können, um die unterschiedlichen Kopplungen zu beiden MBSs zu bestimmen. Darüber hinaus stellen wir fest, dass die Spinrotationswinkel der MBSs einen wesentlichen Einfluss auf die Eigenschaften des Niedrigenergietrans-

---

ports haben. Wir unterstützen unsere analytischen Ergebnisse mit einer selbstkonsistenten numerischen Behandlung des vorgeschlagenen Transportsetups.

Für den Josephsonkontakt verwenden wir die quasientartete Störungstheorie, um einen effektiven niederenergetischen Hamiltonoperator zu erhalten. Unsere Berechnungen zeigen, dass die MBSs nur dann zum Gleichgewichts-Josephsonstrom beitragen, wenn beide durch Elektronentunneln von der Zu- leitung adressiert werden können. Darüber hinaus stellen wir fest, dass der kritische Strom in Abhängigkeit vom angelegten Zeeman-Feld oszilliert und eine Vorzeichenänderung an Paritätsübergängen erfährt. Wir können diese Oszillationen auf die Drehung des Spins des MBS, der weiter vom Übergang entfernt ist, zurückführen. Eine numerische Analyse zeigt zusätzliche Beiträge höherer Energiezustände aufgrund einer verbleibenden  $s$ -Wellenpaarung im topologisch nicht-trivialen Regime, die die Signaturen im Zusammenhang mit den MBSs überschatten. Wir schlagen daher ein experimentelles Schema vor, das die Majorana-Beiträge durch Quasiteilchen-Vergiftung enthüllt.

# Acknowledgements

First, I want to thank Prof. Dr. Patrik Recher for giving me the opportunity to work on this subject matter. We had a lot of interesting and fruitful discussions that extended my physical understanding a lot. Without his guidance this dissertation would not have been possible.

Next, I would like to thank Prof. Dr. Andrey Surzhykov for coreferencing this thesis and Prof. Dr. Uta Schlickum for chairing my PhD-committee.

I also want to especially thank Dr. Luzie Weihofer, Prof. Dr. Alfredo Levy-Yeyati, Daniel Frombach, Dr. Sunghun Park and Manuel Rammner who were directly involved in projects that led to the creation of this thesis.

Another special thank you goes out to all the members of the NTH school for contacts in nanosystems, the research training group nanomet and BIGSM. You all helped me to extend my knowledge beside the specialized topic that this thesis is about and I appreciate the extra curricular time we spend together.

To my colleagues and friends in the physics department, you made my stay worthwhile and I will miss our fun activities and discussions about not only physics related topics. I want to especially point out Conny whose help made it possible to focus on my scientific activities without worrying about bureaucratic obstacles and who always had a open ear during my tea sessions. A special thank you also goes out to my office mates Bene, Lena and Fernando. I really enjoyed our small chats, coffee breaks and quick discussions that often resolved small problems immediately.

It goes without saying that I am deeply indebted to all my friends and family for their continous care and support.

Last but not least, I need to say that everything I did would be unthinkable without Steffi.





## List of Publications

- *Fano resonances in Majorana bound states-quantum dot hybrid systems*, A. Schuray, L. Weithofer, and P. Recher Phys. Rev. B **96**, 085417 (2017)
- *Influence of the Majorana nonlocality on the supercurrent*, A. Schuray, A. L. Yeyati, and P. Recher Phys. Rev. B **98**, 235301 (2018)
- *Transport signatures of Majorana bound states in superconducting hybrid structures*, A. Schuray, D. Frombach, S. Park, and P. Recher Eur. Phys. J. Special Topics **229**, 593 (2020)
- *Signatures of the Majorana spin in electrical transport through a Majorana nanowire*, A. Schuray, M. Rammner and P. Recher Phys. Rev. B **102**, 045303 (2020)

## List of Conference Contributions

- *Fano Resonances in Majorana Bound State - Quantum Dot Systems*, A. Schuray, L. Weithofer, and P. Recher, Workshop Topological States of Matter, San Sebastian, 05. - 09. September 2016 (Poster)
- *Fano resonances in transport through Majorana networks*, A. Schuray, L. Weithofer, and P. Recher, DPG Spring meeting, Dresden, 19. - 24. March 2017 (Talk)
- *Fano resonances in transport through Majorana networks*, A. Schuray, L. Weithofer, and P. Recher, Quantum Transport in Topological Materials, Miraflores de la Sierra, 04. - 08. September 2017 (Poster)
- *Influence of the Majorana nonlocality on the supercurrent*, A. Schuray, A. Levy Yeyati, and P. Recher, DPG Spring meeting, Berlin, 11. - 16. March 2018 (Talk)
- *Influence of the Majorana nonlocality on the supercurrent*, A. Schuray, A. L. Yeyati, and P. Recher, The Capri Spring School on Transport in Nanostructures, 15. - 22. April 2018 (Talk)

- 
- *Fano resonances in spinful Majorana bound state - quantum dot hybrid system*, A. Schuray, and P. Recher, DPG Spring meeting, Regensburg, 31. March - 05. April 2019 (Talk)
  - *Transport through coupled Majorana bound states*, A. Schuray, and P. Recher, Quantum Designer Physics, San Sebastian, 01. - 04. July 2019 (Poster)

# Contents

<b>1. Introduction</b>	<b>1</b>
1.1. Topological superconductivity . . . . .	3
1.1.1. The notion of topology in condensed matter systems	4
1.1.2. Superconductivity - Bogoliubov-de Gennes formalism	5
1.1.3. Majorana modes in topological superconductors . . .	8
1.2. About this thesis . . . . .	20
<b>2. Fano resonances in spinless Majorana bound states-quantum dot system</b>	<b>23</b>
2.1. Setup and Andreev Reflection Probability . . . . .	25
2.2. Fano Resonances . . . . .	29
2.3. Kitaev Chain Calculations . . . . .	33
2.4. Nonlocal Couplings . . . . .	37
2.4.1. Analytical Calculations . . . . .	37
2.4.2. Long-range Couplings to the Kitaev Chain . . . . .	40
2.5. Conclusion . . . . .	43
<b>3. Signatures of the Majorana spin in the electrical transport in a Majorana nanowire</b>	<b>45</b>
3.1. Full Model Hamiltonian . . . . .	47
3.2. Low Energy Effective Model . . . . .	49
3.2.1. Cumulant Generating Function . . . . .	51
3.2.2. Transport without quantum dot . . . . .	52
3.2.3. Transport properties with quantum dot . . . . .	59
3.3. Numerical scattering matrix formalism for the full wire model	63
3.3.1. Without dot . . . . .	64
3.3.2. Self consistent mean field approach for the quantum dot . . . . .	67
3.4. Conclusion . . . . .	71

<b>4. The influence of the Majorana non-locality on the supercurrent</b>	<b>73</b>
4.1. Model . . . . .	76
4.2. Low energy effective system . . . . .	79
4.3. High energy contributions . . . . .	82
4.4. Numerical results . . . . .	84
4.4.1. Finite size Majorana nanowire . . . . .	84
4.4.2. Josephson current and experimental realization . . .	87
4.5. Conclusion . . . . .	89
<b>5. Summary and Conclusion</b>	<b>91</b>
<b>A. Derivation of the Levitov-Lesovik formula</b>	<b>95</b>
<b>B. Calculation of the unperturbed Majorana Green's function</b>	<b>101</b>
<b>C. Quasi-degenerate perturbation theory</b>	<b>105</b>
<b>D. Calculations of Majorana wave function</b>	<b>109</b>

# 1. Introduction

In his 1982 keynote speech “Simulating Physics with Computers” Richard Feynman asks two important questions “Can physics be simulated by a universal computer?” and “Can a quantum system be probabilistically simulated by a classical (probabilistic, I’d assume) universal computer?” [1]. His answer to the second question is plainly “certainly, No!”, because it is a so-called hidden-variable problem. To answer the first question it is important to note that the physical world is a quantum mechanical world. In general, the number of variables describing a quantum system grows exponentially with the number of particles  $N$  so that a classical computer with  $N$  number of elements cannot be used to efficiently simulate the quantum system, but  $N$  quantum computer elements could be. In my opinion, this is the most important use of quantum computer elements, because it allows us to dive deeply in interacting models which could lead to new advances in material science.

Recently, the researcher team around John M. Martinis was able to show quantum supremacy [2]. Quantum supremacy means that they were able to perform a computation task, for which a state-of-the-art classical computer would need thousands of years [3]. Even though the specific computational task they performed has so far no practical application, it is an important milestone in the realization of a universal quantum computer.

The fundamental quantum computer elements needed to construct a working quantum computer are called qubits and they are the quantum analogon to the classical bits. Principally, the qubit is a quantum mechanical two-level system described by the two orthogonal computation basis states  $|0\rangle$  and  $|1\rangle$  [4]. Because quantum mechanics allows for superpositions of these states and also for entanglement the Hilbert space of  $N$  of these qubits becomes exponentially large. The evolution of the qubits is performed by quantum gates, unitary operations that can perform any desired state transformation. In order to build a quantum computer physical realizations of these qubits should be scalable, a state of the qubit has to

## 1. Introduction

---

be initialized, coherence time need to be large compared to gate operation times, a universal set of gates is needed and a qubit-specific measurement capability [5]. These criteria are also known as DiVincenzo criteria.

There are several experimental approaches to creating qubits that satisfy the DiVincenzo criteria. For example the spin of a single electron in a quantum dot [6, 7]. Here, the spin direction (e.g. up and down) correspond to the two computational basis states. Another physical realization involving spin is quantum computation based on atomic nuclei [8], nitrogen-vacancy centers in diamonds [9] or molecular magnets [10]. It is also possible to use the charge states of a double quantum dot (i.e. the position of the electron) as a qubit [11]. The route that the researcher team around John M. Martinis chose was to use superconducting qubits, where the qubit is implemented using small Josephson junctions [12, 13]. These are just a few examples of the proposed realizations of qubits for quantum computation [14]. The main problems that need to be overcome are that errors might enter the system either in the form of inaccuracies of experimental control or uncontrollable perturbations from the environment [15]. A solution for this obstacle is error correction codes that have already been developed [16, 17] that at least theoretically allow for meaningful quantum information processing. But still, full scale quantum computing is not within reach of current state-of-the-art experiments, so that there is still a lot of research directed at new ways of creating and manipulating qubit states.

An interesting way to achieve fault-tolerant quantum computation is to use the exchange statistics of non-Abelian anyons [15, 18]. If these anyons would be elementary particles they would be robust up to high energy scales and therefore the quantum information encoded in their fusion Hilbert space would be resilient and error-free quantum computation could be performed straightforwardly. However, in reality they are realized as emergent quasiparticles in topological systems which makes them still somewhat robust. They are protected from probabilistic errors (e.g. due to finite temperature) by the presence of a finite excitation energy gap. Also, because the information is encoded non-locally in these systems, environmental errors that act as local perturbations to the Hamiltonian are drastically reduced [19] as long as the anyons are kept far apart. In addition, the exotic exchange statistics of these anyons can be exploited to perform unitary gate operations by simple exchange operations where the concrete realization of the exchange path does not matter (as long

as the anyons remain far apart) only its topology [15]. Because of this, these topological quantum gates are very robust. But, not all non-Abelian anyons have the needed complexity in their exchange statistic to realize a universal set of gates. Missing gates then need to be introduced via topologically non-protected and therefore possible quite noisy gates [20].

Early proposal for quantum computing with non-Abelian anyons was based on the  $\nu = 5/2$  fractional quantum Hall state [21, 22]. Other non-Abelian states that were in the focus of much research in the last years are Majorana zero modes that are predicted to arise as emergent quasiparticles in topological superconductors [23–28]. Aside from their useful application in topological quantum computation schemes they also have the interesting fundamental property that these quasiparticles are also their own anti-particles [29]. In order to use these Majorana zero modes for topological quantum computation, their existence and their fundamental properties need to be established. The goal of this thesis is to contribute proposals for detection schemes for these Majorana modes with an emphasis on the fact that in any experimental realization the non-Abelian Majorana quasiparticles are not infinitely spaced from one another but that finite size effects can have a major role in their electronic transport signatures.

In the remainder of this introductory chapter, we introduce the concept of topology in condensed matter systems and cover the basics of creation, characterization and manipulation of Majorana bound states (MBSs). A full review of topological quantum computation and all details about Majorana fermions are beyond the scope of this thesis, however this introductory chapter will contextualize the findings of the succeeding chapters. The results of the works presented in the main part of this thesis are summarized in Sec. 1.2.

## 1.1. Topological superconductivity

In this chapter, we introduce the basic concepts behind the creation, characterization and manipulation of MBSs. We first start with a general introduction of topological materials, before focusing on topological superconductors and the emergence of MBSs. We also give a brief overview of how to use MBS for topological quantum computation schemes.

## 1. Introduction

---

### 1.1.1. The notion of topology in condensed matter systems

In mathematics topology is used to classify shapes. Two shapes are said to have the same topology if they can be continuously transformed into each other. The mathematical concept of topology can also be transferred to quantum mechanical wave functions and the Nobel prize 2016 was given to Thouless, Kosterlitz and Haldane for the theoretical discoveries of topological phase transitions and topological phases of matter [30]. These topological phase transitions are special in the sense that no spontaneous symmetry breaking is associated with them [31]. In addition, to this fundamental feature topological phases of matter are highly robust. In general, the topology of a given object is characterized by an integer number, the topological invariant. And because it is integer it cannot be changed continuously.

The first quantum mechanical system to be recognized to have a non-trivial topology was the quantum Hall effect. Non-trivial in this context means that its topology is distinct from that of the vacuum which is considered to have the trivial topology. Thouless, Kohomoto, Nightingale and de Nijs discovered that the quantum Hall state can be characterized by the TKNN number [32] a topological invariant. Later it was shown that the TKNN number can be derived in the form of the Chern number [33].

Another interesting feature of topological materials is the so called bulk-boundary correspondence. It connects the existence of boundary modes with the topological invariant which is a bulk property. In the case of quantum Hall systems these boundary modes are one-dimensional chiral edge modes that lead to ballistic transport along the edges of a given quantum Hall sample [34]. In general, the boundaries at which these states emerge are boundaries where the topological invariant changes.

To determine the topology of a quantum state it is very important to consider the symmetry of the underlying Hamiltonian. For example with no assumed symmetry the only possible topological non-trivial state in up to three dimensions is the quantum Hall state which is characterized by a nonzero Chern number [35]. For the combination (or lack) of the discrete symmetries particle-hole, chiral and time-reversal symmetry exists a classification of topological invariants for arbitrary dimensions, the so called periodic table of topological invariants [36]. For example in a two dimensional system with only time-reversal symmetry  $\mathcal{T}^2 = -1$  where



$\mathcal{T}$  is the time-reversal operator the topological invariant is a  $\mathbb{Z}_2$  number [37–39]. In addition, spatial symmetries (crystal symmetries) can also lead to topological phases. Material systems with these properties are called topological crystalline insulators [40]. A combination of temporal and spatial symmetries can lead to so called higher-order topological insulators [41–44]. These higher-order topologies in  $d$ -dimensional systems lead to  $(d - 2)$ -dimensional boundary modes (for three-dimensional systems these are hinge modes and for two-dimensional systems these are corner modes).

All the so far discussed topological systems have in common that they have a distinct ground state that is separated from the excited states by an energy gap. The topology of these system can only be changed when this gap closes. Thus, the gap also protects the topological boundary modes. We want to note here, that also gapless topological materials exist for example Weyl semimetals or Dirac semimetals [45].

### 1.1.2. Superconductivity - Bogoliubov-de Gennes formalism

Before discussing the properties of topological superconductors, we take a step back and focus on the essential features of superconductivity itself. Superconductivity arises in the presence of an attractive interaction between two electrons. The single band Hamiltonian for an appropriate interaction in momentum space is

$$H = \sum_{\mathbf{k}, s_1, s_2} \varepsilon_{s_1 s_2}(\mathbf{k}) c_{\mathbf{k} s_1}^\dagger c_{\mathbf{k} s_2} \quad (1.1)$$

$$+ \frac{1}{2} \sum_{\mathbf{k}, \mathbf{k}', s_1, s_2, s_3, s_4} V_{s_1 s_2 s_3 s_4}(\mathbf{k}, \mathbf{k}') c_{-\mathbf{k} s_1}^\dagger c_{\mathbf{k} s_2}^\dagger c_{\mathbf{k}' s_3} c_{-\mathbf{k}' s_4},$$

where  $c_{\mathbf{k} s}^\dagger$  creates an electron with spin  $s$  and momentum  $\mathbf{k}$ , and  $\varepsilon_{s_1 s_2}(\mathbf{k})$  is the band Hamiltonian which is a  $2 \times 2$  matrix in spin space. Its spin dependence can arise for example from spin orbit coupling [46, 47]. In mean field approximation the Hamiltonian becomes [48]

$$H = \sum_{\mathbf{k}, s_1, s_2} \varepsilon_{s_1 s_2}(\mathbf{k}) c_{\mathbf{k} s_1}^\dagger c_{\mathbf{k} s_2} + \frac{1}{2} \sum_{\mathbf{k}, s_1, s_2} \left[ \Delta_{s_1 s_2}(\mathbf{k}) c_{\mathbf{k} s_1}^\dagger c_{-\mathbf{k} s_2}^\dagger + h.c. \right], \quad (1.2)$$

## 1. Introduction

---

where we introduced the pair potential  $\Delta_{s_1 s_2}(\mathbf{k}) = -\sum_{\mathbf{k}', s_3, s_4} V_{s_1 s_2 s_3 s_4}(\mathbf{k}, \mathbf{k}') \langle c_{\mathbf{k}' s_3} c_{-\mathbf{k}' s_4} \rangle$ . This pair potential obeys the relation  $\Delta_{s_1 s_2}(\mathbf{k}) = -\Delta_{s_2 s_1}(-\mathbf{k})$ , because of the Fermi statistics of  $c_{\mathbf{k}s}$ . The mean field Hamiltonian no longer conserves the particle number, however the parity (the number of electrons modulo 2) is still a conserved quantity. The Hamiltonian (1.2) can be rewritten conveniently in matrix form

$$H = \frac{1}{2} \sum_{\mathbf{k}, s_1, s_2} (c_{\mathbf{k}s_1}^\dagger, c_{-\mathbf{k}s_2}) \mathcal{H}_{BdG} \begin{pmatrix} c_{\mathbf{k}s_2} \\ c_{-\mathbf{k}s_2}^\dagger \end{pmatrix} \quad (1.3)$$

with

$$\mathcal{H}_{BdG}(\mathbf{k}) = \begin{pmatrix} \varepsilon_{s_1 s_2}(\mathbf{k}) & \Delta_{s_1 s_2}(\mathbf{k}) \\ \Delta_{s_1 s_2}(\mathbf{k})^\dagger & -\varepsilon_{s_1 s_2}^T(-\mathbf{k}) \end{pmatrix}. \quad (1.4)$$

To arrive at this matrix form we neglected a constant energy shift. This matrix form now obeys the particle-hole symmetry

$$\mathcal{C} \mathcal{H}_{BdG}(\mathbf{k}) \mathcal{C}^{-1} = -\mathcal{H}_{BdG}(-\mathbf{k}), \quad (1.5)$$

with the anti-unitary operator

$$\mathcal{C} = \begin{pmatrix} 0 & \mathbf{I}_{2 \times 2} \\ \mathbf{I}_{2 \times 2} & 0 \end{pmatrix} K, \quad (1.6)$$

and  $K$  the complex conjugation operator. This symmetry arises because of the redundancy within the Hamiltonian. That redundancy comes from the fact that the components of  $(c_{\mathbf{k}s_1}^\dagger, c_{-\mathbf{k}s_1})$  are not independent, but are connected via hermitian conjugation which is of course reflected in the Hamiltonian.

The eigenvalue problem

$$\mathcal{H}_{BdG}(\mathbf{k}) \Psi(\mathbf{k}) = E(\mathbf{k}) \Psi(\mathbf{k}) \quad (1.7)$$

is called Bogoliubov-de Gennes (BdG) equation. The previous mentioned particle-hole symmetry also leads to

$$\mathcal{H}_{BdG}(\mathbf{k}) \mathcal{C} \Psi(-\mathbf{k}) = -E(-\mathbf{k}) \mathcal{C} \Psi(-\mathbf{k}), \quad (1.8)$$

which means that the eigenenergies  $E(\mathbf{k})$  and  $-E(-\mathbf{k})$  come in pairs. And for every solution of the BdG equation  $\psi = (u_\uparrow(\mathbf{k}), u_\downarrow(\mathbf{k}), v_\uparrow^*(-\mathbf{k}), v_\downarrow^*(-\mathbf{k}))^T$

## 1.1. Topological superconductivity

there is a particle-hole conjugate partner  $\mathcal{C}\psi$  that is also a solution of the BdG equation. The four eigenvalues of the  $4 \times 4$  BdG Hamiltonian are therefore  $(E_1(\mathbf{k}), E_2(\mathbf{k}), -E_1(-\mathbf{k}), -E_2(-\mathbf{k}))$  with  $E_i(\mathbf{k}) \geq 0$ . Without loss of generality, it is enough to focus on the positive energy solutions (because of the artificial doubling of degrees of freedom). If we diagonalize the Hamiltonian and reenter the solutions  $\psi^{(i)}(\mathbf{k})$  that correspond to the energy  $E_i(\mathbf{k})$  into Eq. (1.3) we obtain

$$H = \sum_{\mathbf{k}, i} E_i(\mathbf{k}) \gamma_{\mathbf{k}i}^\dagger \gamma_{\mathbf{k}i}, \quad (1.9)$$

where

$$\gamma_{\mathbf{k}i} = \sum_s \left( u_s^{(i)*}(\mathbf{k}) c_{\mathbf{k}s} + v_s^{(i)}(-\mathbf{k}) c_{-\mathbf{k}s}^\dagger \right), \quad (1.10)$$

describe the quasiparticle excitations with energy  $E_i(\mathbf{k})$ . These quasiparticles are called Bogoliubov quasiparticles. The two energy bands ( $i = 1, 2$ ) reflect the two spin degrees of freedom in the Hamiltonian we started with. The operators  $\gamma_{\mathbf{k}i}$  obey the fermionic anti-commutation relation and for the ground state of the superconductor  $|0\rangle$  we find

$$\gamma_{\mathbf{k}i} |0\rangle = 0, \quad (1.11)$$

which implies that all negative energy states are occupied.

The BdG equation also allows us to introduce a boundary to the system straight forwardly. By replacing  $\mathbf{k}$  with  $-i\partial_{\mathbf{x}}$  the BdG equation becomes a differential equation

$$\mathcal{H}_{BdG}(-i\partial_{\mathbf{x}}) \begin{pmatrix} u_\uparrow(\mathbf{x}) \\ u_\downarrow(\mathbf{x}) \\ v_\uparrow^*(\mathbf{x}) \\ v_\downarrow^*(\mathbf{x}) \end{pmatrix} = E \begin{pmatrix} u_\uparrow(\mathbf{x}) \\ u_\downarrow(\mathbf{x}) \\ v_\uparrow^*(\mathbf{x}) \\ v_\downarrow^*(\mathbf{x}) \end{pmatrix}, \quad (1.12)$$

where a boundary condition can be introduced for example as

$$\begin{pmatrix} u_\uparrow(\mathbf{x}_0) \\ u_\downarrow(\mathbf{x}_0) \\ v_\uparrow^*(\mathbf{x}_0) \\ v_\downarrow^*(\mathbf{x}_0) \end{pmatrix} = 0. \quad (1.13)$$

Another advantage is that this equation now can also include position dependent potentials by including them into  $\varepsilon_{s_1 s_2}(-i\partial_{\mathbf{x}})$ . It is also possible

## 1. Introduction

---

to include defects by extending  $\Delta_{s_1 s_2}(-i\partial_{\mathbf{x}}) \rightarrow \Delta_{s_1 s_2}(-i\partial_{\mathbf{x}}, \mathbf{x})$ . Furthermore, the BdG equation allows us to use a lattice model in order for us to consider a boundary. We can discretize the real space and the real space derivative, which leads to a tight binding version of the BdG equation that we can solve on a computer effectively. We also want to note here that bound states can arise at these boundaries or defects. These bound states are generally called Andreev bound states.

The Cooper pairs that form because of the attractive interaction are formed from two spin 1/2 particles. Therefore, they can either be in a spin-singlet (spin angular momentum 0) or a spin-triplet (spin angular momentum 1) configuration. This is then also transferred to the pairing potential  $\Delta_{s s'}(\mathbf{k})$ . It is antisymmetric in spin space for spin-singlet Cooper pairs and symmetric in spin space for spin-triplet Cooper pairs. In analogy with the classification of atomic orbitals, superconductors with Cooper pairs with orbital angular momentum of  $l = 0, 1, 2, 3$  are called *s*-wave, *p*-wave, *d*-wave and *f*-wave superconductors, respectively.

### 1.1.3. Majorana modes in topological superconductors

Ettore Majorana showed that real solutions to the Dirac equations are possible as he found a suitable set of  $4 \times 4$  matrices with pure imaginary components that also obey the Clifford algebra [49]. Fermions described by these real fields have the interesting property that they are their own antiparticle, because particle and anti-particle are connected via a complex conjugation of their respective fields. In second quantization this would correspond to self-hermitian creation operators for Majorana fermions  $\gamma = \gamma^\dagger$ . Because particle and antiparticle have opposite charge, these Majorana fermions thus have to have zero charge. Currently, it is suspected that neutrinos might be Majorana fermions, however the double beta decay that could underline this hypothesis was not yet observed [50].

The need for this chargelessness provides a challenge for the search of Majorana fermion like excitations in condensed matter. Because both electrons and holes which are the building blocks of collective excitations in condensed matter are charged with opposite charge  $\pm e$  [50]. A Majorana excitation has to be a coherent superposition of an electron and a hole. As seen in the previous section (cf. Eq (1.10)) the Bogulibov excitations in superconductors can serve this purpose. This can be understood

because the number of Cooper pairs is not fixed in the mean field description, so that the difference between an electron and a hole gets blurry. However, the conventional superconductors are  $s$ -wave superconductors with spin-singlet Cooper pairs. Their Bogoliubov excitations are of the form of  $\gamma_1 = uc_{\uparrow} + vc_{\downarrow}^{\dagger}$  which even for  $u = v$  are no Majorana fermions, because of the spin degree of freedom.

Systems in which this problem could be solved are  $p$ -wave superconductors, because the Cooper pairs in those form spin-triplets. It can be shown that the Andreev bound states that are pinned to vortices in two dimensional  $p$ -wave superconductors are indeed Majorana bound states [51]. Experimentally, the  $p$ -wave superconductivity can be realized by proximity inducing superconductivity in the surface state of a three-dimensional topological insulator by using a conventional  $s$ -wave superconductor [52]. In this thesis however, we focus on the Majorana excitations that emerge at the boundary of one-dimensional topological superconductors.

A one dimensional  $p$ -wave superconductor was discussed first by Kitaev [29]. Kitaev considered a spinless fermionic tight binding chain with a superconducting pairing of nearest neighbors. It is described with the Hamiltonian

$$H = - \sum_{j=1}^N \mu \left( c_j^{\dagger} c_j - \frac{1}{2} \right) + \left( \sum_{j=1}^{N-1} -t c_j^{\dagger} c_{j+1} + \Delta e^{-i\varphi} c_j^{\dagger} c_{j+1}^{\dagger} + h.c. \right), \quad (1.14)$$

where  $c_j^{\dagger}$  creates an electron at site  $j$ ,  $\mu$  is the chemical potential,  $t$  the hopping amplitude and  $\Delta$  is the superconducting pairing amplitude. It is convenient to gauge the phase of the superconductor  $\varphi$  into the creation operators  $c_j \rightarrow e^{-i\varphi/2} c_j$ . We transform the fermionic creation and annihilation operators into Majorana operators with the transformation

$$c_j = \frac{1}{2} (\gamma_{Aj} + i\gamma_{Bj}), \quad (1.15)$$

where  $\gamma_{nj}^{\dagger} = \gamma_{nj}$  with  $n = A, B$ . Because of the fermionic anti-commutation relation for the electron creation and annihilation operators the anti-commutation relation for the Majorana operators is given by

$$\{\gamma_{nj}, \gamma_{mk}\} = 2\delta_{nm}\delta_{jk}. \quad (1.16)$$

## 1. Introduction

---

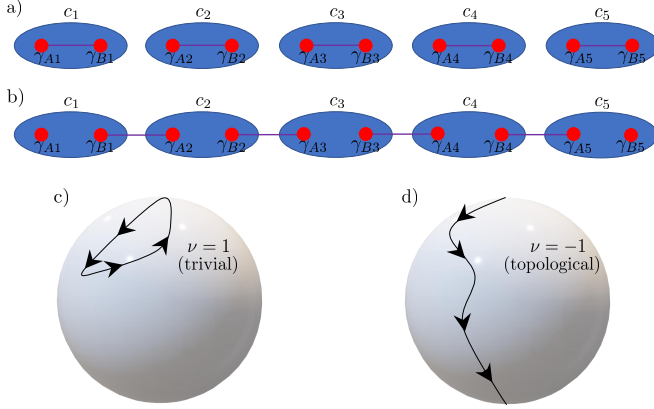


**Figure 1.1.:** a) & b) Visual representation of a 5 site Kitaev chain at the trivial (see a)) and topological (see b)) sweet spots discussed in the text. The blue ovals represent a fermionic site, while the red circles correspond to the Majorana operators. The purple lines stand for the interactions between the Majorana operators at the sweet spots. c) & d) Schematic diagram for the Kitaev chain Hamiltonian with periodic boundary conditions. Figure adapted from [23]

## 1.1. Topological superconductivity

---

If we use this transformation we can rewrite the Hamiltonian in terms of Majorana operators

$$H = -\frac{i}{2} \sum_{j=1}^N \mu \gamma_{Aj} \gamma_{Bj} + \frac{i}{2} \sum_{j=1}^{N-1} (t + \Delta) \gamma_{Bj} \gamma_{Aj+1} + (-t + \Delta) \gamma_{Aj} \gamma_{Bj+1}.$$

Here, we want to discuss two special cases that are depicted in Fig. 1.1 a) and b). First, we consider the case  $\mu \neq 0$  and  $t = \Delta = 0$ . In this trivial case the Hamiltonian is given by

$$H|_{\mu \neq 0, t=\Delta=0} = -\frac{i}{2} \sum_{j=1}^N \mu \gamma_{Aj} \gamma_{Bj}. \quad (1.17)$$

As also seen in Fig. 1.1 a) this Hamiltonian couples only the Majorana operators on the same fermionic site. Also, all Majorana operators are coupled. The other more interesting case is  $\mu = 0$  and  $t = \Delta \neq 0$ . This scenario is depicted in Fig. 1.1 b). The Hamiltonian in this case is

$$H|_{\mu=0, t=\Delta \neq 0} = i \sum_{j=1}^{N-1} t \gamma_{Bj} \gamma_{Aj+1}. \quad (1.18)$$

Here, two Majorana operators (one on the first and one on the last site) are left uncoupled. Because they no longer enter the Hamiltonian they commute with the Hamiltonian and span a zero-energy two-fold degenerate ground state manifold. These two states are the Majorana bound states. Together the two MBSs form a non-local fermionic degree of freedom. Away from this sweet spot MBSs can still be found, however they are no longer completely localized at the last site. The wave function rather decays exponentially along the chain. This also leads to a finite energy splitting  $\varepsilon \propto e^{-iL/\xi_M}$ , where  $\xi_M$  is the Majorana localization length [29]. In this case the low-energy sector of the Hamiltonian can be described with two Majorana operators  $\gamma'$  and  $\gamma''$  that are a superposition of the former Majorana operators

$$H = i\varepsilon \gamma' \gamma''. \quad (1.19)$$

To understand why the MBS persist away from the sweet spot, we take a look at the topology of the system. Therefore we consider periodic

## 1. Introduction

---

boundary conditions and take a look at the Hamiltonian in reciprocal space. In the BdG formalism the Hamiltonian in reciprocal space takes the form

$$H = \frac{1}{2} \sum_{k \in BZ} \begin{pmatrix} c_k^\dagger & c_{-k} \end{pmatrix} \mathcal{H}_k \begin{pmatrix} c_k \\ c_{-k}^\dagger \end{pmatrix}, \quad (1.20)$$

$$\mathcal{H}_k = \begin{pmatrix} -t \cos k - \mu & i\Delta \sin k \\ -i\Delta \sin k & t \cos k + \mu \end{pmatrix}.$$

Now, let us discuss a possible topological invariant. Here, we follow the strategy outlined in Ref. [23]. The  $2 \times 2$  BdG Hamiltonian can also be written in the form of

$$\mathcal{H}_k = \mathbf{h}(k) \cdot \boldsymbol{\sigma}, \quad (1.21)$$

where  $\boldsymbol{\sigma} = \sigma_x \mathbf{e}_x + \sigma_y \mathbf{e}_y + \sigma_z \mathbf{e}_z$  is the vector of Pauli matrices and  $\mathbf{h}(k)$  is also a three component vector. Because of the particle-hole symmetry inherent to the spinless BdG formalism  $\mathbf{h}(k)$  needs to fulfill the following relations

$$h_{x,y}(k) = -h_{x,y}(-k), \quad h_z(k) = h_z(-k). \quad (1.22)$$

Let us suppose now, that the system is completely gapped, i.e.  $\mathbf{h}(k)$  is non-zero all over the Brillouin zone. Then we can define the normalized vector  $\hat{\mathbf{h}}(k) = \mathbf{h}(k)/|\mathbf{h}(k)|$  to map the Brillouin zone onto the unit sphere which is schematically shown in Fig. 1.1 c) and d). By using the relations from Eq. (1.22) one finds that

$$\hat{\mathbf{h}}(0) = s_0 \mathbf{e}_z, \quad \hat{\mathbf{h}}(\pi) = s_\pi \mathbf{e}_z, \quad (1.23)$$

where  $s_0$  and  $s_\pi$  are the sign of the kinetic energy measured relatively to the Fermi level at momentum 0 and  $\pi$ , respectively. For the product of these signs  $\nu = s_0 s_\pi$  there are two fundamentally different results. As shown in Fig. 1.1 c) for  $\nu = 1$ ,  $\hat{\mathbf{h}}(0)$  and  $\hat{\mathbf{h}}(\pi)$  point in the same direction, so that  $\hat{\mathbf{h}}(k)$  completes a circle on the interval  $[0, \pi]$ . In contrast for  $\nu = -1$ ,  $\hat{\mathbf{h}}(0)$  and  $\hat{\mathbf{h}}(\pi)$  point in the opposite directions, which is shown in Fig. 1.1 d). The two trajectories on the unit sphere are therefore topologically distinct which makes  $\nu$  a  $\mathbb{Z}_2$  topological index. The only way to change the topology is to close the gap, because then  $\hat{\mathbf{h}}(k)$  is not defined on the complete Brillouin zone. For the Kitaev chain that means that as long as  $|\mu| < |t|$  the chain is in the topologically non-trivial phase



with MBS at the ends of the chain. We note here, that the discussion of the topological index is valid, even if we allow for perturbations in the Hamiltonian as long as the particle-hole symmetry is present.

In general, the Kitaev chain is not readily realized in nature, as all electrons carry a spin degree of freedom. A fully spin polarized system is also very unlikely to realize a Kitaev chain, because most superconductors found in nature host spin-singlet Cooper pairs. However, the *s*-wave superconductors can be used to induce superconductivity in other materials via the superconducting proximity effect.

It was pointed out that semiconducting nanowires with Rashba spin-orbit coupling with proximity induced superconductivity can realize a topologically non-trivial phase, when a strong enough Zeeman field is applied [53, 54]. These nanowires are also dubbed Majorana nanowires. Let us first consider this system without the proximity induced superconductivity. In this case the Hamiltonian describing the nanowire in the effective mass approximation in reciprocal space is

$$H_W = \int dk \left( \psi_{\uparrow k}^\dagger, \psi_{\downarrow k}^\dagger \right) \left( \frac{\hbar^2 k^2}{2m^*} - \mu + \alpha k \sigma_y + V_Z \sigma_z \right) \begin{pmatrix} \psi_{\uparrow k} \\ \psi_{\downarrow k} \end{pmatrix}, \quad (1.24)$$

where  $\psi_{\sigma k}^\dagger$  creates an electron with momentum  $k$  and spin  $\sigma$ ,  $m^*$  is the effective mass,  $\mu$  is the chemical potential,  $\alpha$  is the Rashba parameter and  $V_Z$  is the applied Zeeman field. The band energies of this Hamiltonian are

$$E_{\pm}(k) = \frac{\hbar^2 k^2}{2m^*} - \mu \pm \sqrt{\alpha^2 k^2 + V_Z^2}, \quad (1.25)$$

and they are shown in Fig. 1.2.

The effective mass approximation leads to a quadratic dispersion with a two-fold degeneracy due to the spin 1/2 of the electrons. The Rashba spin-orbit coupling then splits the two parabolas (red and blue curve in Fig. 1.2), but keeps the degeneracy at the  $\Gamma$  point, because of time-reversal symmetry. The Zeeman field breaks the time reversal symmetry and opens a gap at the  $\Gamma$  point. If the chemical potential is tuned to be inside this gap, the system mimics a spinless system.

Now, we can include the proximity induced superconducting pairing

$$H = H_W + H_{SC} = H_W + \int dk \left( \Delta \psi_{\uparrow k} \psi_{\downarrow -k} + \Delta^* \psi_{\downarrow -k}^\dagger \psi_{\uparrow k}^\dagger \right), \quad (1.26)$$

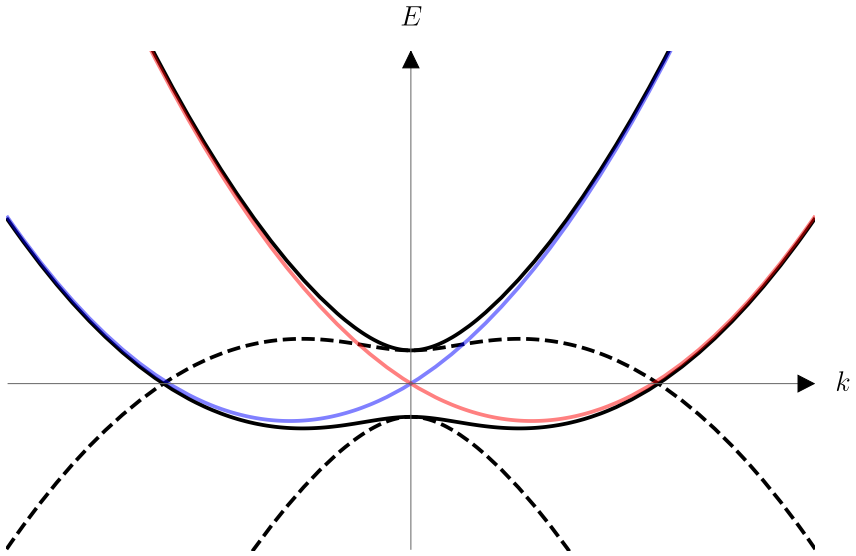


**Figure 1.2.:** Band structure of the nanowire without induced superconductivity for a finite Zeeman field (black curves) and without Zeeman field (blue and red curve). The dashed curves correspond to the hole degrees of freedom that arise in the BdG formalism.

with the superconducting pairing amplitude  $\Delta$ . It is convenient to rewrite the Hamiltonian in terms of eigenstates of the nanowire Hamiltonian  $H_W$

$$\begin{aligned}
 H = \int dk & \left( E_+(k) \psi_+^\dagger(k) \psi_+(k) + E_-(k) \psi_-^\dagger(k) \psi_-(k) \right. \\
 & + \frac{\Delta_p(k)}{2} [\psi_+(-k) \psi_+(k) + \psi_-(-k) \psi_-(k) + h.c.] \\
 & \left. + \Delta_s(k) [\psi_-(-k) \psi_+(k) + h.c.] \right), \tag{1.27}
 \end{aligned}$$

with the pairing potentials

$$\Delta_p = \frac{\alpha k \Delta}{\sqrt{\alpha^2 k^2 + V_Z^2}}, \quad \Delta_s = \frac{V_Z \Delta}{\sqrt{\alpha^2 k^2 + V_Z^2}}. \tag{1.28}$$

The two pairing potentials mix electron and hole degrees of freedom in the BdG fashion. The dashed curve in Fig. 1.2 shows the hole degrees of freedom for the wire without superconductivity. At points in momentum space where the electron and hole energies are the same the pairing potential opens gaps. Here,  $\Delta_p$  is an intraband coupling, because it couples electron and hole degrees of freedom resulting from the same band, while  $\Delta_s$  couples the bands around  $k = 0$ , so it is an interband coupling. In the limit of large Zeeman field  $V_Z \gg \Delta$  assuming that only the lower band  $E_-$  is occupied the Hamiltonian effectively becomes

$$\begin{aligned}
 H_{\text{eff}} = \int dk & \left( \left[ \frac{\hbar^2 k^2}{2m^*} - \mu - |V_Z| \right] \psi_-^\dagger(k) \psi_-(k) \right. \\
 & \left. + \frac{\alpha \Delta k}{2|V_Z|} [\psi_-(-k) \psi_-(k) + h.c.] \right), \tag{1.29}
 \end{aligned}$$

which directly maps to the Kitaev chain under  $k \rightarrow i\partial_x$  and being put on a lattice. The topological criterion in this case is

$$V_Z > \sqrt{\Delta^2 + \mu^2}. \tag{1.30}$$

Because  $V_Z = \sqrt{\Delta^2 + \mu^2}$  describes the point in parameter space in which the gap in the excitation spectrum closes. In the case of a finite nanowire the MBSs are not completely localized at the ends of the wire but de-

## 1. Introduction

---

cay exponentially into the wire with additional oscillations [55]. The hybridization energy of the two MBSs then is given by

$$\varepsilon \approx \hbar^2 k_{F,\text{eff}} \frac{e^{-2L/\xi}}{m^* \xi} \cos(k_{F,\text{eff}} L), \quad (1.31)$$

where  $k_{F,\text{eff}}$  is the effective Fermi wave vector associated with the zero-mode solution and  $\xi$  is the effective coherence length both of which are functions of the microscopic parameters of the model Hamiltonians shown in Eq. (1.26). Related model Hamiltonians can not only be realized with semiconducting nanowires, like for example InAs or InSb nanowires, but also with 2DEG systems [56] or carbon nanotubes [57].

Another system that is predicted to be a one dimensional topological superconductor is magnetic adatoms chains on top of a superconducting surface [58–63]. Here, the needed spin structure comes from the interplay of spin-orbit coupling from the superconductor (for example lead) with the ferromagnetism of the adatoms (for example iron) [59], or in the absence of spin-orbit coupling spatially modulated spin arrangements in the adatoms [60, 63]. Another way to recreate the low-energy physics of the Kitaev chain is to use the emerging edge states of two dimensional topological insulators [52]. Here, again the superconducting proximity effect is used to induce superconductivity in the spin-locked counterpropagating edge states. Other proposals use Josephson junctions induced in 2DEGs [64, 65], Corbino geometry Josephson junction induced in surface states of three dimensional topological insulators [66], proximity induced superconductivity in hinge states of higher order topological insulators [67, 68] and many others [69–72]. To discuss all these proposals in detail would exceed the scope of this thesis and we refer the interested reader to more detailed review articles [23–27].

In addition to proposals how to create MBSs, also signatures of MBSs are needed in order to establish their existence. One of the first proposed signatures of MBSs is the so called fractional Josephson effect [29, 73, 74]. Here, the periodicity of the supercurrent with respect to the superconducting phase difference in a junction of two MBSs is doubled ( $4\pi$  instead of  $2\pi$  periodicity) in contrast to conventional Josephson junctions. This can be explained by the fact that the two MBSs at the junction constitute a fermionic degree of freedom. This way single electrons can be transferred between the two superconductors instead of Cooper pairs. In the frequency domain this leads to the missing of odd Shapiro steps. In order

to observe the fractional Josephson effect straightforwardly, the number parity needs to be conserved to protect the crossing in the energy phase relation that enables the doubled periodicity, so that quasiparticle poisoning destroys this signature [75, 76]. Also, the finite size of the topological superconductor in any experiment leads to a hybridization with the outer MBSs which introduces a gap at the parity crossing [77–81]. Experimentally, the fractional Josephson effect has been reported in the frequency domain with missing Shapiro steps [82–88] and Josephson radiation/emission [89, 90]. On another note, even higher fractions for the fractional Josephson effect can be realized with parafermions [91], a generalization of Majorana fermions [92–94].

Another way to test the existence of MBSs is to couple a normal conducting lead as a local electrical probe. Because the differential conductance probes the density of states, a zero bias peak should arise in the topologically non-trivial regime. To be precise this zero bias peak at zero temperature is predicted to be quantized to  $2e^2/h$ , if the lead couples to a single MBS, independent of coupling strength [95–97], because the MBS couples to the electron and hole states in the lead with same tunnel coupling due to its particle-hole symmetric property. And indeed many experiments show the emergence of a zero bias peak in the predicted regime [56, 98–113]. However, only recently the robust quantization has been reported [114]. If a second lead is coupled to the MBS that emerges on the other side of the one-dimensional TSC with a symmetrically applied bias voltage between lead and superconductor crossed Andreev reflection is predicted to be the dominant transport process in the low bias regime [115, 116]. Here, low bias regime means a bias voltage energy  $eV$  lower than the Majorana hybridization energy  $\varepsilon$ . Also, because MBSs always come in pairs the differential conductances in the two leads should be correlated under changes of the microscopic parameters [117, 118]. If the nanowire is floating that means that charging on the nanowire becomes important, “electron teleportation” is predicted to occur [119]. These floating devices are called Majorana islands. Electron teleportation means that the Coulomb blockade goes from  $2e$ -periodic oscillations (transportation of Cooper pairs) in the topologically trivial regime to  $1e$ -periodic oscillations (coherent single-electron transport) in the topologically non-trivial regime. This effect has been reported in Majorana nanowires where the applied magnetic field changes the periodicity from  $2e$  to  $1e$  [120].

## 1. Introduction

---

However, the unique signature of MBSs is their non-Abelian anyonic exchange statistics [24, 121, 122]. Under exchange of two MBSs one of them picks up a minus sign

$$\gamma_1 \rightarrow -\gamma_2, \quad \gamma_2 \rightarrow \gamma_1. \quad (1.32)$$

A second exchange results in a minus sign for both of them with respect to the start of the exchange. Because of this we can associate the MBSs with an exchange phase of  $\pi/2$ , in contrast to regular fermions (exchange phase of  $\pi$ ) or bosons (exchange phase of  $2\pi$ ). Because their exchange phase is neither bosonic nor fermionic they are called anyons. Mathematically, the reason for this is that the parity  $\mathcal{P} = i\gamma_1\gamma_2$  should not change under exchange of the two MBSs. Because the Majorana operators also need to be hermitian, the only possible exchange phase (except which MBS gets the minus sign under exchange is arbitrary) is the one discussed before. The exchange of the two MBSs is then generated by the unitary operator  $B_{12} = \exp[(\pi/4)\gamma_1\gamma_2] = [1 + \gamma_1\gamma_2]/\sqrt{2}$ . Now, let us consider four MBSs. The unitary braid operators that exchange two neighboring MBSs that involve a common MBS do not commute

$$[B_{i-1,i}, B_{i,i+1}] = \gamma_{i-1}\gamma_{i+1}, \quad (1.33)$$

because of this they are called non-Abelian. In order to braid MBSs in real space a two dimensional system is needed. Suggestions to realize this are for example T-junctions using Majorana nanowires [123, 124] or Corbino geometry Josephson junctions [66, 125]. Experiments to report signatures of braiding of MBSs are however still missing. In addition to braiding in real space (e.g. exchanging MBS in real space), the non-Abelian property of MBSs can also be utilized through a sequence of measurements [126, 127] or switching on and off couplings between different MBSs [128, 129].

The non-Abelian exchange statistics is also what makes MBSs a candidate for building blocks for qubits. To understand this in more detail we need to consider not two but four MBSs, because two MBSs are not enough to constitute a physical qubit because of parity conservation. These four MBS build up two non-local fermions that both can be empty or occupied and that are described with the operators

$$f_1^\dagger = \frac{1}{2}(\gamma_1 + i\gamma_2), \quad f_2^\dagger = \frac{1}{2}(\gamma_3 + i\gamma_4). \quad (1.34)$$

One possible basis for this low-energy space is

$$|n\rangle_1 |m\rangle_2 = \left(f_1^\dagger\right)^n \left(f_2^\dagger\right)^m |0\rangle, \quad (1.35)$$

where  $|0\rangle$  is the ground state with  $f_j |0\rangle = 0$  for  $j = 1, 2$  and  $n, m = 0, 1$ . Because of the parity conservation in superconducting systems the four dimensional low-energy space decouples into two  $2 \times 2$ -blocks. One of these  $2 \times 2$ -blocks then constitutes a qubit. For our discussion we focus now on the odd parity sector that is spanned by the two states  $|0\rangle = |1\rangle_1 |0\rangle_2$  and  $|1\rangle = |0\rangle_1 |1\rangle_2$ . As seen before the exchange of two MBSs is generated by  $B_{i,j}$ . If we now consider not an exchange but a round trip of  $\gamma_1$  and  $\gamma_2$  we find

$$B_{1,2}^2 = \sigma_z. \quad (1.36)$$

Additionally, all other Pauli matrices can be generated by

$$B_{2,3}^2 = \sigma_x \quad B_{1,3}^2 = \sigma_y. \quad (1.37)$$

The square roots of the Pauli matrices can be realized just by exchange of two MBS accordingly. Also, more elaborate exchange schemes lead to the so called Hadamard gate

$$B_{1,2} B_{2,3} B_{1,2} = \sqrt{\frac{i}{2}} (\sigma_x + \sigma_z) = e^{\frac{i\pi}{4}} H, \quad (1.38)$$

with

$$H = \frac{1}{2} \begin{pmatrix} 1 & 1 \\ 1 & -1 \end{pmatrix}. \quad (1.39)$$

The gates that contain Pauli matrices and their square roots are called single qubit Clifford gates [28] and they all can be generated through braiding. However, the Clifford gates do not constitute a universal set of single qubit gates. The missing magic or T-gate can, however, be realized by introducing topologically non-protected protocols [20, 22, 130–132]. To build a universal quantum computer in addition to the single qubit gates it is sufficient to implement the controlled not gate (CNOT) which acts on two qubits. All other unitary gate operations can be constructed as a combination from the CNOT gates and single qubit rotations. The CNOT gate can also be realized by braiding MBSs, but additionally one needs to be able to measure the fermion parity of four MBSs without gaining information about the fermion parity of pairs within these four [133–136].

## 1. Introduction

---

A computation based on unitary operations built from braiding is called topological quantum computation [18, 22]. The Clifford gate operations are topologically protected by the excitation gap  $\Delta_p$  in the topological superconductor, because it needs to be closed in order to change the topology of the physical system [137]. This protection offers a way for fault tolerant quantum computation [18]. Also,  $\hbar/\Delta_p$  constitutes the timescale on which the quantum operations should be performed. If the exchange of two MBSs is performed too fast, i.e., non-adiabatically the quantum computation scheme becomes faulty.

## 1.2. About this thesis

The aim of this thesis is to contribute to the efforts in characterization of MBSs formed as topologically protected boundary modes in one dimensional TSCs. The main focus lies on the effect that the finite size of the TSC has. In particular, we consider what happens in terms of electronic transport if the wave functions of the MBSs reach across the whole TSC so that both MBSs can be electrically addressed at the same spatial point. These non-local couplings (i.e. couplings to the MBSs emerging at both ends of the wire) are the red threat running through the following chapters.

Chap. 2 mostly follows Ref. [138]. We consider a Kitaev chain which is tunnel contacted by a quantum dot on one side and a spinless lead on the other side. In the topologically non-trivial regime the low-energy sector of the Kitaev chain is spanned by the two emerging MBSs which obtain a finite splitting energy due to their possible wave function overlap. First, we focus on an analytical model that replaces the Kitaev chain with its low-energy sector spanned by the two MBSs. To calculate the transport in this setup we resort to the full counting statistics. In the case of no non-local couplings we show that in specific parameter regimes resonances arise as a function of dot level energy in the differential conductance that can be described with the Fano-Beutler formula. These so called Fano resonances come in pairs and are invariant under a sign change of the dot level energy, a signature that we can attribute to the particle-hole symmetry of a single MBS. By the introduction of the non-local couplings in the effective low-energy model we show that the symmetry of the two Fano resonances with respect to each other is broken. A numerical analysis using the full Kitaev



chain verifies our effective model calculation. By introducing long range hopping between the Kitaev chain and the lead and dot respectively, we can show that the Fano resonance symmetry is broken as both MBS wave functions become accessible for tunneling events.

In Chap. 3 which is based on our publication [139], we extend our analysis by replacing the Kitaev chain with an experimentally relevant Majorana nanowire. While the Kitaev chain is based on spinless fermions the Majorana nanowire takes the electron spin into account. Therefore, we also introduce the spin degree of freedom in the metallic lead and the quantum dot. We first consider the system without the dot. We show that non-local couplings lead to deviations from the predicted quantized differential conductance for coupling to a single MBS. For zero energy MBSs the height of the resonance in the differential conductance is dictated by the difference in spin canting angles of the two MBS wave functions at the junction. Also, the temperature dependence of the differential conductance shows that in an intermediate to high temperature regime the difference between coupling to a single or both MBS becomes blurred. When including the dot in the calculations we treat the resulting Coulomb interaction within a mean field approximation. In our analytical model we find the emergence of two pairs of Fano resonances, one for every spin on the dot. These pairs again show an inherent symmetry as long as only local couplings persist. Finally, in a numerical treatment of the setup in which the mean field approximation is applied selfconsistently, we show that the asymmetry in these Fano resonances is largest for smallest Majorana splitting energies.

Chap. 4 is based on Ref. [140]. We investigate a Josephson junction comprised of an  $s$ -wave superconducting lead and a finite sized Majorana nanowire. In a low-energy effective model we show that the equilibrium Josephson current is only non-vanishing if both MBSs are tunnel coupled to the  $s$ -wave lead. The wave function of the two MBSs enter the supercurrent in the form of a singlet projection due the singlet Cooper pairs in the superconducting lead. As a function of Zeeman energy the critical current is oscillating. This oscillations can be attributed to the rotation of the spin canting angle of the more distant MBS to the junction. The amplitude of these oscillations is rising with increased applied Zeeman field, because the localization length of the MBS is increased. Furthermore, we see discontinuities in the critical current. These discontinuities occur at points in parameter space at which the parity of the

## 1. Introduction

---

ground state changes (parity crossing) and at them the sign of the critical current changes. A numerical analysis shows a qualitative agreement for the Josephson current mediated by the low-energy states. However, higher energy contribution which come from a residual  $s$ -wave pairing in the Majorana nanowire conceal the Majorana contributions. But, by using quasiparticle poisoning and the inherent particle-hole symmetry of the superconductors the Josephson current coming from the MBSs can be unveiled. Lastly, we summarize the findings of this thesis in Chap. 5.

## 2. Fano resonances in spinless Majorana bound states-quantum dot system

In order to use Majorana bound states (MBSs) as building blocks for topological quantum computing their existence needs to be established without a doubt. The key signature of MBS, the quantized differential conductance at zero bias voltage, was reported recently [114], however there is still a debate if the reported quantization can come from trivial Andreev bound states [141–147]. So in order to decide in this matter additional signatures of MBSs are needed.

A helpful tool to analyze MBSs are quantum dots. These quantum dots are small structures that confine a precise and tunable number of charge carriers. In general, the electrons or holes are trapped in the dot with the help of repelling electric fields, effectively putting the charge carriers in a box. This leads to eigenstates with discrete energy levels [148]. These energy levels can be tuned by using electrical gating. Tunnel barriers can be used to couple the quantum dot to a reservoir and in this case to MBSs. The advantage of using quantum dots in combination with MBSs lies in the additional degrees of freedom and their high precision tunability [149–156].

Additionally, the inclusion of a quantum dot can lead to Fano resonances. These resonances arise as the interference pattern between a discrete and a continuous path [157]. The line shape of these Fano resonances is universal and can be described with just three parameters using the Fano-Beutler formula [158]. These Fano resonances have been seen in the transmission through a quantum dot [159] as the function of dot level energy. The emergence of Fano resonances in MBS-quantum dot hybrid systems has already been discussed in the literature, however the proposed setups analyze Fano resonances as function of bias voltage [160–163]

and/or flux through a loop built from MBSs [164–166].

Here, we consider a Kitaev chain coupled to a metallic lead on one end and a quantum dot on the other end. We use full counting statistics (FCS) to calculate the cumulant generating function (CGF). In a low-energy effective approach the CGF predicts that the only process that contributes to the transport from lead to Kitaev chain is Andreev reflection. We show that this setup exhibits Fano resonances as a function of dot level energy and analytically relate the parameters describing the Fano-Beutler formula to the microscopic parameters of the considered setup. The two paths needed for Fano resonances to occur are firstly direct Andreev reflections and secondly processes in which the charge carriers virtually occupy the quantum dot before entering the Cooper pair condensate by Andreev reflection. While the first path is independent of dot level energy, the second path is resonant with it. We show that the Fano resonances come in pairs and are invariant under a sign change in the dot level energy. The asymmetry parameter of an individual Fano resonance can be used to measure the energy splitting of the two MBS in the finite size Kitaev chain, because the asymmetry parameter changes its sign as the bias voltage between lead and grounded superconductor is tuned across the splitting energy.

In addition, to the analytical low-energy model we also consider a full finite size Kitaev chain and find good agreement between the two in the low-energy regime. We show that the inclusion of finite temperature can destroy the quantization of the differential conductance. However, the symmetry of the Fano resonances is not affected by the inclusion of temperature.

Finally, we take a look at extended couplings that not only connect lead and dot to the closer but also to the more distant MBS, respectively. In an analytical low-energy model we parametrize the couplings in a way that allows us to smoothly tune between “pure” Majorana-like couplings, i.e. coupling to a single MBS, and “pure” Dirac-like couplings, i.e. coupling to both MBSs with the same tunneling amplitude.

This Chapter is based on Ref. [138]. In Chap. 2.1 we introduce the model Hamiltonians. We also calculate the CGF and discuss the properties of the probability for Andreev reflections. The relationship between the probability for Andreev reflections and the Fano-Beutler formula is discussed in great detail in Chap. 2.2. In Chap. 2.3 we underline our analytical findings by numerically analyzing a full Kitaev chain model. The

non-local couplings are introduced in Chap. 2.4 in which we focus on an analytical low-energy model in Chap. 2.4.1 and extended tunnel couplings to the Kitaev chain in Chap. 2.4.2. Finally, we conclude this project in Chap. 2.5.

## 2.1. Setup and Andreev Reflection Probability

The setup under consideration consists of a Kitaev chain in the topologically non-trivial phase which is tunnel coupled to a metallic lead on one side and a quantum dot on the other side. A sketch of this setup can be seen in Fig. 2.1. Because the Kitaev chain only consists of spinless fermions we also approximate the lead with spinless fermions and describe the quantum dot with a single spinless level  $\varepsilon_D$ , thus the spinless quantum dot can only be empty or singly occupied. The low-energy sector of the Kitaev chain consists of two MBSs, described with the self-hermitian operators  $\gamma_i = \gamma_i^\dagger$ , which can have a splitting energy  $\varepsilon \propto e^{-L/\xi_M}$  where  $L$  is the length of the Kitaev chain and  $\xi_M$  is the Majorana localization length [29]. This splitting is generated by the spatial overlap of the two MBSs due to the finite size of the Kitaev chain. The full Hamiltonian for this setup is given by

$$H = H_L + H_T + H_M + H_{Dot} + H_{TDot}, \quad (2.1)$$

$$H_M = i\varepsilon\gamma_1\gamma_2, \quad (2.2)$$

$$H_{Dot} = \varepsilon_D d^\dagger d, \quad (2.3)$$

$$H_T = i\gamma_1 [t_1\psi^\dagger(0) + t_1^*\psi(0)], \quad (2.4)$$

$$H_L = -i\hbar v_F \int dx \psi^\dagger(x) \partial_x \psi(x), \quad (2.5)$$

$$H_{TDot} = i\gamma_2 [t_2 d^\dagger + t_2^* d], \quad (2.6)$$

where  $v_F$  is the Fermi velocity in the normal conducting lead,  $t_1$  is the tunneling amplitude between the MBS system and the lead,  $t_2$  is the tunneling amplitude between the quantum dot and the MBS system. The creation operator  $d^\dagger$  creates an electron on the quantum dot and  $\psi^\dagger(x)$  creates an electron in the lead at position  $x$ .

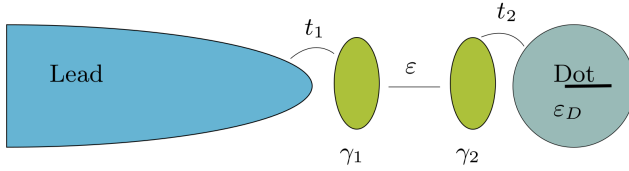


**Figure 2.1.:** Schematic sketch of the considered setup, in which two Majorana bound states  $\gamma_1$  and  $\gamma_2$  arise in a Kitaev chain. One of them is contacted by a normal conducting lead and the other one with a quantum dot with level energy  $\varepsilon_D$ . The two MBS experience a splitting  $\varepsilon$  due to a wave function overlap of the two MBS. Figure and caption taken from Ref. [138]. ©[2017] American Physical Society.

In order to calculate the electron transport between lead and superconductor we resort to the FCS. The FCS is a formalism based on the calculation of Keldysh Green's functions [167]. The main entity of the FCS is the CGF. For its derivation we closely follow [116] and the details of the derivation can be found in Ref. [168]. The CGF is calculated to be

$$\ln \chi(\lambda) = \frac{\mathcal{T}}{2\hbar} \int dE \ln [1 + p(E)(e^{-2ei\lambda} - 1)n(E)n(-E) + p(E)(e^{2ei\lambda} - 1)(n(E) - 1)(n(-E) - 1)], \quad (2.7)$$

where  $n(E) = 1/(1 + e^{\beta(E - eV)})$  is the Fermi function in the lead with  $\beta = 1/k_B T$  the inverse temperature and  $\mathcal{T}$  is a long measurement time. This CGF describes a binomial process in which Andreev reflections, the transfer of two electrons by reflection of an incoming electron as an outgoing hole, occur with the energy dependent probability  $p(E)$ . It also shows that these Andreev reflections are the only processes which can contribute to the electronic transport. The transport characteristics like the current and symmetrized zero frequency noise can be calculated by taking the first and second derivative of the CGF with respect to the counting field  $\lambda$ , respectively. At zero temperature the differential conductance and dif-

## 2.1. Setup and Andreev Reflection Probability

ferential noise are calculated to be

$$\frac{dI}{dV} = \frac{d}{dV} \frac{i}{\mathcal{T}} \frac{\partial}{\partial \lambda} \ln \chi \Big|_{\lambda=0} = \frac{2e^2}{h} p, \quad (2.8)$$

$$\frac{dP}{dV} = \frac{d}{dV} \frac{-1}{\mathcal{T}} \frac{\partial^2}{\partial \lambda^2} \ln \chi \Big|_{\lambda=0} = \frac{4e^3}{h} p(1-p), \quad (2.9)$$

with

$$p = \frac{4\Gamma^2(eV)^2}{\left( \frac{4\varepsilon^2(\varepsilon_D^2 - (eV)^2)}{4|t_2|^2 + \varepsilon_D^2 - (eV)^2} - (eV)^2 \right)^2 + 4\Gamma^2(eV)^2}. \quad (2.10)$$

Here,  $\Gamma = 2\pi\rho_0|t_1|^2$  where  $\Gamma/\hbar$  is the tunneling rate between the lead and the nearest MBS ( $\gamma_1$ ) with the constant density of states per length  $\rho_0 = (2\pi\hbar v_F)^{-1}$  and  $eV$  is the bias voltage between the lead and the grounded topological superconductor hosting the two MBSs. Because the Andreev reflection is the only relevant transport process the measurement of the differential conductance and therefore measurement of the Andreev reflection probability is enough to fully characterize the full transport. For the dot level energy

$$\varepsilon_{D,\max}^2 = (eV)^2 + \frac{4|t_2|^2(eV)^2}{(2\varepsilon)^2 - (eV)^2}, \quad (2.11)$$

the differential conductance becomes quantized with  $2e^2/h$ , because of perfect Andreev reflection ( $p = 1$ ). In addition, the Andreev reflection can also be blocked ( $p = 0$ ) which leads to antiresonances in the differential conductance and occurs when the dot level energy satisfies

$$\varepsilon_{D,0}^2 = (eV)^2 - 4|t_2|^2. \quad (2.12)$$

It is convenient to rewrite the Andreev reflection probability to

$$p(\varepsilon_D) = \frac{1}{1 + \frac{q^2(\varepsilon_D^2 - \varepsilon_{D,\max}^2)^2}{(\varepsilon_D^2 - \varepsilon_{D,0}^2)^2}}, \quad (2.13)$$

with  $q^2 = (\varepsilon^2 - (eV/2)^2)/(\Gamma^2(eV/2)^2)$ , because we are interested in the influence of the quantum dot on the transport properties.

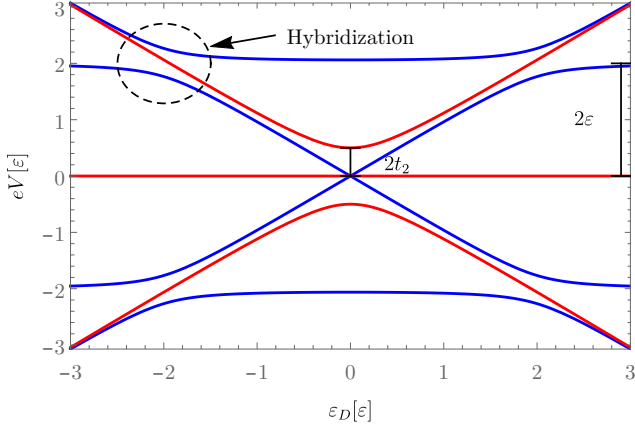


**Figure 2.2.:** Resonances ( $p = 1$ , blue) and antiresonances ( $p = 0$ , red) of the differential conductance in dependence of the bias voltage  $eV$  between lead and the Kitaev chain (grounded), and the quantum dot level energy for  $t_2 = 0.25\varepsilon$ . The resonances correspond to the spectrum of the system without the lead. The levels show an avoided crossing if  $\varepsilon_D \approx \pm 2\varepsilon$ . Figure and caption adapted from Ref. [138].



The resonances and antiresonances as a function of applied bias voltage and dot level energy are summarized in Fig. 2.2. The resonances correspond to the spectrum of the considered setup without the metallic lead and we see a hybridization of the MBSs with the quantum dot state when they are in resonance with respect to each other. This hybridization manifests itself in form of an avoided crossing. At dot level energies away from this hybridization we can attribute the resonances to the MBSs (nondispersive with  $\varepsilon_D$ ) and quantum dot states (linear dispersion with  $\varepsilon_D$ ).

The point  $eV = \varepsilon_D = 0$  is also of special interest. For a finite overlap energy  $\varepsilon \neq 0$ , the Andreev reflection probability vanishes at zero bias voltage and zero temperature for all finite quantum dot energies  $\varepsilon_D \neq 0$  [75]. If we however set the dot level energy in Eq. (2.10) to zero first and then look at the zero-bias Andreev reflection probability, we find it to be one. However, this problem is resolved as soon as we take finite temperature into account, because of its broadening effect on the resonances.

## 2.2. Fano Resonances

In this section, we want to show that Fano resonances (FRs) arise in differential conductance as a function of dot energy level. These resonances are the result of an interference between a continuous and a resonant path [169] and their line shape can be described with the normalized Fano-Beutler formula [158]

$$p_{\text{FB}}(\varepsilon_D) = \frac{1}{1 + q^2} \frac{((\varepsilon_D - E_R)/(2\Gamma_F) + q)^2}{1 + ((\varepsilon_D - E_R)/(2\Gamma_F))^2}, \quad (2.14)$$

where  $\Gamma_F$  is the width of the FR and  $E_R$  is the resonance energy. The parameter  $q$  describes the asymmetry of the resonance and its sign determines whether the destructive or constructive interference can be found at smaller energies.

In this setup the continuous path for an electron is direct Andreev reflection without including the quantum dot. As this path does not include the quantum dot it is independent of its level energy. In the second path the electron first traverses the wire and occupies the dot before returning to the wire and forming a Cooper pair by emission of a hole into the lead as shown in Fig. 2.3. This second part is dependent on

## 2. Fano resonances in spinless Majorana bound states...

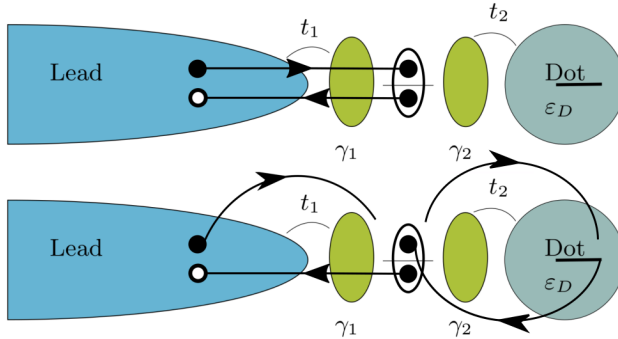


**Figure 2.3.:** Two possible paths for Andreev reflection (lines with arrows). In the upper panel the incoming electron (full circle) directly enters the Cooper pair condensate (denoted by an oval with two electrons) by simultaneous back reflecting of a hole (empty circle). This process is independent of the dot. The second panel shows a transport path where the incoming electron virtually occupies the quantum dot before entering the condensate. This process is resonant with respect to the dot level position. The interference of these two paths leads to the Fano resonance (further processes where the reflected hole visits the dot are possible, too). Figure and caption taken from Ref. [138]. ©[2017] American Physical Society.

the dot level energy and the interference of both leads to the emergence of Fano resonances as function of the dot level energy.

In order to show that the Andreev reflection probability and therefore the differential conductance really exhibits Fano resonances, we relate  $p(\epsilon_D)$  with the Fano-Beutler formula. In order to do this we compare special points of Eq. (2.14) with those of Eq (2.10), the resonance ( $p_{\text{FB}}(\epsilon_D) = 1$ ) and the antiresonance ( $p_{\text{FB}}(\epsilon_D) = 0$ ) of a FR as a function of  $\epsilon_D$  appear at

$$\epsilon_D = \epsilon_{D,\text{max}} \equiv 2\Gamma_F/q + E_R, \quad (2.15)$$

and at

$$\epsilon_D = \epsilon_{D,0} \equiv -2q\Gamma_F + E_R, \quad (2.16)$$

respectively. We can now enter these in Eq. (2.13) for the calculated An-

Andreev reflection probability. In the limit of small FR width i.e.  $|\Gamma_F/E_R| \ll 1$  the Andreev reflection probability can be simplified to

$$p(\varepsilon_D) \approx \left( \frac{1}{1+q^2} \right) \left( \frac{(\frac{\varepsilon_D - E_R}{2\Gamma_F} + q)^2}{1 + (\frac{\varepsilon_D - E_R}{2\Gamma_F})^2} \right) \left( \frac{(\frac{\varepsilon_D + E_R}{2\Gamma_F} - q)^2}{1 + (\frac{\varepsilon_D + E_R}{2\Gamma_F})^2} \right). \quad (2.17)$$

This describes the product of two Fano-Beutler formula. The resonance energies  $E_R$  as well as the asymmetry parameters  $q$  for the two Fano resonances have opposite sign and both have the same width  $\Gamma_F$ . We can further simplify the Andreev reflection probability in the limit of  $E_R^2/\Gamma_F^2 \gg q^2$  to find

$$p(\varepsilon_D) \approx \frac{1}{1+q^2} \frac{(\frac{|\varepsilon_D| - E_R}{2\Gamma_F} + q)^2}{1 + (\frac{|\varepsilon_D| - E_R}{2\Gamma_F})^2}, \quad (2.18)$$

which also describes two FRs which are mirrored at  $\varepsilon_D = 0$ . To relate the parameters of the Fano-Beutler formula to the microscopic parameters of the setup we enter  $\varepsilon_{D,\max}$  and  $\varepsilon_{D,0}$  from Eq. (2.15) and Eq. (2.16) into Eq. (2.11) and Eq. (2.12), respectively and focus on the FR at positive dot level energy

$$E_R = 2 \frac{(\frac{eV}{2})^2 \Gamma^2 \sqrt{(\frac{eV}{2})^2 - t_2^2} + ((\frac{eV}{2})^2 - \varepsilon^2)^{3/2} \sqrt{(\frac{eV}{2})^2 ((\frac{eV}{2})^2 - \varepsilon^2 - |t_2|^2)}}{(\frac{eV}{2})^2 \Gamma^2 + (\varepsilon^2 - (\frac{eV}{2})^2)^2}, \quad (2.19)$$

$$\Gamma_F = \frac{((\frac{eV}{2})^2 - \varepsilon^2) \sqrt{(\frac{eV}{2})^2 - t_2^2} - \sqrt{(\frac{eV}{2})^2 - \varepsilon^2} \sqrt{(\frac{eV}{2})^2 ((\frac{eV}{2})^2 - \varepsilon^2 - t_2^2)}}{(\frac{eV}{2}) \Gamma + (\varepsilon^2 - (\frac{eV}{2})^2)^2 / ((\frac{eV}{2}) \Gamma)}, \quad (2.20)$$

$$q = \frac{(\frac{eV}{2})^2 - \varepsilon^2}{\Gamma \frac{eV}{2}}. \quad (2.21)$$

The assumptions of a large resonance energy  $E_R$  and small width  $\Gamma_F$  can now be represented with the model parameters and it can be seen that the description with the Fano formula holds for  $|t_2| \ll |eV|$ . This corresponds to a weakly coupled QD. We note that the sign of the asymmetry changes as the applied bias voltage energy is tuned through  $2\varepsilon$ . This means that the asymmetry can be used to measure the overlap energy. For a large bias voltage the position of the resonance is in leading order given by the bias voltage energy. But we also find a regime in which the description

## 2. Fano resonances in spinless Majorana bound states-...

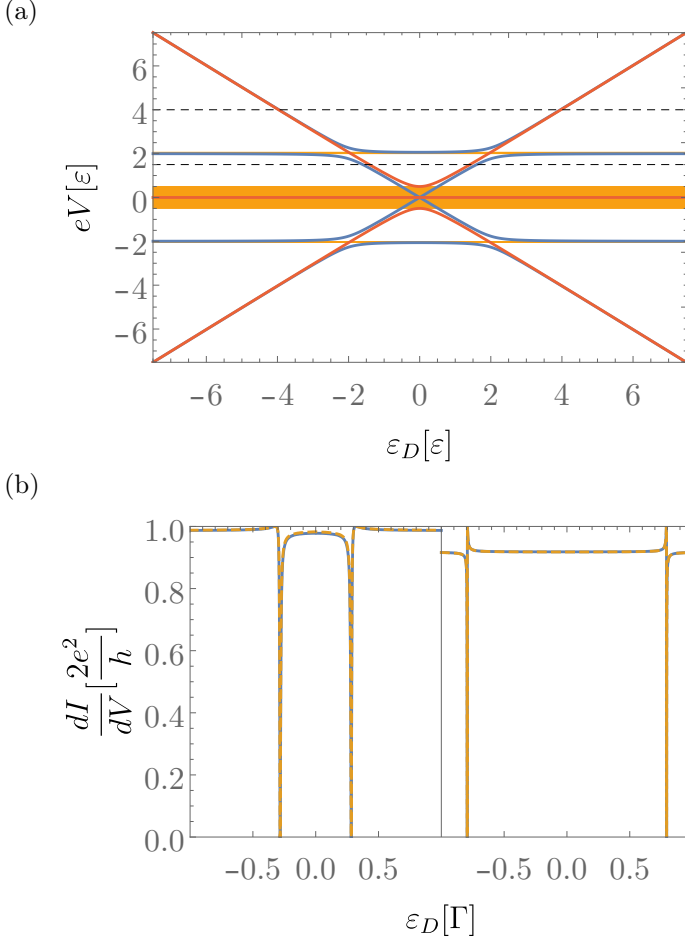


**Figure 2.4.:** Resonances and antiresonances in the setup with  $t_2 = 0.25\varepsilon$ . The dashed lines correspond to the bias voltages chosen for the plots in (b) ( $eV = 0.095\Gamma$  for the left plots,  $eV = 0.2\Gamma$  for the right plots). Orange background color marks the parameter space in which no Fano resonances arise. (b) Differential conductance vs. quantum dot level energy for different bias voltages between lead and topological superconductor. The blue line is the exact calculated differential conductance, whereas the yellow dashed line is the approximation using Eq.(2.18), where  $E_R$ ,  $\Gamma_F$  and  $q$  are given by Eqs. (2.19-2.21), respectively. Figure and caption adapted from Ref. [138].

using the Fano-Beutler formula fails. First of all, it fails in the regime  $(eV/2)^2 < |t_2|^2$ , because the resonance energy and the width of the FR would both become imaginary. This can be explained by the fact that the Fano-Beutler formula only describes a single Fano resonance. In this regime however, the two resonances overlap so that the description using the Fano-Beutler formula fails. Second, for  $\varepsilon < |eV|/2 < \sqrt{|t_2|^2 + \varepsilon^2}$  the Fano-Beutler formula is also not applicable. This is the regime in which the MBSs hybridize strongly with the quantum dot states. Because of this hybridization the distinction of the two different paths becomes blurry. These two regimes are highlighted in Fig.2.4 (a) with orange boxes and the dashed lines correspond to the line cuts for which we show the differential conductance in Fig.2.4 (b). The full lines display the exactly calculated differential conductance and they are in very good agreement with the deduced Fano form (dashed lines). The dashed lines result from the Fano-Beutler formula Eq. (2.18) with the parameters  $E_R$  and  $\Gamma_F$  expressed with the microscopic parameters of our model via Eq. (2.19) and Eq. (2.20).

The clear signature of coupling to a single MBS in this setup is that the differential conductance peaks are quantized with  $2e^2/h$  and that the differential conductance is invariant under the transformation  $\varepsilon_D \rightarrow -\varepsilon_D$ . Both are a direct consequence of the particle-hole symmetric nature of a Majorana excitation. The invariance under a sign change of the applied bias voltage, however, comes from the particle-hole symmetry inherent to all superconductors described within the Bogoliubov-de Gennes formalism.

## 2.3. Kitaev Chain Calculations

Now, we want to extend the previous calculations by including the full Kitaev chain instead of only the low-energy MBSs. Here our starting point is a continuum Hamiltonian for a  $p$ -wave superconductor within the Bogoliubov-de Gennes formalism which we discretize on a one dimensional

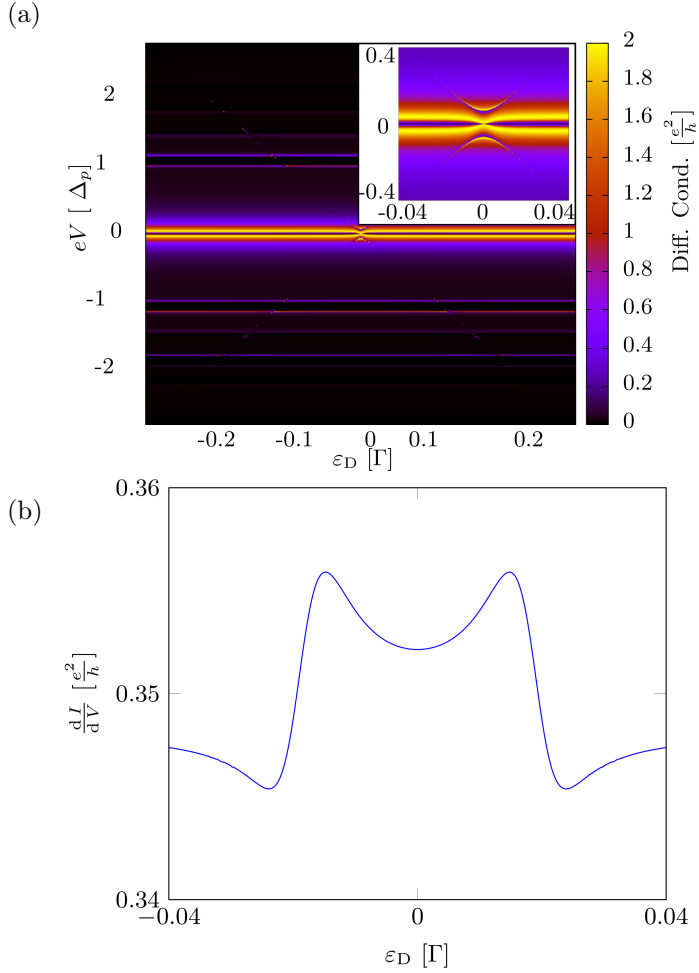


**Figure 2.5.:** (a) Differential conductance as function of the dot level energy and the bias voltage between lead and the Kitaev chain with  $N = 100$  sites. The parameters are  $a = 6 \cdot 10^{-3}$ ,  $\tilde{t} = 1/4500$ ,  $|\tilde{\Delta}| = 1/700$ ,  $\Gamma = 1$ ,  $U = 0.2$  and  $t_2 = 0.09$ , which corresponds to the topologically non-trivial phase. The  $p$ -wave gap is around  $\Delta_p = 0.1\Gamma$  and above this gap the differential conductance is on the order of  $10^{-3} \frac{e^2}{h}$ . At lower energies resonances can be seen which correspond to in gap states. The strongest resonance is the Majorana induced resonance with a quantized differential conductance of  $\frac{2e^2}{h}$ . The influence of the dot can be seen best at the Majorana resonance and results in destructive interference. The inset shows the low-energy section. The quantized resonances corresponding to the dot level cannot be clearly seen because of resolution problems. (b) Fano resonance at finite temperature  $k_B T = 0.02\Delta_p$ . This temperature is in agreement with comparable experiments [106]. The symmetry with respect to the dot level energy is conserved also at finite temperatures. Caption and Figure adapted from Ref. [138].

chain with  $N$  sites and site spacing  $a = L/N$

$$\begin{aligned}
 H_{p\text{-wave}} &= \frac{1}{2} \int_0^L dx \begin{pmatrix} \Psi^\dagger(x) & \Psi(x) \end{pmatrix} \begin{pmatrix} -\tilde{t}\partial_x^2 + U & -i2\tilde{\Delta}\partial_x \\ -i2\tilde{\Delta}^*\partial_x & \tilde{t}\partial_x^2 - U \end{pmatrix} \begin{pmatrix} \Psi(x) \\ \Psi^\dagger(x) \end{pmatrix} \\
 &= \sum_{j=1}^N \left( U - \frac{2\tilde{t}}{a^2} \right) \left( c_j^\dagger c_j - \frac{1}{2} \right) \\
 &\quad - \sum_{j=1}^{N-1} \left( \frac{\tilde{t}}{a^2} (c_j^\dagger c_{j+1} + c_{j+1}^\dagger c_j) + \frac{i\tilde{\Delta}}{a} c_j^\dagger c_{j+1}^\dagger + \frac{i\tilde{\Delta}^*}{a} c_j c_{j+1} \right) \\
 &= \frac{i}{2} \sum_{j=1}^N \left( U - \frac{2\tilde{t}}{a^2} \right) \gamma_{2j-1} \gamma_{2j} \\
 &\quad + \frac{i}{2} \sum_{j=1}^{N-1} \left[ \left( \frac{\tilde{t}}{a^2} + \frac{|\tilde{\Delta}|}{a} \right) \gamma_{2j} \gamma_{2j+1} + \left( -\frac{\tilde{t}}{a^2} + \frac{|\tilde{\Delta}|}{a} \right) \gamma_{2j-1} \gamma_{2j+2} \right],
 \end{aligned} \tag{2.22}$$

where  $\tilde{t} = \hbar^2/(2m^*)$  and in last step we followed a transformation to Majorana fermions similar to the one described in Ref. [29]. The operator

## 2. Fano resonances in spinless Majorana bound states...

---

$\Psi^\dagger(x)$  creates a Dirac fermion at position  $x$  while  $c_j^\dagger$  is its discretize version and creates an electron on site  $j$ . For  $|U - 2\tilde{t}/a^2| < |2\tilde{t}/a^2|$  the chain is in the topologically non-trivial regime and the MBSs emerge at the ends of the wire [29].

To couple the  $p$ -wave superconductor to a lead, we modify the tunneling Hamiltonian to couple the first Dirac-fermionic site of the chain to the lead with a tunneling amplitude  $t_L$  and the last Dirac-fermionic site of the chain to the quantum dot with a tunneling amplitude  $t_D$ . The full Hamiltonian in terms of Majorana operators then reads

$$H = H_{p\text{-wave}} + H_L + H_D + \frac{i}{2} [-t_D \gamma_{2N} \gamma_{2N+1} + t_D \gamma_{2N-1} \gamma_{2N+2}] \\ + \frac{i}{2} \gamma_1 [(it_L)^* \psi(0) + (it_L) \psi^\dagger(0)] - \frac{i}{2} \gamma_2 [t_L \psi^\dagger(0) + t_L^* \psi(0)]. \quad (2.23)$$

Without loss of generality, we choose  $t_L$  and  $t_D$  to be real valued. To calculate the transport properties we again resort to FCS and use the Levitov-Lesovik formula derived in Ref. [168] and evaluate it numerically. The resulting differential conductance at zero temperature is shown in Fig. 2.5 (a). As seen in the inset the low-energy behavior recovers our analytical findings. Both symmetries ( $eV \rightarrow -eV$  as well as  $\varepsilon_D \rightarrow -\varepsilon_D$ ) and the quantization of the differential conductance can be seen. We attribute this, following our interpretation of the analytical model, to the coupling to a single MBS. Following the original work of Kitaev [29] the localization length of the MBSs in the isolated wire for the chosen parameters is  $\xi_M = 0.244L$ . This localization length leads to an energy splitting due to the spatial overlap of the MBS wave functions, but suppresses the coupling to the dot and/or lead strongly enough that we address the MBSs individually.

The coupling between the dot and the higher energy states is much smaller than the coupling to the MBS which is due to the fact that the higher energy states are delocalized over the whole wire and are not concentrated at its end. Moreover, the differential conductance is not quantized for those resonances corresponding to the high energy states.

At finite temperatures the resulting Fano resonances can still be resolved as shown in Fig. 2.5 (b). Furthermore, the finite temperature has no influence on the symmetry of the two emerging Fano resonances with respect to each other.



## 2.4. Nonlocal Couplings

In the following section, we consider more elaborate couplings between the MBSs and the quantum dot and lead. Again we start using an analytical low-energy model and focus on the differential conductance. After that analysis we consider a numerical model with a full Kitaev chain and long range couplings.

### 2.4.1. Analytical Calculations

In general, all fermions can be decomposed in two Majorana fermions. However, for most fermions these Majorana components are not spatially separated, so that a tunnel contact couples to both of them. We want to emulate the cross-over from a Majorana-like coupling to a regular Dirac-fermion-like coupling. A sketch of the considered setup can be seen in Fig. 2.6 (a).

To realize these couplings physically one can consider a short chain, so that the exponentially localized MBS wave functions can reach the other side of the wire. The effective low-energy Hamiltonian then is

$$\begin{aligned}
H = & H_L + i\varepsilon\gamma_1\gamma_2 + \varepsilon_D d^\dagger d \\
& - i\gamma_1[t_1 \cos(\phi)\psi + t_1 \cos(\phi)\psi^\dagger + it_2 \sin(\phi)d - it_2 \sin(\phi)d^\dagger] \\
& - i\gamma_2[it_1 \sin(\phi)\psi - it_1 \sin(\phi)\psi^\dagger + t_2 \cos(\phi)d + t_2 \cos(\phi)d^\dagger], \quad (2.24)
\end{aligned}$$

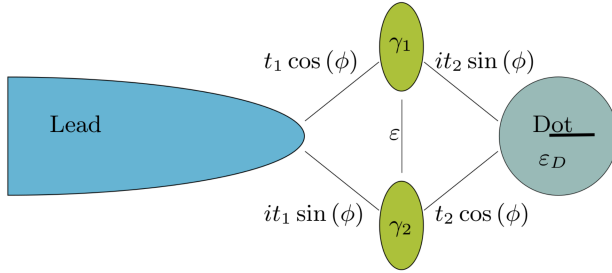
where  $H_L$ ,  $\gamma_i$  and  $\psi$  are the same operators as before and  $t_1$  and  $t_2$  are real valued. We choose the parametrization using the angle  $\phi$  so that we can continuously tune between a pure Majorana like coupling ( $\phi = 0$ ) and a pure Dirac like coupling ( $\phi = \pi/4$ ). We choose the angle to be the same for the coupling to the lead and for the coupling to the dot, because of the spatial symmetry of an isolated Kitaev chain.

The CGF for this setup has the same form as the CGF in Eq. (2.7) which means that Andreev reflection is still the only process contributing to transport, however the Andreev reflection probability is different. In Fig. 2.6 (b) we show the differential conductance as function of dot level energy for different non-local coupling angles  $\phi$ .

## 2. Fano resonances in spinless Majorana bound states-...

---

(a)



(b)

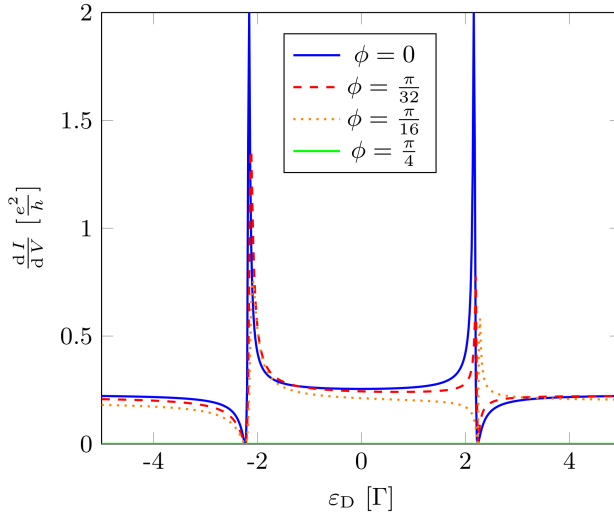


**Figure 2.6.:** (a) Sketch of the extended setup. By varying the parameter  $\phi$  we can tune the system from pure Majorana-like coupling ( $\phi = 0$ ) to pure Dirac-fermion-like coupling ( $\phi = \frac{\pi}{4}$ ), in order to find unique signatures of coupling to a single MBS. (b) Differential conductance in the extended setup for different  $\phi$ . In the Majorana coupling case  $\phi = 0$  the Fano resonances are quantized and are mirrored at  $\varepsilon_D = 0$  due to the real valued properties of the Majorana fermion. For  $0 < \phi < \frac{\pi}{4}$  the resonances are no longer quantized and the peaks are no longer symmetric. Parameters are  $eV = 3\Gamma$ ,  $|t_2| = \Gamma$ ,  $\varepsilon = 0.4\Gamma$ . Figure and caption taken from Ref. [138]. ©[2017] American Physical Society.

For pure Majorana-like couplings we restore the symmetric results from Sec. 2.1. In the case of pure Dirac-like couplings the transport is completely blocked. Because the lead and the dot couple to single normal Dirac fermionic degree of freedom, the superconductivity is effectively shut off, and therefore no Andreev processes are possible. In between pure Majorana-like and Dirac-like couplings ( $0 < \phi < \pi/4$ ), the emerging Fano resonances are no longer symmetric with respect to each other. Depending on the parameters the sign of the asymmetry parameter of both resonances can even be the same (see Fig. 2.6 (b)  $\phi = \pi/16$ ). Moreover, the Fano resonances are no longer quantized to  $2e^2/h$ .

The loss of symmetry regarding the Fano resonances can be explained with asymmetric hybridizations between the non-local fermion composed of the two MBSs and the electron and hole degree of freedom of the quantum dot, respectively. Fig. 2.7 shows the differential conductance as a function of applied bias voltage energy and dot level energy. The resonances in the differential conductance again correspond to the spectrum as the differential conductance also probes the density of states. The different hybridizations for positive and negative dot level energy can be clearly identified. To understand this on a mathematical level we take a look at the Hamiltonian from Eq.(2.24) without the attached lead and rewrite the MBS operators in regular Dirac fermion operators  $\gamma_1 = f^\dagger + f$  and

## 2. Fano resonances in spinless Majorana bound states...

---

$$\gamma_2 = i(f^\dagger - f)$$

$$\begin{aligned} H = & 2\varepsilon(f^\dagger f - \frac{1}{2}) + [t_2 \sin(\phi) + t_2 \cos(\phi)]f^\dagger d + [t_2 \sin(\phi) - t_2 \cos(\phi)]fd \\ & - [t_2 \sin(\phi) - t_2 \cos(\phi)]f^\dagger d^\dagger + [t_2 \sin(\phi) + t_2 \cos(\phi)]fd^\dagger \\ & + \varepsilon_D d^\dagger d. \end{aligned} \quad (2.25)$$

This Hamiltonian is only invariant (up to a constant) under the transformation  $d \rightarrow d^\dagger$ ,  $d^\dagger \rightarrow d$  and  $\varepsilon \rightarrow -\varepsilon$  if  $\phi = 0$  which shows that any non-Majorana-like coupling destroys the dot-particle-hole symmetry.

Recent experiments including a quantum dot coupled to a Majorana nanowire [106, 113] showed that the differential conductance in the low-energy sector shows asymmetric hybridizations between the electron and hole states and an in-gap low-energy state. In Ref. [113] they also analyzed this hybridization following a similar formalism that we used to measure a so called quality factor [152, 153]  $q = 1 - \tan(\phi)$ , which quantifies the “Majoraneness” of the coupling between dot and Majorana nanowire. In the reported experiments they were able to achieve quality factors of up to  $q = 0.97$  which is consistent with highly non-local MBSs. In their experiments Deng et al. were not able to see Fano resonances because the quantum dot was created between the lead and the Majorana nanowire, so that all transport paths include the quantum dot.

### 2.4.2. Long-range Couplings to the Kitaev Chain

In order to connect our low-energy analysis including the non-local couplings and our numerical calculation using a full Kitaev chain we extend the tunnel Hamiltonian from the Kitaev chain to the lead and the dot. We consider a coupling to every single site of the chain, but with exponentially decreasing amplitude over the length of the wire. The modified tunneling Hamiltonian then can be written as

$$H_T = \sum_{n=1}^N \left( t_L e^{-\frac{(n-1)a}{\xi}} \psi^\dagger c_n + t_D e^{-\frac{(N-n)a}{\xi}} c_n^\dagger d + h.c. \right), \quad (2.26)$$

where  $\xi$  is a length scale on which the tunneling amplitude decreases. In Fig. 2.8 we show the resulting differential conductance as function of dot level energy for two different decay lengths  $\xi$ . In both cases we can again

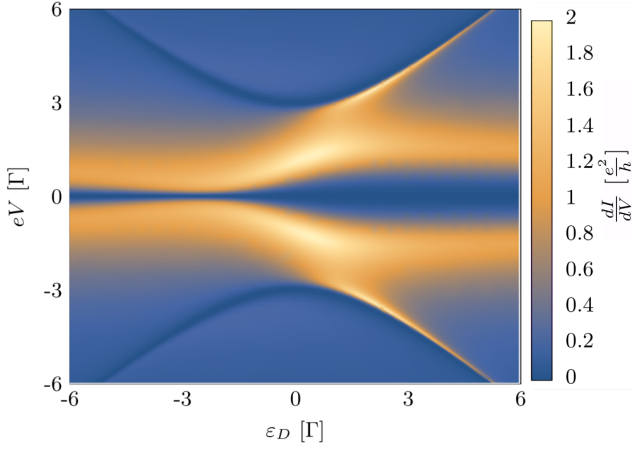


**Figure 2.7.:** Differential conductance as function of dot level energy and bias voltage for non-Majorana fermionic couplings with  $\phi = 0.4$ ,  $\varepsilon = 0.5\Gamma$ ,  $|t_2| = 1.5\Gamma$ . The maxima of the differential conductance correspond to the eigenenergies of the system without the lead. Figure and caption taken from Ref. [138]. ©[2017] American Physical Society.

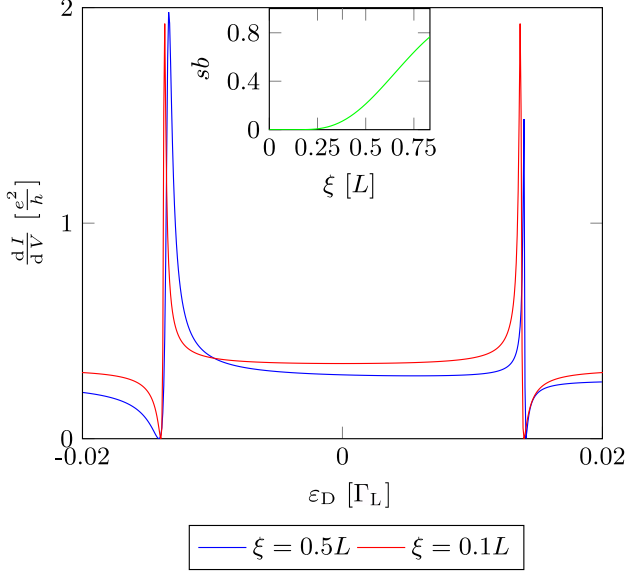


**Figure 2.8.:** Fano resonances in the Kitaev chain for non-trivial couplings to normal conducting lead and QD using  $t_D = 0.15\Gamma_L$ . The other parameters are the same as in Fig. 2.5 (a). In the case of long range couplings ( $\xi = 0.5L$ ) the two Fano resonances are no longer symmetric. For a shorter decay length ( $\xi = 0.1L$ ) the symmetry of the two FRs is restored. The inlay shows the symmetry breaking parameter  $sb = (p(\varepsilon_D = eV) - p(\varepsilon_D = -eV))/p(\varepsilon_D = eV)$  vs. the tunneling decay length. Figure and caption taken from Ref. [138]. ©[2017] American Physical Society.

identify the two Fano resonances. In the case of the longer decay length  $\xi = 0.5L$  the symmetry of the two resonances is broken, while it is restored in the case of  $\xi = 0.1L$ . This is in agreement with our interpretation of the analytical model, because in the case of the shorter decay length only a single MBS is accessible for lead and quantum dot, respectively. In order to quantify the symmetry breaking induced by the non-local couplings we introduce the symmetry breaking parameter

$$sb = (p(\varepsilon_D = eV) - p(\varepsilon_D = -eV))/p(\varepsilon_D = eV), \quad (2.27)$$

which is shown in the inlay of Fig. 2.8. It can be clearly seen that the symmetry of the Fano resonances is intact until the decay length exceeds the Majorana coupling length (for the chosen parameters  $\xi_M = 0.244L$ ). This is again in accordance with the analytical model which predicts the loss of symmetry as soon as both Majorana wave functions are accessible by electron tunneling.

## 2.5. Conclusion

To summarize, we have calculated the electron transfer between a spinless lead and an MBS-quantum dot hybrid system. To perform this calculations we resorted to full counting statistics, a Keldysh Green's function based formalism. The cumulant generating function showed that the only process that contributes to transport is Andreev reflection. The probability for this Andreev reflection characterizes the transport in the considered setup completely. Resonances in the Andreev reflection probability correspond to the spectrum of the considered setup without an attached lead. This spectrum shows hybridizations of the electron-like and hole-like states on the quantum dot with the MBSs.

Fano resonances emerge in the differential conductance as a function of dot level energy. These Fano resonances always come in pairs (one for the electron and one for the hole degree of freedom of the quantum dot).

In the case of lead and quantum dot coupling to only one MBS each, we presented that the differential conductance can be described with the Fano-Beutler formula which proves that the observed line shapes are in fact Fano resonances. The two emerging Fano resonances are mirrored at zero dot level energy. We also expressed the three parameters describing a Fano resonance in terms of the microscopic parameters of our setup.

## 2. Fano resonances in spinless Majorana bound states-...

---

And showed that a sign change in the asymmetry parameter of a single Fano resonance can be used to measure the splitting energy of the MBSs. Moreover, we showed that the resulting Fano resonances are quantized to  $2e^2/h$ .

When considering extended couplings where both MBSs couple to the lead and to the dot we found that the symmetry of the two Fano resonances as well as their quantization is lost. In the special case of equal tunnel amplitudes to both MBSs, the electron transport is even completely blocked.

We support our effective model findings with the numerical analysis of a full Kitaev chain coupled to a quantum dot at one end and to a lead at the other end. We showed a good agreement with our analytic results in the low-energy sector. We showed that the Fano resonances persist at finite temperature and that even though their quantization is lost, the symmetry of the two Fano resonances with respect to each other remains. In addition, we showed that a long ranged coupling between Kitaev chain and quantum dot and lead respectively can lead to the breaking of the symmetry of the two Fano resonances. Long range in this context means that tunneling amplitudes connecting the lead and the dot with the Kitaev chain can reach the Majorana wave function of the MBS located at the opposite side of the wire.

We showed that the symmetry of the Fano resonances can only be accomplished if the MBSs can be addressed individually which corresponds to them being spatially separate. Thus, we consider it to be a unique signature of coupling to a single MBS which goes beyond the quantized differential conductance.



### 3. Signatures of the Majorana spin in the electrical transport in a Majorana nanowire

In the previous chapter, we considered a Kitaev chain as the system in which the MBSs emerge. However, the Kitaev chain is more of a toy system that is not realized directly in nature. A more experimentally relevant system in that MBSs can be found as topologically protected boundary states are the Majorana nanowires which we have introduced in Chap. 1.1.3. Recently, there have been experimental reports of coupling quantum dots to low-energy states in these Majorana nanowires [106,113]. The experimental results showed different hybridizations of spin polarized electron- and hole-like quantum dot states with the close to zero energy state which can be explained by a coupling to both emerging MBSs [138, 152, 153, 170]. Generally, both MBSs can be accessible by tunneling to the dot state, because their wave functions decay exponentially into the wire which means that if the wire is not long enough, the wave functions of both MBSs have a finite weight at the interface with the quantum dot (and/or a lead).

In addition, it was pointed out that near-zero-energy bound states can emerge rather generically in a tunneling junction if there is a non-superconducting section between the tunneling barrier and the Majorana nanowire [142, 144, 154, 170–175]. Some of these low-energy modes can be already distinguished from topological MBSs, because they are only zero energy states for fine-tuned parameters. However, some of them are pinned to zero or close to zero energy over a wide range of parameters [141, 142, 154, 156, 170–178]. These pinned modes are also dubbed non-topological MBSs or quasi-MBSs [179] and have been shown to mimic

### 3. Signatures of the Majorana spin in the electrical transport . . .

---

many signatures of topologically non-trivial MBSs [118, 141, 142, 174, 175]. So that additional signatures for topologically non-trivial MBSs in the Majorana nanowires are needed.

Another tool to discriminate between topologically non-trivial MBSs and topologically trivial MBSs is the spin-canting angle of the Majorana wave function. Because of the interplay of the Zeeman field with Rashba spin orbit coupling there is no fixed spin quantization axis in the nanowires. This leads to a non-trivial spin structure of the Majorana wave functions [152, 180–182]. This non-trivial spin structure can lead to different spin-canting angles for the two MBSs at the same spatial position and thus can also have an influence on transport properties [140, 152].

Also, to distinguish between topologically non-trivial MBSs and non-topological MBSs non-local measurements schemes can be employed, because topological MBSs should always emerge on both ends of the nanowire. The non-local probe could be a quantum dot contacting the MBSs as discussed in the previous chapter or truly non-local probes using two leads [115, 116] which has been realized in experiments recently [183–185].

In this chapter, we consider two setups. First, we take a look at a Majorana nanowire that is tunnel contacted by a spinful normal conducting lead. We focus on the finite size of the nanowire that allows us to couple the lead to both MBSs which can have different spin-canting angles at the tunneling interface. The second setup under consideration is a Majorana nanowire that is coupled to a lead on one side and a quantum dot on the other side. What differentiates this setup from the one in the previous chapter is that we use a spinful lead and quantum dot and we find that the additional spin degree of freedom leads to further signatures in the transport characteristics.

To calculate the transport properties in these setups we use an effective low-energy approach together with full counting statistics. The calculated cumulant generating function shows that only Andreev reflection in two channels contributes to the transport in both setups. In the case without quantum dot we show that the probability for an Andreev reflection becomes a function of spin-canting angle difference of the two MBSs and that the transport in one channel is blocked if the spins of the two MBSs are the same or only one MBS is contacted by the lead. In the case with dot we show that pairs of Fano resonances emerge as a function of dot level energy. We find that the symmetry relation within each of these

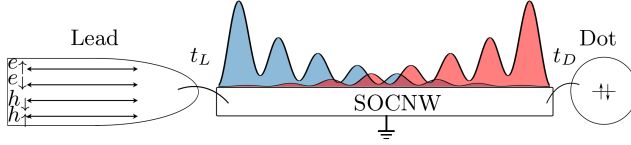


**Figure 3.1.:** Schematic representation of the setup under consideration. The normal spinful lead contains two electron (up, down) and two hole (up, down) channels. We assume a point-like tunneling from the lead ( $t_L$ ) and dot ( $t_D$ ) to the corresponding ends of the nanowire. Blue (red) are the calculated Majorana wave functions of the left (right) ends of the grounded spin orbit coupled Majorana nanowire (SOCNW). Caption and figure taken from Ref. [139]. ©[2020] American Physical Society.

pairs can be used to distinguish if the dot couples to only one or both MBSs in the nanowire.

In this chapter, we present the results of our publication [139]. The rest of the chapter is organized as follows. We introduce the full model Hamiltonian in Chap. 3.1 and describe the low-energy physics of the full model by using an effective Hamiltonian that we present in Chap. 3.2. To calculate the transport properties by using full counting statistics the cumulant generating function has to be calculated. The calculation of it is presented in Chap. 3.2.1. In Chap. 3.2.2, we apply full counting statistics to the spinful lead-Majorana nanowire setup. Next, we consider the setup in which an additional quantum dot is tunnel coupled to the Majorana nanowire at the side opposite to the lead in Chap. 3.2.3. Finally, in Chap. 3.3 we extend the transport calculations of the effective models by employing a numerical scattering matrix approach to the full Majorana nanowire Hamiltonian.

## 3.1. Full Model Hamiltonian

We consider a Majorana nanowire which is tunnel coupled to a spinful normal metallic lead on one side and to a quantum dot on the other side as depicted in the sketch in Fig 3.1. The Hamiltonian describing this system

$$H = H_M + H_L + H_D + H_T, \quad (3.1)$$

### 3. Signatures of the Majorana spin in the electrical transport . . .

---

can be split up in four individual parts. The first part describes the topological superconductor. We use the Bogoliubov-de Gennes formalism for the Majorana nanowire

$$H_M = \frac{1}{2} \int_0^L \Psi^\dagger(x) \mathcal{H}_{BdG}^{NW} \Psi(x) dx, \quad (3.2)$$

where  $L$  is the length of the nanowire and  $H_{BdG}^{NW}$  is presented in the Nambu basis with  $\Psi(x) = [\psi_\uparrow(x), \psi_\downarrow(x), \psi_\downarrow^\dagger(x), -\psi_\uparrow^\dagger(x)]^T$ , and

$$\mathcal{H}_{BdG}^{NW} = \left[ \left( -\frac{\hbar^2}{2m^*} \partial_x^2 - \mu \right) - i\alpha \partial_x \sigma_y \right] \tau_z + V_Z \sigma_z + \Delta \tau_x. \quad (3.3)$$

Here,  $m^*$  is the effective electron mass,  $\mu$  is the chemical potential,  $\alpha$  is the Rashba parameter,  $V_Z$  is the Zeeman energy and  $\Delta$  is the induced  $s$ -wave pairing. The Pauli matrices  $\sigma_i$  and  $\tau_i$  act in the spin and particle-hole space, respectively. The topological non-trivial phase with emerging MBSs is present for  $V_Z > \sqrt{\Delta^2 + \mu^2}$  [53, 54]. For the lead we assume a linearized dispersion relation

$$H_L = -i\hbar v_F \sum_\sigma \int dx c_\sigma^\dagger(x) \partial_x c_\sigma(x), \quad (3.4)$$

where  $c_\sigma^\dagger(x)$  creates an electron with spin  $\sigma$  at position  $x$  in the lead. Here, we neglect effects that dominate at the band bottom (Zeeman effect and spin-orbit coupling), because of the large Fermi energy in a metallic lead. For the quantum dot we assume a single level with energy  $\varepsilon_D$  that is Zeeman split with the same Zeeman field strength as in the wire, because in previous experiments [106, 113] the quantum dot was formed by gating inside the semiconducting nanowire. Double occupancy of the quantum dot leads to an additional charging energy  $U$ , so that the Hamiltonian is given by

$$H_D = \sum_{\sigma, \sigma'} d_\sigma^\dagger [\varepsilon_D \sigma_0 + V_Z \sigma_z]_{\sigma\sigma'} d_{\sigma'} + U n_\uparrow n_\downarrow, \quad (3.5)$$

where  $d_\sigma^\dagger$  creates an electron with spin  $\sigma$  on the dot and  $n_\sigma = d_\sigma^\dagger d_\sigma$  counts the number of electrons with spin  $\sigma$  on the dot. We treat the Coulomb interaction using a mean field approximation [152]

$$U n_\uparrow n_\downarrow \approx U (n_\uparrow \langle n_\downarrow \rangle + \langle n_\uparrow \rangle n_\downarrow - \langle n_\uparrow \rangle \langle n_\downarrow \rangle). \quad (3.6)$$

In the mean field approximation, quadratic fluctuations in the dot occupation number are neglected, so that the approximation works best in the Coulomb valley as fluctuations are smaller away from points in parameter space at which the occupation of the dot changes. Also, interaction effects like the Kondo effect are beyond the mean field approximation [186]. However, the applied Zeeman field suppresses the Kondo correlations (for  $\Delta_Z$  larger than the Kondo temperature).

We assume a point-like tunneling between the end of the lead and one end of the nanowire with amplitude  $t_L$  as well as a tunneling between the dot and the other side of the nanowire with amplitude  $t_D$

$$H_T = \sum_{\sigma} t_L c_{\sigma}^{\dagger}(0) \psi_{\sigma}(0) + t_D d_{\sigma}^{\dagger} \psi_{\sigma}(L) + h.c.. \quad (3.7)$$

If not explicitly stated otherwise we will use the parameters  $m^* = 0.015m_e$  where  $m_e$  is the electron rest mass,  $\alpha = 20$  meVnm and  $\Delta = 0.5$  meV. With these realistic parameters we do not aim for a quantitative agreement with the experiments, but show rather qualitatively the existence of the proposed signatures.

## 3.2. Low Energy Effective Model

Because we are interested in the transport signatures of the MBSs, we introduce an effective low-energy model for the Majorana nanowire. The finite size of the wire leads to an energy splitting  $\varepsilon$  of the non-local fermion  $\eta = (\gamma_1 + i\gamma_2)/2$  composed of the two MBSs which can be described with the Hamiltonian

$$H_{\text{MEff}} = i\varepsilon\gamma_1\gamma_2, \quad (3.8)$$

where  $\gamma_i = \gamma_i^{\dagger}$  is the self-hermitian creation/annihilation operator generating the  $i$ -th MBS and these operators obey the anti commutator relation  $\{\gamma_i, \gamma_j\} = 2\delta_{ij}$ . In this low-energy approach the annihilation operator for the electrons in the Majorana nanowire can be written in terms of the Majorana operators  $\psi_{\sigma}(x) = \Lambda_{1\sigma}(x)\gamma_1 + \Lambda_{2\sigma}(x)\gamma_2$ , where  $\Lambda_{i\sigma}(x)$  is the electronic part of the spinor wave function of the  $i$ -th MBS. It is convenient

### 3. Signatures of the Majorana spin in the electrical transport ...

---

to use the parametrization

$$\begin{aligned}
t_L \Lambda_{i\uparrow}(0) &= t_i \cos\left(\frac{\Theta_i(0)}{2}\right) \equiv t_{Li\uparrow}, \\
t_L \Lambda_{i\downarrow}(0) &= t_i \sin\left(\frac{\Theta_i(0)}{2}\right) \equiv t_{Li\downarrow}, \\
t_D \Lambda_{i\uparrow}(L) &= t_{Di} \cos\left(\frac{\Theta_i(L)}{2}\right) \equiv t_{Di\uparrow}, \\
t_D \Lambda_{i\downarrow}(L) &= t_{Di} \sin\left(\frac{\Theta_i(L)}{2}\right) \equiv t_{Di\downarrow},
\end{aligned} \tag{3.9}$$

with the spin-canting angle  $\Theta_i(x)$  of the  $i$ -th Majorana wave function at position  $x$  in the nanowire. Because we base our effective Hamiltonian on Eq. (3.3), we find for the spin-canting angles  $\Theta_1(0) = \Theta_2(L) = \Theta_1$  and  $\Theta_2(0) = -\Theta_1(L) = \Theta_2$ . With this the tunnel Hamiltonian can be written as

$$\begin{aligned}
H_{\text{TEff}} = \sum_{i=1}^2 t_i \cos\left(\frac{\Theta_i(0)}{2}\right) c_{\uparrow}^{\dagger}(0) \gamma_i + t_i \sin\left(\frac{\Theta_i(0)}{2}\right) c_{\downarrow}^{\dagger}(0) \gamma_i \\
+ t_{Di} \cos\left(\frac{\Theta_i(L)}{2}\right) d_{\uparrow}^{\dagger} \gamma_i + t_{Di} \sin\left(\frac{\Theta_i(L)}{2}\right) d_{\downarrow}^{\dagger} \gamma_i + h.c.. \tag{3.10}
\end{aligned}$$

Also, we assume that the dot is only weakly coupled to the wire, so that we approximate the expectation values for the occupation of the dot with those of a completely isolated dot at zero temperature

$$\begin{aligned}
\langle n_{\uparrow} \rangle &= \vartheta(-U - V_Z - \varepsilon_D) \\
\langle n_{\downarrow} \rangle &= \vartheta(V_Z - \varepsilon_D),
\end{aligned} \tag{3.11}$$

where  $\vartheta(x)$  is the Heaviside function. We perform this approximation, because the analytical self-consistent treatment of the mean field approximation is in general not possible. In the following sections we use that the Heaviside function can be written as  $\vartheta(x) = \lim_{n \rightarrow 0} (1/2 + 1/\pi \arctan(x/n))$ . However, instead of performing this limit we use  $n = 10^{-4}$  for all plots.

### 3.2.1. Cumulant Generating Function

To calculate the cumulant generating function (CGF) we transform the dot creation and annihilation operators into a Majorana basis

$$\begin{aligned} d_{\uparrow}^{\dagger} &= \frac{1}{2} (\gamma_3 + i\gamma_4) \\ d_{\downarrow}^{\dagger} &= \frac{1}{2} (\gamma_5 + i\gamma_6), \end{aligned} \quad (3.12)$$

to obtain the Hamiltonians

$$H'_{\text{M}} = \frac{i}{2} \sum_{\mu\nu} A_{\mu\nu} \gamma_{\mu} \gamma_{\nu}, \quad (3.13)$$

$$H'_{\text{T}} = t_i \cos\left(\frac{\Theta_i}{2}\right) c_{\uparrow}^{\dagger}(0) \gamma_i + t_i \sin\left(\frac{\Theta_i}{2}\right) c_{\downarrow}^{\dagger}(0) \gamma_i + h.c.,$$

where the matrix  $A$  is a real valued skew symmetric matrix containing the splitting energy, the dot level energy, the Coulomb energy in the mean field approximation and the couplings between the MBS and the quantum dot. So that the full Hamiltonian of the low-energy systems is  $H = H'_{\text{M}} + H'_{\text{T}} + H_{\text{L}}$ . To calculate the CGF we use the Levitov-Lesovik formula [167, 187]. A detailed derivation of this formula is shown in App. A where we closely follow the calculations of Ref. [116]. In order to include the spinful lead, we treat the two spin channels as independent leads with the same counting field  $\lambda$ . The CGF is then given by

$$\ln \chi(\lambda) = \frac{\mathcal{T}}{2} \int \frac{d\omega}{2\pi} \ln \left[ \frac{\det ([D^{\lambda}]^{-1}(\omega))}{\det ([D^{\lambda=0}]^{-1}(\omega))} \right], \quad (3.14)$$

where the inverse full Majorana Green's function  $[D^{\lambda}]^{-1}(\omega) = [D^{(0)}(\omega)]^{-1} - \Sigma^{\lambda}(\omega)$  is a  $12 \times 12$  matrix (2 for the MBS, 4 for the electron and hole degree of freedom on the dot and doubled because of the Keldysh formalism). Here,  $D^{(0)}(\omega)$  is the unperturbed Majorana Green's function, the Fourier transform of  $[D^{(0)}(t, t')]_{\alpha\beta} = -i \langle T_{\mathcal{C}} \gamma_{\alpha}(t) \gamma_{\beta}(t') \rangle$ , and  $\Sigma^{\lambda}(\omega)$  is the Fourier transform of the selfenergy containing the counting fields

$$\begin{aligned} \Sigma_{\alpha\beta}^{\lambda}(t, t') &= \sum_{\sigma} \left[ -t_{L\alpha\sigma} t_{L\beta\sigma}^{*} e^{-i \frac{\lambda(t) - \lambda(t')}{2}} G_{\sigma}(t, t') \right. \\ &\quad \left. + t_{L\beta\sigma} t_{L\alpha\sigma}^{*} e^{i \frac{\lambda(t) - \lambda(t')}{2}} G_{\sigma}(t', t) \right], \end{aligned} \quad (3.15)$$

### 3. Signatures of the Majorana spin in the electrical transport . . .

---

where  $G_\sigma(t', t) = G_\sigma(x' = 0, x = 0, s', s) = -i \langle T_C \hat{c}_\sigma(0, s') \hat{\bar{c}}_\sigma(0, s) \rangle$  is the unperturbed lead boundary Green's function for spin  $\sigma$ . Detailed calculations for the unperturbed Majorana Green's function can be found in App. B. If we insert the calculated Green's functions in Eq (3.14) we find for the CGF

$$\ln \chi(\lambda) = \frac{\mathcal{T}}{2\hbar} \sum_{i=\pm} \int \frac{dE}{2\pi} \ln \left[ 1 + p_i (e^{-2ei\lambda} - 1) n(E) n(-E) + p_i (e^{2ei\lambda} - 1) (n(E) - 1) (n(-E) - 1) \right], \quad (3.16)$$

where  $n(E) = \frac{1}{1+e^{\beta(E-eV)}}$  is the Fermi function in the lead with  $\beta = 1/k_B T$  the inverse thermal energy,  $k_B$  is the Boltzmann constant and  $V$  the bias voltage between the lead and the grounded superconductor,  $\mathcal{T}$  is the large measuring time and  $e$  is the elementary charge. At zero temperature the CGF simplifies even more to

$$\ln \chi(\lambda)|_{T=0} = \frac{\mathcal{T}}{2\hbar} \sum_{i=\pm} \int_{-eV}^{eV} \frac{dE}{2\pi} \ln \left[ 1 + p_i(E) (e^{-2ei\lambda} - 1) \right]. \quad (3.17)$$

This CGF describes a binomial process in which two electrons are transferred across the junction in two independent channels  $\pm$  with the probability  $p_i$ , respectively. The process which transfers two electrons in the single particle picture is Andreev reflection where an incoming electron is back scattered as an outgoing hole. There are two channels for the Andreev reflection, because of the two spin channels in the normal conducting lead. The first two transport cumulants follow by simply taking the derivative of the CGF with respect to the counting field

$$\begin{aligned} I &= \frac{i}{\mathcal{T}} \frac{d}{d\lambda} \ln \chi(\lambda), \\ S &= -\frac{1}{\mathcal{T}} \frac{d^2}{d\lambda^2} \ln \chi(\lambda), \end{aligned} \quad (3.18)$$

where  $I$  is the average current and  $S$  is symmetrized zero frequency noise.

#### 3.2.2. Transport without quantum dot

In the following section, we want to focus on the case in which the dot is decoupled from the Majorana system, i.e.  $t_D = 0$ , and find the influ-



ences of the finite size of the considered Majorana nanowire on the transport characteristics. This simplified setup has already been considered in the literature, but these previous works only focused on parallel [188] or anti-parallel [142] Majorana spins, respectively. These special cases are included in our model for  $\Theta_1 = \Theta_2$  (parallel) and  $\Theta_1 - \Theta_2 = \pi$  (anti-parallel) and our findings are consistent with the results of these previous works.

Here, we find that the Andreev reflection probabilities

$$p_{\pm}(E) = 2 \frac{2\Gamma_1\Gamma_2(4\Gamma_1\Gamma_2 + 4\varepsilon^2 + E^2) \sin^2(\frac{\delta\Theta}{2}) + E^2(\Gamma_1 - \Gamma_2)^2}{16(\Gamma_1\Gamma_2 + \varepsilon^2)^2 + 2(2(\Gamma_1^2 + \Gamma_2^2) - 4\varepsilon^2)E^2 + E^4} \pm 2 \frac{\sqrt{(\Gamma_1 - \Gamma_2)^4 E^4 + 4\Gamma_1\Gamma_2 E^2(\Gamma_1 - \Gamma_2)^2(4\varepsilon^2 + 2E^2 + 4\Gamma_1\Gamma_2) \sin^2(\frac{\delta\Theta}{2}) \dots - 16\Gamma_1^2\Gamma_2^2 E^2((\Gamma_1 - \Gamma_2)^2 - 4\varepsilon^2) \sin^4(\frac{\delta\Theta}{2})}}{16(\Gamma_1\Gamma_2 + \varepsilon^2)^2 + 2(2(\Gamma_1^2 + \Gamma_2^2) - 4\varepsilon^2)E^2 + E^4}, \quad (3.19)$$

with  $\Gamma_i = 2\pi\nu(0)|t_i|^2$  and  $\delta\Theta = \Theta_1 - \Theta_2$  are only depending on the spin-canting angle difference and not on the individual angles. This can be explained with the spin rotation invariance of the lead, because we can always choose a spin basis in which the spin of the first MBS is aligned with this basis, so that only the difference to the second MBS matters. Also, in the case of no spin-canting angle difference ( $\delta\Theta = 0$ )  $p_-$  vanishes, as one spin channel in the lead decouples from the Majorana nanowire following the same argument as before. Finally, for  $\Gamma_2 = 0$  we also end up with a single transport channel ( $p_- = 0$ ), because only one MBS can be contacted by the lead. The differential conductance is calculated to be

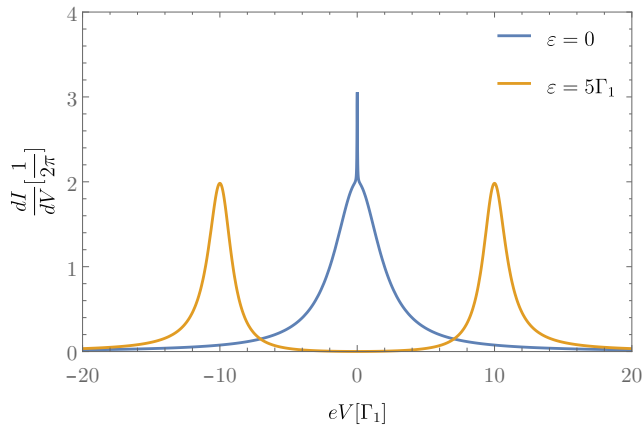
$$\begin{aligned} \frac{dI}{dV} &= \frac{2e^2}{h} (p_+(eV) + p_-(eV)) \\ &= \frac{8e^2}{h} \frac{(eV)^2(\Gamma_1 - \Gamma_2)^2 + 2\Gamma_1\Gamma_2 \sin^2(\frac{\delta\Theta}{2})(4\varepsilon^2 + (eV)^2 + 4\Gamma_1\Gamma_2)}{(4\varepsilon^2 - (eV)^2)^2 + 8\Gamma_1\Gamma_2(4\varepsilon^2 + 2\Gamma_1\Gamma_2) + 4(eV)^2(\Gamma_1^2 + \Gamma_2^2)}. \end{aligned} \quad (3.20)$$

As seen in Fig. 3.2 a) the influence of the coupling to the second MBS is negligible if  $\varepsilon \gg \Gamma_2$ , because the differential conductance shows nearly quantized peaks with height  $2e^2/h$  at the applied bias voltage energy  $eV = 2\varepsilon$  which is expected for coupling to a single MBS. However, if the coupling to the second MBS is much larger than Majorana overlap energy

### 3. Signatures of the Majorana spin in the electrical transport ...

---

(a)



(b)

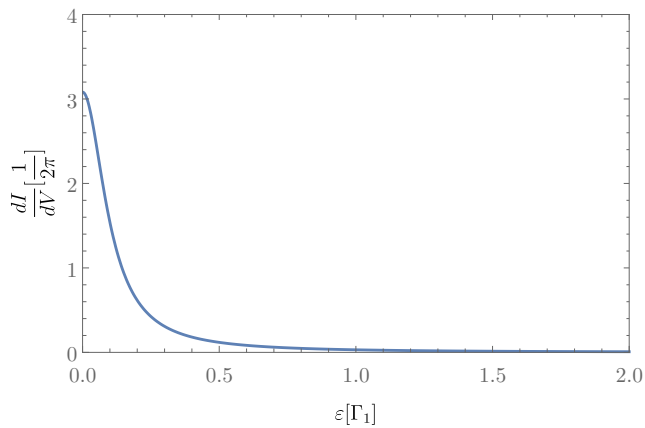


**Figure 3.2.:** Differential conductance in the low-energy model in the setup without QD with finite coupling to both MBS. (a) Differential conductance as a function of bias energy with zero Majorana splitting energy (blue) and finite splitting energy  $\varepsilon = 5\Gamma_1$  (yellow). For  $\varepsilon = 0$ , the differential conductance has the shape of a sum of two Lorentzians with two different widths and deviates strongly from the expected value at the resonance in the case of a coupling to one MBS. Whereas in the case of large splitting energy  $\varepsilon \gg \Gamma_2$ , such deviations at the resonance are very small. (b) Zero bias differential conductance vs Majorana splitting energy. The differential conductance at zero bias is not quantized for  $\varepsilon = 0$  and does not vanish for finite splitting energies. The other parameters are  $\Gamma_2 = 0.01\Gamma_1$  and  $\delta\Theta = \pi - 1$ . Caption and figure taken from Ref. [139]. ©[2020] American Physical Society.

$\varepsilon$  the key signature of quantized differential conductance is lost. For zero-energy MBSs the differential conductance is described by the sum of two Lorentzians whose widths is basically determined by the coupling to the first and second Majorana, respectively. The height of these Lorentzians is not quantized and the sign of it can even be different for both Lorentzians so that the differential conductance at zero bias can assume any value between zero and  $4e^2/h$ . In general, at zero bias voltage the differential conductance is given by

$$\frac{dI}{dV}|_{V=0} = \frac{4e^2}{h} \frac{\Gamma_1\Gamma_2}{\varepsilon^2 + \Gamma_1\Gamma_2} \sin^2\left(\frac{\delta\Theta}{2}\right). \quad (3.21)$$

This again is a Lorentzian, but this time as a function of Majorana splitting energy with its width given by  $\sqrt{\Gamma_1\Gamma_2}$  as shown in Fig. 3.2 b). The height of it can be used to extract the spin-canting angle difference, because it is given by  $4e^2 \sin(\delta\Theta/2)/h$ . It is important to note that Eq. (3.21) was derived with the assumption that either  $\Gamma_2 \neq 0$  or  $\varepsilon \neq 0$ . The emergence of the two different coupling strengths that determine the widths of the Lorentzians can mathematically be understood in the framework of bifurcation of exceptional points [174].

In addition to the differential conductance we can calculate the differential noise

$$\frac{dP}{dV} = \frac{4e^3}{h} (p_+(1 - p_+) + p_-(1 - p_-)). \quad (3.22)$$

### 3. Signatures of the Majorana spin in the electrical transport . . .

---

By measuring both the differential noise and the differential conductance it is possible to calculate the two Andreev reflection probabilities

$$p_{\pm} = \frac{4h}{e^2} \frac{dI}{dV} \mp (\pm) \sqrt{\frac{4h}{e^2} \frac{dI}{dV} - \left( \frac{4h}{e^2} \frac{dI}{dV} \right)^2 - \frac{8h}{e^3} \frac{dP}{dV}}, \quad (3.23)$$

which means that the measurement of these two measurands is enough to fully characterize the transport in this setup. However, because the differential noise is quadratic in the Andreev reflection probabilities there is an ambiguity (“ $(\pm)$ ”) in the calculation of the two probabilities. Physically, this reflects the fact that  $p_-$  and  $p_+$  cannot be distinguished experimentally, because of the spin rotation invariance in the lead.

The influence of finite temperatures on the differential conductance can also be analyzed and is shown in Fig 3.3. We can identify three distinct temperature regimes. The first is the low temperature regime  $k_B T < \Gamma_2$ . In this temperature regime the differential conductance plateaus at its zero temperature value. The second regime is the intermediate temperature regime ( $\Gamma_2 < k_B T < \Gamma_1$ ). Here, depending on the difference between the couplings to the two MBS the differential conductance plateaus at  $2e^2/h$ , the value expected for coupling to a single MBS. In the latter regime at even higher temperatures the differential conductance drops due to the temporal broadening in the lead.

We also calculate the Fano factor

$$F = \frac{S}{eI}, \quad (3.24)$$

which is shown in Fig. 3.24. In general the Fano factor is between 0 and 2. In the case of a large splitting energy  $\varepsilon > \Gamma_i$  there is no qualitative difference of the Fano factor between the case of coupling to only one MBS or the case of an additional small coupling to the second MBS (Fig. 3.4 (a)). In the case of zero energy MBSs, however, the behavior of the Fano factor is fundamentally different at low applied voltages for the case of coupling to only one MBS in contrast to coupling to both MBSs as seen in Fig. 3.4 (b).

In general, we cannot find an analytical expression for the Fano factor, however at zero bias, zero temperature and finite MBS splitting energy we manage to find

$$F|_{V=0} = 2 \frac{\Gamma_1 \Gamma_2 \cos^2\left(\frac{\delta\Theta}{2}\right) + \varepsilon^2}{\Gamma_1 \Gamma_2 + \varepsilon^2} = 2 - \frac{h}{2e^2} \frac{dI}{dV}|_{V=0}. \quad (3.25)$$

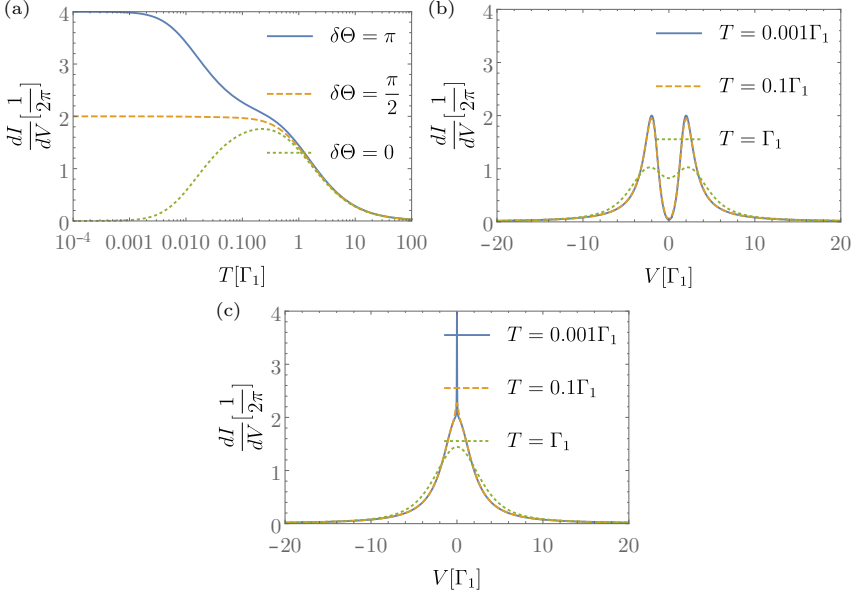


**Figure 3.3.:** Differential conductance in the low-energy model in the setup without QD with finite coupling to both MBS ( $\Gamma_2 = 0.01\Gamma_1$ ) at finite temperature. (a) Differential conductance at zero applied bias voltage energy ( $eV = 0$ ) for three different spin-canting angle differences  $\delta\Theta$  for zero Majorana splitting energy ( $\varepsilon = 0$ ). At very small temperatures ( $k_B T \ll \Gamma_2$ ) the differential conductance shows plateaus. (b) & (c) Differential conductance as a function of applied bias voltage energy at different finite temperatures with spin-canting angle difference  $\delta\Theta = \pi$ . The Majorana splitting energy is finite ( $\varepsilon = \Gamma_1$ ) in (b) and zero in (c). Caption and figure taken from Ref. [139]. ©[2020] American Physical Society.

### 3. Signatures of the Majorana spin in the electrical transport ...

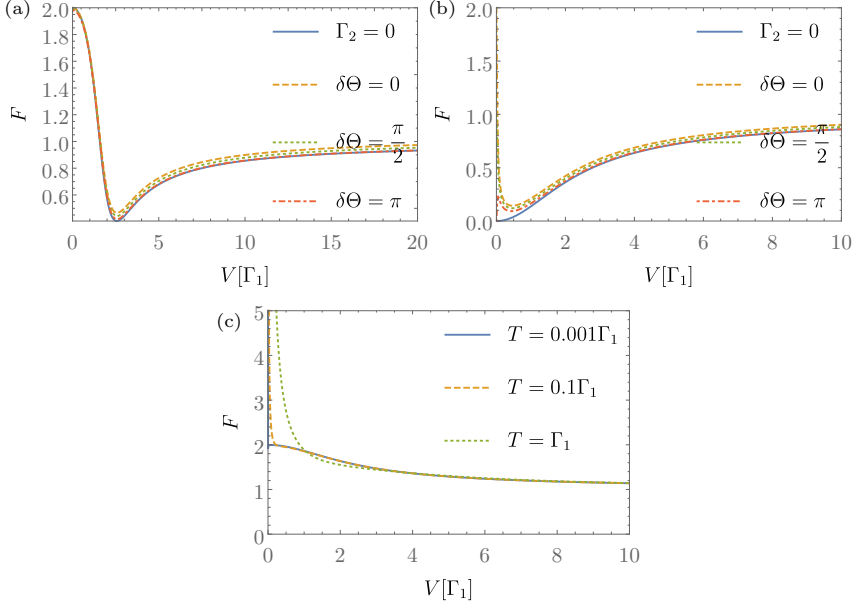


**Figure 3.4.:** Fano factor in the low-energy model as a function of applied bias voltage energy in the setup without QD. If not stated otherwise  $\Gamma_2 = 0.01\Gamma_1$ . (a) & (b) Fano factor for various spin-canting angle differences  $\delta\Theta$  and tunneling rates to the second MBS at zero temperature. In (a) the Majorana splitting energy is finite  $\varepsilon = \Gamma_1$  and in (b) it is assumed to be zero. (c) Fano factor with  $\varepsilon = 0$  and  $\delta\Theta = \pi$  for various temperatures. Caption and figure taken from Ref. [139]. ©[2020] American Physical Society.

In the case of coupling to only one MBS or to only one spin direction the Fano factor at zero bias is quantized to 2. This Fano factor of 2 corresponds to Cooper pairs being transferred between the lead and the superconductor. In the large voltage regime ( $V \rightarrow \infty$ ) the Fano factor is exactly one in the case of coupling to a single MBS. At finite temperatures the Fano factor diverges at zero bias due to the thermal noise. For large bias voltage energies  $eV \gg k_B T$  the zero temperature behavior of the Fano factor is recovered.

#### 3.2.3. Transport properties with quantum dot

Now, in this section we focus on the influence of the quantum dot on the electronic transport. First experiments that suggest the existence of the non-local couplings have been using a quantum dot that is coupled to a Majorana nanowire and a normal conducting lead [106, 113]. Spectrally, this experimental setup has also been analyzed from a theoretical standpoint [152, 153]. In the following, we look at a setup where the dot is not directly contacted by the lead. This difference to the previously mentioned experiments and theoretical works has the advantage that we can probe non-local effects of the MBSs. In this section, we also focus on a low-energy regime.

Because of the spatial symmetry of the Majorana nanowire, we use a fixed ratio for the two couplings to the two MBSs for the tunneling amplitude between Majorana nanowire and lead and the Majorana nanowire and quantum dot, respectively. Then we can use the parametrization

$$\begin{aligned} t_1 &= t \cos(\phi) & t_2 &= it \sin(\phi) \\ t_{D1} &= t_{\text{Dot}} \sin(\phi) & t_{D2} &= it_{\text{Dot}} \cos(\phi), \end{aligned} \quad (3.26)$$

which leads to  $\Gamma = 2\pi\nu_0|t|^2$ . The angle  $\phi$  then controls the strength of non-local couplings, where for  $\phi = 0$  only couplings to the nearest MBS exist (Majorana-like), while for  $\phi = \pi/4$  the couplings to both MBSs are the same (Dirac-like).

First, we note that in contrast to the case without the dot the Andreev reflection probabilities do not only depend on the difference in the spin-canting angles at the junction, but on the two spin cantings themselves. This is due to the fact that the spin rotational invariance on the dot is broken by the applied Zeeman field.

### 3. Signatures of the Majorana spin in the electrical transport ...

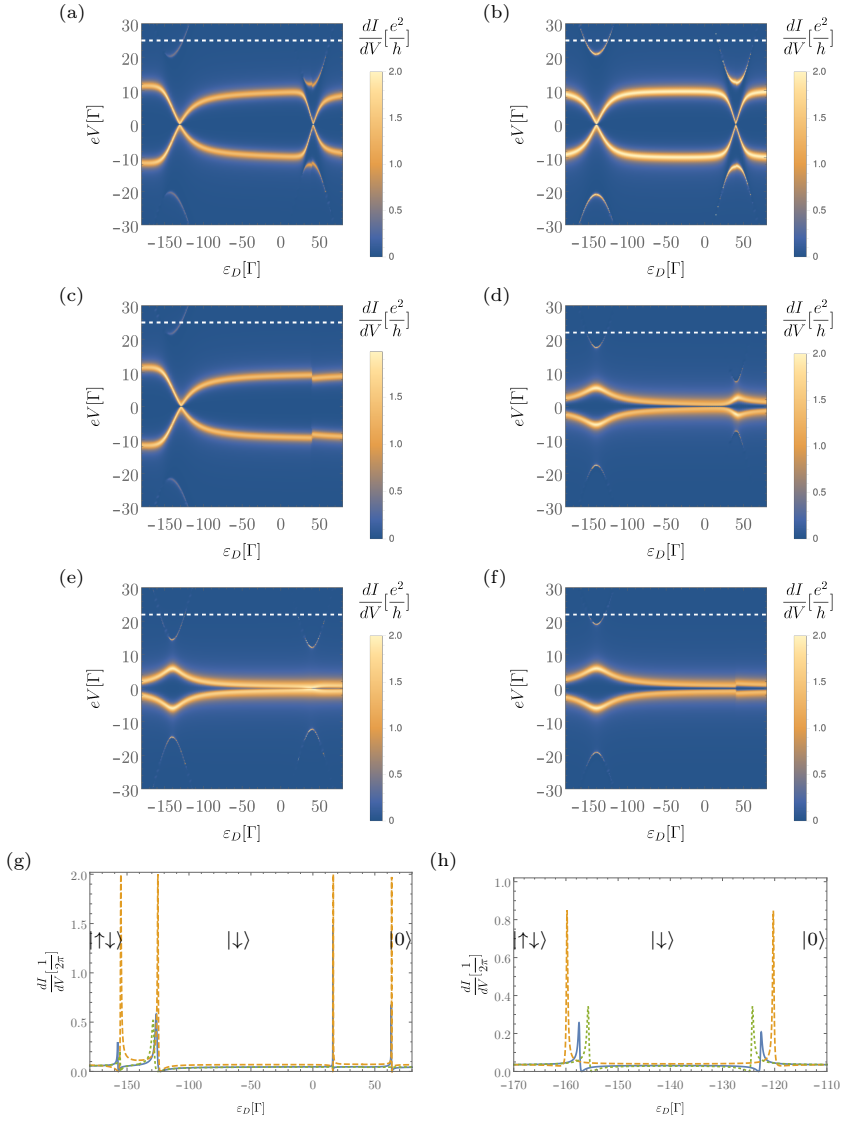




**Figure 3.5.:** (a)-(f) Differential conductance in the low-energy model as a function of applied bias voltage energy  $eV$  and dot level energy  $\varepsilon_D$  with  $t_{\text{Dot}} = 10\Gamma$ ,  $U = 100\Gamma$  and  $V_Z = 40\Gamma$ . (a)-(c) show the differential conductance at finite splitting energy  $\varepsilon = 5\Gamma$ . In (a) and (b) the spin-canting angles are  $\Theta_1 = \Theta_2 = 0.8$ . Here both anticrossings are visible. In (a)  $\phi = 0.3$ . This resulting non-locality manifests in the asymmetry of  $dI/dV$  peaks around the points where the occupancy of the dot changes. In (b)  $\phi = 0$  and the differential conductance shows a bow-tie shape. In (c) we consider  $\phi = 0.3$  and  $\Theta_1 = \Theta_2 = 0$ . Here only the anticrossings around  $\varepsilon_D = U - V_Z$  can be seen. (d)-(f) show the differential conductance at  $\varepsilon = 0$  and  $\phi = 0.3$  for various spin-canting angle configurations ((d)  $\Theta_1 = \Theta_2 = 0.8$ , (e)  $\Theta_1 = 0$ ,  $\Theta_2 = 1.4$ , (f)  $\Theta_1 = \Theta_2 = 0$ ). All plots show a diamond-like lineshape. The dashed lines indicate line cuts shown in (g) & (h) as a function of dot level energy. (g) corresponds to the upper row of plots with  $eV = 25\Gamma$  and (h) corresponds to the lower row of plots with  $eV = 22\Gamma$ . In (g) and (h) the kets denote the spin ground state of the QD that changes when passing a Fano resonance. Caption and figure taken from Ref. [139]. ©[2020] American Physical Society.

The particle-hole symmetry which manifests itself in the Andreev reflection probabilities in form of  $p_{\pm}(eV) = p_{\pm}(-eV)$  is still intact.

If we take a look at the differential conductance as a function of applied bias voltage, we find six resonances for a given set of other parameters which correspond to the eigenenergies of the system without lead. Fig. 3.5 shows that we can identify resonances that correspond to the states on the dot (disperse linear with dot level energy) and that correspond to the MBSs (do not disperse with dot level energy). The states on the dot have an electron-like (positive slope) and a hole-like (negative slope) behavior. Furthermore, we see the hybridization of the MBSs with the quantum dot states. This hybridization can be different for up and down spin states, because of the MBSs spin-canting angles. The shapes of the resonances in Fig. 3.5 (a)-(c) resemble a bow-tie-like form because of the large Majorana splitting while the shapes of the resonances for a small splitting (see Fig. 3.5 (d)-(f)) resemble a diamond-like form. However, the diamond-like lineshape only emerges if the non-local couplings do not vanish. These patterns can be used to analyze the Majorana non-locality

### 3. Signatures of the Majorana spin in the electrical transport . . .

---

as discussed in Ref. [152, 153].

It can also be seen that the approximations we made (mean field approximation and nearly isolated dot) breaks down at points where the occupation of the dot changes and leads to nonphysical discontinuities in the differential conductance. At those degeneracies the fluctuations in the dot occupation are largest and therefore the mean field approximation leads to unphysical results.

The width of the resonances corresponding to the dot states is smaller than those corresponding to the MBSs, because the lead which is responsible for the broadening is coupled directly to the MBSs but only indirectly to the quantum dot.

At fixed bias voltages the differential conductance shows Fano resonances as a function of dot level energies shown in Fig. 3.5 (g) and (h). These resonances arise because two fundamentally different electron paths interfere with each other. The first is a structureless path in which the electrons enter the superconducting Cooper pair condensate directly via an Andreev reflection. The second path involves an incoming electron virtually occupying the dot before entering the Cooper pair condensate. This second path is resonant with respect to the dot level energy while the first is not. This then leads to the emergence of the Fano resonances. We find that these Fano resonances always come in pairs at approximately

$$\varepsilon_{D,res} \approx \begin{cases} -U - V_Z \pm V & \text{where } \langle n_{\uparrow} \rangle \text{ changes,} \\ V_Z \pm V & \text{where } \langle n_{\downarrow} \rangle \text{ changes.} \end{cases} \quad (3.27)$$

For  $V = 0$  these dot level energies correspond to the changes of the occupation number in the ground state of the isolated dot.

In the bias window in which we see the hybridization between the dot states and the MBSs no Fano resonances can be found, because the hybridization makes a distinction of the two path's impossible.

In the case of coupling to only one MBS, these two Fano resonances are approximately symmetric with respect to each other, because a single MBS couples to electron and hole degrees of freedom in the same way. Mathematically, this can be explained if we examine the low-energy Hamiltonian. For a large Zeeman field and large Coulomb interaction  $V_Z, U > \varepsilon$  and for dot level energies  $\varepsilon_D$  where the occupation of the dot can change (i.e. if

### 3.3. Numerical scattering matrix formalism for the full wire model

---

a spin level is close to zero energy) the low-energy physics is described by

$$H_{LE} = i\varepsilon\gamma_1\gamma_2 + \varepsilon_{D2\uparrow(\downarrow)}d_{\uparrow(\downarrow)}^\dagger d_{\uparrow(\downarrow)} + i\gamma_2 \left[ t_{D2\uparrow(\downarrow)}d_{\uparrow(\downarrow)}^\dagger + t_{D,\uparrow(\downarrow)}^* d_{\uparrow(\downarrow)} \right], \quad (3.28)$$

where we projected out the higher energy dot state, accordingly and  $\varepsilon_{D,\sigma} = \varepsilon_D + \sigma V_Z + U \langle n_{\bar{\sigma}} \rangle$ . This Hamiltonian is invariant under the transformation

$$\varepsilon_{D,\uparrow(\downarrow)} \rightarrow -\varepsilon_{D,\uparrow(\downarrow)} \quad d_{\uparrow(\downarrow)} \rightarrow d_{\uparrow(\downarrow)}^\dagger, \quad (3.29)$$

up to a phase that can be gauged away. This reflects the particle-hole symmetry of an isolated MBS and is only present if the dot couples to a single MBS.

The resonances can also be linked to the spin states of the QD. In general, the height of the Fano resonance is only quantized to  $2e^2/h$  for the case of coupling to a single MBS ( $\phi = 0$ ). In this case, the antiresonances also completely block the transport ( $dI/dV = 0$ ). Moreover, because of the intrinsic particle-hole property of a single MBS the Fano resonances corresponding to an electron-like or hole-like state on the QD are symmetric with respect to each other in the case of  $\phi = 0$ . In the case of finite non-local couplings, the quantization of the height is gone and it can be different for the two resonances within a pair.

We also want to note here, that the case of both spins pointing in the same direction along the quantization axis of the spins on the QD is equivalent to the system considered in the previous chapter, because then one spin channel and one spin state on the QD decouples from the Majorana system. However, there are two differences. First, because of the applied Zeeman field and charging energy the occupation number change in the ground state of the isolated dot is shifted in energy. Second, there is the discontinuity due to our approximations (Eq. (3.11)).

### 3.3. Numerical scattering matrix formalism for the full wire model

In this section, we want to connect our analytical low-energy findings to the full Hamiltonian represented in Eq. 3.1. Therefore, we discretize it on

### 3. Signatures of the Majorana spin in the electrical transport ...

---

a chain to obtain a tight binding model of the full system. The discretized Hamiltonian for the nanowire reads

$$H_{\text{Num}} = \sum_{i=1}^N \Psi_i^\dagger \left[ \left( \frac{\hbar^2}{m^* a^2} - \mu \right) \tau_z + V_z \sigma_z + \Delta \tau_x \right] \Psi_i + \sum_{i=1}^{N-1} \Psi_i^\dagger \left[ -\frac{\hbar^2}{2m^* a^2} \tau_z + i \frac{\alpha}{a} \tau_z \sigma_y \right] \Psi_{i+1} + h.c., \quad (3.30)$$

with  $a = \frac{L}{N}$ , where  $N$  is the number of sites of the discretized nanowire. To calculate the transport properties we use a scattering matrix approach which is implemented in the python package Kwant [189]. The scattering matrix

$$S = \begin{pmatrix} S_{ee} & S_{eh} \\ S_{he} & S_{hh} \end{pmatrix}, \quad (3.31)$$

connects the outgoing modes of kind  $i$  with the incoming modes of kind  $j$  with the amplitude  $S_{ij}$ . The modes in the metallic lead are either of electron or of hole kind. The differential conductance at zero temperature is

$$\frac{dI}{dV} = N_e - T_{ee} + T_{eh}, \quad (3.32)$$

where  $N_e$  is the number of propagating electron modes in the lead. The transmission amplitudes  $T_{ij}$ , even though  $T_{ee}$  is actually describing the reflection of an electron, can be calculated from the scattering matrix

$$T_{ij} = \text{Tr} \left( S_{ij}^\dagger S_{ij} \right). \quad (3.33)$$

#### 3.3.1. Without dot

Again, we start by analyzing the system without quantum dot. For Zeeman fields larger than the critical Zeeman field  $V_{ZC} = \sqrt{\Delta^2 + \mu^2}$  the wire is in a topological non-trivial phase which leads to the emergence of close to zero-energy states. Due to the finite size of the nanowire the energy of this state is oscillating with the applied Zeeman field [55, 190] which is shown in Fig. 3.6 (a). The differential conductance at zero bias voltage shows a peak whenever the excitation energy is zero which is to be expected, because the differential conductance probes the local density of states at the end of Majorana nanowire. However, the peak height is

### 3.3. Numerical scattering matrix formalism for the full wire ...

---

not quantized with  $2e^2/h$ , but varies for different oscillation periods. The height of the peak can undercut or exceed the quantized value depending on the applied magnetic field. This indicates that the lead is not only coupled to one MBS but also to the second MBS and following the analytical model that the difference in spin-canting angles is decreasing for each period of the splitting energy oscillations.

In Fig. 3.6 (b) the differential conductance as a function of applied bias voltage at two different fixed Zeeman fields is shown. For the Zeeman field that corresponds to the close to zero energy Majorana splitting the differential conductance can be described as a sum of two Lorentzians with two different widths. It was already pointed out that the width of the second Lorentzians is so small that current state-of-the-art experiments are not able to resolve it properly due to too high temperatures [172]. In the case of a magnetic field that corresponds to the maximum Majorana splitting energy, the differential conductance does not deviate much from the quantized value of  $2e^2/h$  at the resonances which points to a coupling to an isolated MBS. This is consistent with the findings of Peñaranda et al. [170] who showed that the non-local couplings are smallest when the Majorana splitting is maximal.

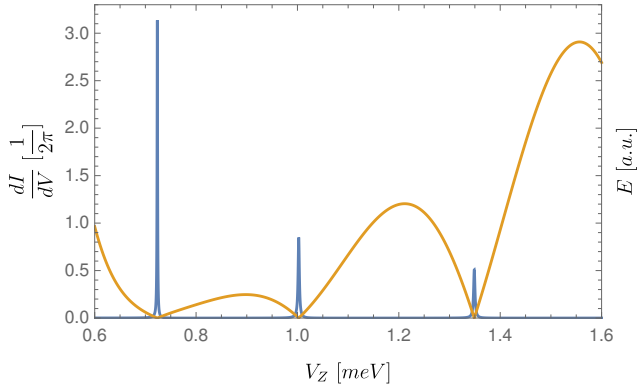
The low-energy transport in both cases can be very well described with the effective model calculations. This is shown by the fits (dashed lines) to the numerical data using Eq. (3.20). What cannot be described with the effective model is the transport due to the higher energy states shown in the inset in Fig. 3.6 (b).

In recent experiments [109], first hints of the non-local couplings could be seen, because the zero bias differential conductance peak exceeded  $2e^2/h$  at low temperatures and large tunnel couplings. However, the full regime was not yet explored, because in these experiments the ratio of  $k_B T/\Gamma$  was still too large to fully resolve a possible coupling to the more distant MBS.

### 3. Signatures of the Majorana spin in the electrical transport ...

---

(a)



(b)

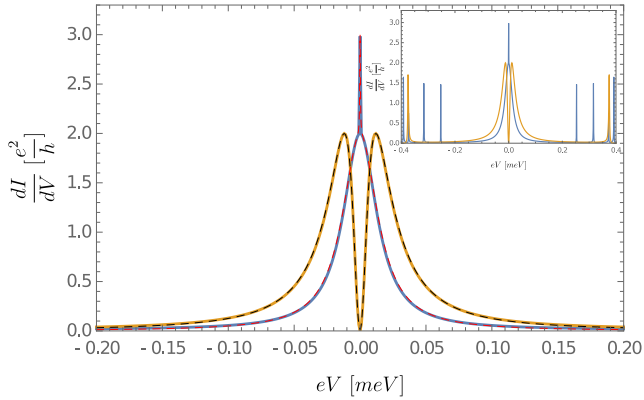


**Figure 3.6.:** (a) Zero bias differential conductance at zero temperature (blue) and energy  $E$  of the lowest energy excitation in the nanowire (yellow) as a function of the applied Zeeman field for the setup without QD. The peaks in the differential conductance correspond to zero energy states in the nanowire. (b) Differential conductance vs. applied bias voltage energy at fixed Zeeman field  $V_Z = 0.7236$  meV (blue) and  $V_Z = 1.2$  meV (yellow). The Zeeman field values correspond to a small Majorana splitting (blue) and large splitting energy (yellow). The dashed lines are fits to the numerical data using Eq. (3.20) with  $\delta\Theta$ ,  $\Gamma_1$  and  $\Gamma_2$  as free parameters. The inset shows the differential conductance for a larger bias voltage energy window which includes higher energy states in the superconducting gap. The other microscopic parameters are  $\mu = 0$ ,  $m^* = 0.015m_e$  where  $m_e$  is the electron rest mass,  $\alpha = 20$  meVnm,  $L = 1.1$   $\mu\text{m}$  and  $\Delta = 0.5$  meV. Caption and figure taken from Ref. [139]. ©[2020] American Physical Society.

#### 3.3.2. Self consistent mean field approach for the quantum dot

So far, the non-local couplings have only been conclusively seen in experiments containing a quantum dot. Therefore, we now turn again to the setup with a quantum dot. To include the quantum dot, we implement the mean field approximation self-consistently. Also, we stay in a regime in which the dot is only weakly coupled to the nanowire in order to ensure the comparability to our effective model calculations, i.e. the hopping between the dot and the nanowire is assumed to be only 10% of the hopping inside the nanowire.

For the self-consistent calculations we start with a finite size system including a finite sized lead with  $M$  sites. From this we extract the quantum dot occupation numbers that we then insert into the open system. A program flow chart for our selfconsistent method can be seen in Fig. 3.7. We start with a given input vector for the spin-up and spin-down ground-state occupation numbers  $\langle n_{in} \rangle$  on the dot and a number of sites for the lead  $M$ . Then, we calculate the expectation value for the number operator on the dot  $\langle n_{out} \rangle$  in the ground state. We check if the difference between

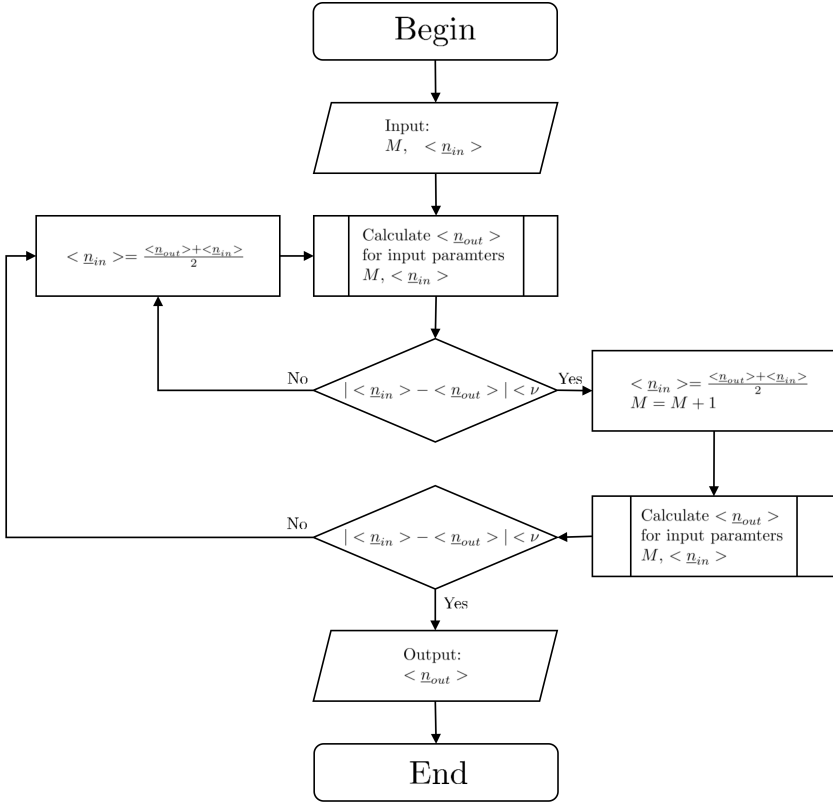


**Figure 3.7.:** Program flow chart for the self-consistent calculation of the QD occupation number. The program contains two loops. In the first loop the QD occupation number  $\langle n \rangle$  is calculated selfconsistently for a fixed number of sites of the lead  $M$ , while the second loop increases the number of sites for the lead until convergence (with small convergence parameter  $\nu$ ). Caption and figure taken from Ref. [139]. ©[2020] American Physical Society.



### 3.3. Numerical scattering matrix formalism for the full wire ...

---

input and output  $|\langle n_{in} \rangle - \langle n_{out} \rangle|$  is larger than a predefined value  $\nu$  (in our case  $\nu = 0.001$ ). If it is we use  $\langle n_{in} \rangle = 0.5(\langle n_{in} \rangle + \langle n_{out} \rangle)$  as the newinput value and start the calculation again. If it is smaller than  $\nu$ , we add a site to the finite size lead set  $\langle n_{in} \rangle = \langle n_{out} \rangle$  and calculate  $\langle n_{out} \rangle$  again. We check again if input and output do not differ more than  $\nu$ . If the system has not converge yet, we start the selfconsistent calculation from the start. However, if it has converged, we use the output as input for the calculation using the scattering matrix formalism. As seen in Fig. 3.8 (f) the occupation of the dot corresponds nearly to that of an isolated dot. The limitations of the self consistent mean field theory is visible as a discontinuity of the occupation number at the transition from a doubly to a singly occupied QD.

To compare the numerical analysis to our effective model calculations, we focus on the topological regime. As seen in Fig. 3.8 (a) this regime is dominated by the oscillating energy of the near zero energy Majorana states. However, not only the MBSs emerge inside the gap, but also other low-energy bound states can be found. The dot states hybridize with the MBSs as well as with the other states in the wire. Fig. 3.8 (b)&(c) show the differential conductance as function of applied bias and dot level energy. The resonances reveal that there is a large splitting energy for the MBSs. However, the line shapes at low energies are symmetric around the dot level energies where the ground state occupation number of the dot changes. This indicates, according to our effective model, that there is only an insignificant or even vanishing coupling to the second MBS.

The hybridization of the dot spin-up state with the MBSs is much smaller than that of the dot's spin-down state. This can be explained with the spin-canting angle of the MBSs. The different hybridizations can therefore also be used to analyze the spin-canting angle [113].

In Fig. 3.8 (d)&(e) the Zeeman field is tuned in such a way that the Majorana splitting energy is close to zero. In the low-energy transport regime ( $|eV| < 0.3$  meV) the resonances are asymmetric around the point where the ground state occupation number changes which indicates the existence of a large non-local coupling. This is consistent with our findings in the previous section for the setup without the QD.

### 3. Signatures of the Majorana spin in the electrical transport ...

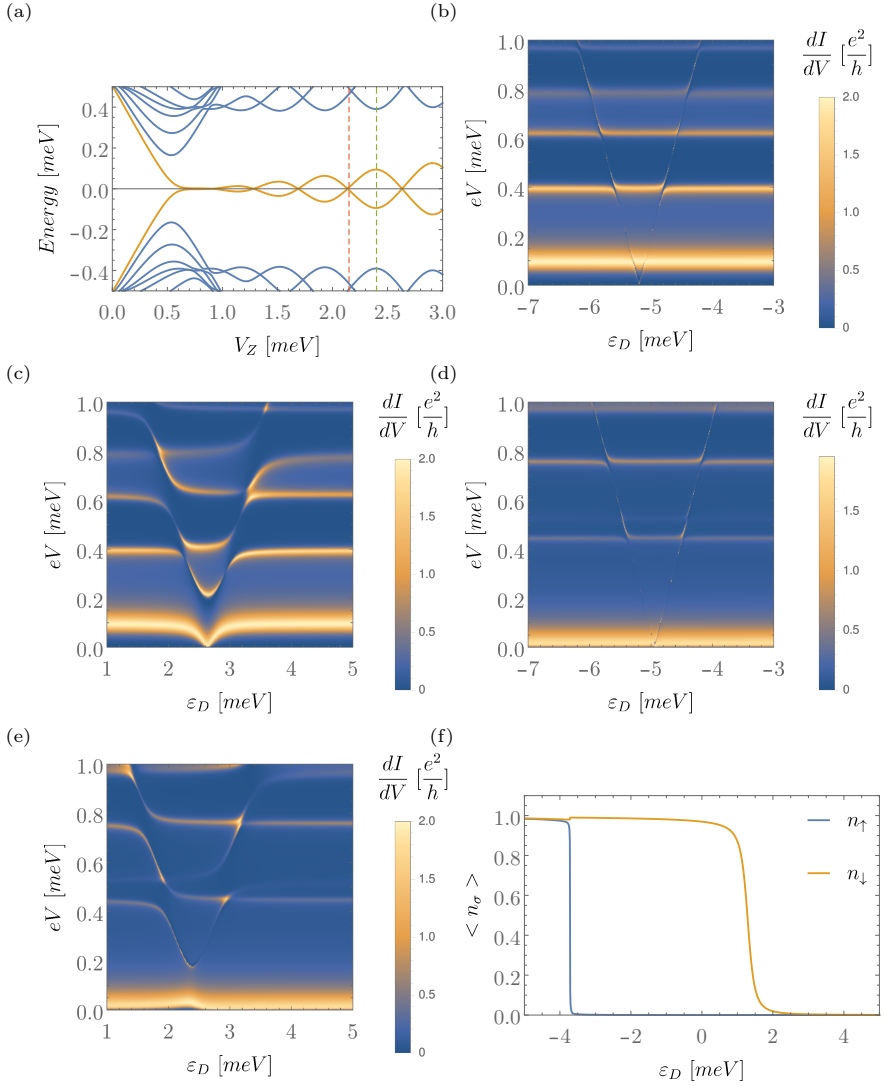


**Figure 3.8.:** (a) Spectrum of a finite-length nanowire - QD setup without an attached lead as a function of applied Zeeman field with  $\varepsilon_D = -10$  meV. The vertical dashed lines indicate the Zeeman fields which were used in the calculations of the differential conductance in (b)-(e). (b)-(e) Differential conductance as a function of applied bias voltage between lead and Majorana nanowire and dot level energy for various Zeeman fields  $V_Z = 2.4$  meV ((b) & (c)) and  $V_Z = 2.15$  meV ((d) & (e)). (f) Occupation number of the QD as a function of dot level energy for  $V_Z = 1.5$  meV. The other microscopic parameters are  $\mu = 0$ ,  $m^* = 0.015m_e$  where  $m_e$  is the electron rest mass,  $\alpha = 20$  meVnm,  $\Delta = 0.5$  meV,  $L = 1$ .  $\mu\text{m}$  and  $U = 3$  meV. Caption and figure taken from Ref. [139]. ©[2020] American Physical Society.

The higher-energy states also hybridize with the QD states. This hybridization is also asymmetric for electron- and hole-like excitations on the dot. It reflects the fact that all excitations can be decomposed into two MBS components, and, in general, these components are not spatially separated and thus the dot couples to both Majorana components of each higher-energy state.

The advantage of this setup compared to the setup without QD is that we can efficiently tune the spectrum of the system which can be probed by electron transport. This leads to qualitative features (symmetric vs. asymmetric hybridization) that allows to discriminate between the case of coupling to only one or both MBSs. In contrast, the differential conductance peak in the setup without quantum dot only changes its height but not its position when we include non-local couplings and its height change might be hard to detect experimentally due to thermal broadening of the conductance resonances.

### 3.4. Conclusion

To sum up, we analyzed the electronic transport in a metallic lead-Majorana nanowire-quantum dot structure. In the topological regime the low-energy physics of the nanowire is described by the two Majorana bound states (MBSs) emerging at both ends of the wire. We allowed for tunnel couplings to both MBSs for lead and dot, respectively and in-

### 3. Signatures of the Majorana spin in the electrical transport . . .

---

cluded the spin structure of the Majorana wave functions in these tunnel couplings. We treat the charging energy of the quantum dot with a mean field approximation. For the low-energy model we use the full counting statistics, a Keldysh based technique, to calculate the cumulant generating function (CGF) which characterizes the full transport between the lead and the topological superconductor. The CGF shows that the only process that contributes to the current is Andreev reflection in two different transport channels which can be associated with the spin in the metallic lead.

If the quantum dot is decoupled from the nanowire, the probability for an Andreev reflection to occur is only depending on the difference of the two Majorana spin-canting angles at the junction. This dependence can be explained with the spin rotation symmetry in the metallic lead. In general, the differential conductance can take on any value between zero and  $4e^2/h$ . In contrast to a setup in which only one MBS is contacted by the lead, the quantization of resonances in the differential conductance is lost. We showed that the differential conductance or the Fano factor at zero bias and temperature can be used to determine the spin-canting angle difference. Furthermore, we showed that the finite temperature behavior of the differential conductance can be used to extract the coupling to the more distant MBS.

The quantum dot introduces more complexity to the system. If the dot levels and the MBS splitting energy are in resonance there is a hybridization between the dot states and the MBSs which leads to bow-tie-like and diamond-like lineshapes of the resonances in the differential conductance as a function of applied bias voltage and dot level energy. At fixed bias voltage Fano resonances emerge as a function of dot level energy. These Fano resonances come in pairs around the points where the occupancy of the dot changes. If the dot and lead couple only to one MBS each pair of Fano resonances is symmetric and quantized to  $2e^2/h$ .

Finally, we used a tight binding model of a full Majorana nanowire to calculate the differential conductance numerically. In the case without quantum dot, the numerical calculation shows that for realistic parameters both MBS can be contacted by the lead. In the case with quantum dot, we treat the mean field approximation self-consistently. By comparing the numerical calculations with the effective model, we find that the non-local couplings are largest when the splitting energy of the MBS is smallest.

## 4. The influence of the Majorana non-locality on the supercurrent

In the two previous chapters, we considered the transport between a metallic lead and a grounded topological superconductor (TSC) and have seen that the transport was governed by Andreev reflection a process that transfers two electrons (or holes) from the lead to the superconductor. However, in this chapter we focus on a setup in that the TSC is not probed by a normal metallic but a superconducting lead. Together lead and TSC form a Josephson junction and a supercurrent can be driven through the junction without a voltage drop [191]. This Josephson effect occurs in all junctions between superconductors that are connected by a weak link. The maximal current that can be driven through the junction without voltage drop is called critical current. Without going into the details here, the equilibrium Josephson current can be calculated by taking the derivative of the free energy (or the ground state energy at zero temperature) with respect to the superconducting phase difference [192]. For a standard Josephson junction consisting of two BCS (Bardeen-Cooper-Schrieffer) superconductor's energy phase relation and therefore the Josephson current is  $2\pi$  periodic. Additionally, an applied bias voltage leads to an evolution of the phase over time following the second Josephson equation [47]. In the case of a rf-driven junction with the bias voltage  $V = V_0 + V_1 \cos(\omega_1 t)$ , Shapiro steps in the dc current occur when  $V_0 = n\hbar\omega_1/2e$  [193].

The Josephson effect in TSC-TSC Josephson junctions that are also called topological Josephson junctions can show a different behavior. In an ideal configuration the supercurrent shows a  $4\pi$ -fractional Josephson effect in that the energy phase relation becomes  $4\pi$  periodic [29, 73, 74]. This doubling of period corresponds to the fractionalization of charge carriers, in

#### 4. The influence of the Majorana non-locality on the ...

---

this case Cooper pairs. This fractionalization is possible because of the zero-energy fermionic degree of freedom of the idealized MBSs. Taking interactions into account even higher fractionalized Josephson effects can occur, e.g.  $8\pi$ . In these cases, the Josephson current is mediated by parafermions, a generalization of Majorana fermions [91].

In any finite size topological Josephson junctions the degeneracy of the fermionic degree of freedom is lifted and in general the  $4\pi$  effect becomes  $2\pi$  periodic again [75, 77, 79]. Also, quasi-particle poisoning events that change the parity of the junction reduce the periodicity back to the  $2\pi$  periodicity. These, in addition to the fact that every real world experiment uses finite size TSCs, make the fractional Josephson effect fragile and not directly measurable in equilibrium experiments. The  $4\pi$  effect can, however, be restored by applying a dc bias voltage which results in a linear time dependence of the superconducting phase difference. If the phase is swept fast enough, Landau-Zener process can induce transitions between the non-degenerate states which recovers the  $4\pi$  periodicity [75, 77–79]. However, Landau-Zener processes can also induce transitions to continuum states which again destroys the  $4\pi$  periodicity.

Another experimentally feasible strategy to unveil the fractional Josephson effect is relying on Shapiro step experiments. Because Shapiro steps are connected to the periodicity of the junction, a  $4\pi$  periodicity leads to the missing of odd Shapiro steps [86–88, 194]. First experiments showed the missing of the first odd Shapiro step [82, 84] and current state of the art experiments showed a suppression of all odd Shapiro steps [83]. Another dynamical measurement of the  $4\pi$  effect is to directly detect the emitted Josephson radiation which also has been observed experimentally [89, 90]. Another tool for the detection of MBSs is to look at the dissipative quasi-particle current in a voltage biased junction. In the TSC-TSC case, multiple Andreev reflection leads to multiple peaks at subgap voltages [77, 195, 196]. In a normal S-TSC setup the subgap transport is suppressed and a universal peak in the differential conductance with  $\frac{dI}{dV} = (4 - \pi)\frac{2e^2}{h}$  arises at  $eV = \pm\Delta_{\text{BCS}}$ , where  $\Delta_{\text{BCS}}$  is the superconducting gap in the normal  $s$ -wave superconducting lead [196–200]. The advantage of the superconducting lead in comparison with a normal conducting lead lies within the exponential suppression of thermal broadening effects due to the density of states in the superconducting lead. First STM experiments that use a superconducting tip in order to probe magnetic

---

adatoms on lead surfaces, show these peaks that however are not quantized to the predicted value [110, 201].

The Josephson current in junctions consisting of normal *s*-wave superconductor and TSCs show a different behavior. In a junction between a pure *s*-wave and a pure *p*-wave equilibrium superconductor the Josephson current is completely blocked [202]. This blockade can however be lifted if the *s*-wave superconductor does not only contact a single, but two MBS [203, 204] if their spin is non-collinear. In junctions between an *s*-wave lead and a Majorana nanowire in the topologically non-trivial phase finite Josephson currents can be found in an *s*-wave Majorana nanowire junction [205–207]. This can be attributed to a residual *s*-wave pairing in the higher-energy states coming from the parent superconductor that proximity induces the superconductivity in the nanowire.

In this chapter we focus on the equilibrium supercurrent in an *s*-wave superconductor - finite size Majorana nanowire Josephson current. In contrast to the previous works considering this kind of Josephson junction we emphasize the finite size of the nanowire and explicitly analyze the contribution to the supercurrent coming from the MBSs emerging at both ends of the Majorana nanowire. We show that a coupling to both MBSs in the nanowire lifts the supercurrent blockade.

In order to calculate the Majorana contribution to the Josephson current, we use the quasi-degenerate perturbation theory to find an effective Hamiltonian for the low-energy sector. As already seen in Chap. 3, the spin-canting angle difference  $\delta\Theta$  of the two MBSs at the position of the junction has influence on the transport properties. We show that the critical current shows a dependence on  $\delta\Theta$ . In order to relate the resulting supercurrent to experimentally relevant parameters, we calculate the Majorana spinor wave function approximately. As a function of applied Zeeman field the critical current is oscillating with an increase in amplitude for larger Zeeman fields. We attribute these oscillations to the rotation of the spin-canting angle of the MBS more distant to the junction. Also, the critical current changes sign at parity crossings. These two effects are the main findings of this chapter.

In addition, we show that higher-energy states can also contribute to the Josephson current, if they experience a residual *s*-wave pairing from the parent superconductor. We verify our findings using a numerical tight-binding calculation for the full system. Here, we find that the high-energy contributions are concealing the Majorana contributions. We also suggest

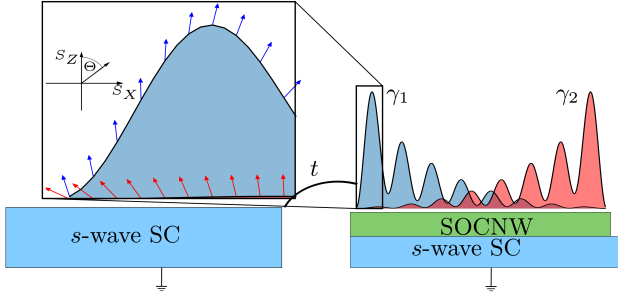


**Figure 4.1.:** Sketch of the considered Josephson junction between an  $s$ -wave superconductor and a topological superconducting nanowire including the calculated wave functions of the two MBS  $\gamma_1$  and  $\gamma_2$ . The wave functions decay into the wire and their spin cantings (arrows) change with position along the wire. Electrons can tunnel between the  $s$ -wave superconducting lead and the nanowire with tunneling amplitude  $t$  creating overlap with both MBS. Figure and caption taken from Ref. [140].  
 ©[2018] American Physical Society.

an experimental scheme to unveil the Majorana contributions by using quasi-particle poisoning.

The rest of this chapter is organized as follows: In Chap. 4.1 we introduce the model under consideration. We derive the low-energy effective model in Chap. 4.2 and discuss the contribution from higher-energy states in Chap. 4.3. To verify our analytical results we present a numerical analysis of the considered model in Chap. 4.4. The results presented in this chapter have been originally published in Ref. [140].

### 4.1. Model

We consider a Josephson junction between a conventional  $s$ -wave superconducting lead and a grounded finite size Majorana nanowire. The  $s$ -wave lead is described with the standard BCS Hamiltonian

$$H_{\text{BCS}} = \sum_{\mathbf{k}} \epsilon_{\mathbf{k}} c_{\mathbf{k}\sigma}^\dagger c_{\mathbf{k}\sigma} + \Delta_{\text{BCS}} \left( e^{i\varphi_1} c_{\mathbf{k}\uparrow}^\dagger c_{-\mathbf{k}\downarrow}^\dagger + e^{-i\varphi_1} c_{-\mathbf{k}\downarrow} c_{\mathbf{k}\uparrow} \right), \quad (4.1)$$



where  $\epsilon_{\mathbf{k}} = \hbar^2 \mathbf{k}^2 / 2m - \mu_{\text{BCS}}$  is the single-particle energy of the lead in the normal phase [47],  $\Delta_{\text{BCS}}$  is the superconducting pairing amplitude,  $\varphi_1$  is the superconducting phase and  $c_{\mathbf{k}\sigma}^\dagger$  creates an electron with momentum  $\hbar \mathbf{k}$  and spin  $\sigma$ . We note that the superconducting phase itself is no measurable entity because of the  $U(1)$  gauge degree of freedom of the electron creation and annihilation operators. With the use of the Bogoliubov-Valatin transformation [208, 209]

$$\begin{aligned} c_{\mathbf{k}\uparrow} &= u_{\mathbf{k}}^* \gamma_{\mathbf{k}0} + v_{\mathbf{k}} \gamma_{\mathbf{k}1}^\dagger \\ c_{-\mathbf{k}\downarrow}^\dagger &= -v_{\mathbf{k}}^* \gamma_{\mathbf{k}0} + u_{\mathbf{k}} \gamma_{\mathbf{k}1}^\dagger, \end{aligned} \quad (4.2)$$

where the coefficients  $u_{\mathbf{k}}$  and  $v_{\mathbf{k}}$  satisfy  $|u_{\mathbf{k}}|^2 + |v_{\mathbf{k}}|^2 = 1$ , the Hamiltonian in Eq. (4.1) is being diagonalized

$$H_{\text{BCS}} = \sum_{\mathbf{k}} E_{\mathbf{k}} (\gamma_{\mathbf{k}0}^\dagger \gamma_{\mathbf{k}0} + \gamma_{\mathbf{k}1}^\dagger \gamma_{\mathbf{k}1}), \quad (4.3)$$

with  $E_{\mathbf{k}} = \sqrt{\epsilon_{\mathbf{k}}^2 + \Delta_{\text{BCS}}^2}$  and  $\gamma_{\mathbf{k}n}^\dagger$  creating a quasi-particle excitation in the superconducting lead. To be precise, we shifted the ground state energy of the Hamiltonian in Eq. (4.3) to zero, because we are only interested in the excitation spectrum.

To describe the Majorana nanowire we resort to a one dimensional effective mass approximation in real space [53, 54]. Within the Bogoliubov-de Gennes (BdG) formalism the Hamiltonian can be written as

$$H_{\text{NW}} = \frac{1}{2} \int_0^L dx \Psi^\dagger(x) \mathcal{H}_{\text{BdG}} \Psi(x), \quad (4.4)$$

where  $L$  is the finite length of the nanowire and  $\Psi^\dagger(x) = [\psi_\uparrow^\dagger(x), \psi_\downarrow^\dagger(x), \psi_\downarrow(x), -\psi_\uparrow(x)]$  is the creation operator in Nambu basis with  $\psi_\sigma^\dagger(x)$  creating an electron at position  $x$  with spin  $\sigma$ . The BdG Hamiltonian  $\mathcal{H}_{\text{BdG}}$  is given by

$$\mathcal{H}_{\text{BdG}} = \left[ \left( -\frac{\hbar^2}{2m^*} \partial_x^2 - \mu \right) - i\alpha \partial_x \sigma_y \right] \tau_z + V_Z \sigma_z + \Delta \tau_x, \quad (4.5)$$

where the Pauli matrices  $\sigma_i$  and  $\tau_i$  act in spin and particle-hole space respectively. Here,  $m^*$  is the effective mass,  $\mu$  is the chemical potential,  $\alpha$  is the Rashba spin orbit parameter,  $V_Z$  is the applied Zeeman field and  $\Delta$  is

#### 4. The influence of the Majorana non-locality on the ...

---

the proximity induced superconducting pairing amplitude in the nanowire. For simplicity, we directly choose a gauge in which the superconducting phase  $\varphi_2$  does not enter the nanowire Hamiltonian. This Hamiltonian can also be diagonalized using a Bogoliubov transformation. However, because of the richer spin dependence, it is necessary to introduce the spinor wave function  $\alpha_{n\sigma}(x)$  and  $\beta_{n\sigma}(x)$  along with the quasi-particle excitation creation operator  $\eta_n^\dagger$

$$\psi_\sigma(x) = \sum_n \alpha_{n\sigma}(x)\eta_n + \beta_{n\sigma}^*(x)\eta_n^\dagger, \quad (4.6)$$

which results in

$$H_{\text{NW}} = \sum_n \varepsilon_n \eta_n^\dagger \eta_n. \quad (4.7)$$

In the topologically non-trivial phase ( $V_Z \gg \sqrt{\mu^2 + \Delta^2}$ ) the low-energy sector of this Hamiltonian is given by a single fermionic level which can be either empty or occupied. This level is of special interest because it can be decomposed in two mostly spatial separate MBS  $\eta_1 = (\gamma_1 + i\gamma_2)/2$  which emerge at the end of the nanowire as its topologically produced boundary modes. Because of the finite size of the nanowire the spinor wave functions of these two MBSs  $\Lambda_{n\sigma}(x)$  overlap which leads to a finite splitting energy  $\varepsilon$  and the low-energy Hamiltonian for the nanowire is given as

$$H_{\text{NWLE}} = i\varepsilon\gamma_1\gamma_2. \quad (4.8)$$

The tunnel Hamiltonian that mediates the transfer of electrons between the lead and the Majorana nanowire is given as

$$H_{\text{T}} = \sum_{\mathbf{k}, \sigma} t e^{i\frac{\varphi}{2}} c_{\mathbf{k}\sigma}^\dagger \psi_\sigma(0),$$

with the momentum and spin independent tunneling amplitude  $t$ . We choose to gauge the superconducting phase difference  $\varphi = \varphi_1 - \varphi_2$  into the tunneling Hamiltonian and note that this difference has a physical meaning. The full Hamiltonian of the system is therefore given by

$$H = H_{\text{BCS}} + H_{\text{NW}} + H_{\text{T}}. \quad (4.9)$$

## 4.2. Low energy effective system

Because we are interested in the contributions of the MBSs to the Josephson current we consider the nanowire to be in the topologically non-trivial regime so that we describe the complete nanowire with  $H_{\text{NWLE}}$ . Moreover, we can rewrite the electron creation and annihilation operators in terms of the MBS operators and their wave functions

$$\psi_{\sigma}(0) \approx \Lambda_{1\sigma}(0)\gamma_1 + \Lambda_{2\sigma}(0)\gamma_2. \quad (4.10)$$

In order to calculate the Josephson current analytically, we use the quasi-degenerate perturbation theory, where we assume the tunneling to be a small perturbation to the unperturbed Hamiltonian  $H_0 = H_{\text{BSC}} + H_{\text{NWLE}}$ . Up to second order in the perturbation the effective low-energy Hamiltonian can be calculated as

$$H = PH_0P + PH_T \frac{Q}{E - H_0} H_T P, \quad (4.11)$$

where  $P$  projects onto the low-energy sector comprised of the ground state of the BCS lead and the two MBS in the nanowire and  $Q = 1 - P$  projects onto the high-energy sector, meaning an excitation in the BCS superconductor. The first order corrections vanish, because a single tunnel event always brings the superconductor from the ground state to an excited state. In the limit  $\varepsilon \ll \Delta_{\text{BCS}}$ , we find for the eigenenergies

$$E_{e(o)}^{(2)} = \mp \varepsilon \pm 2\pi\nu(0) \left( it^2 e^{i\varphi} [\Lambda_{1\uparrow}(0)\Lambda_{2\downarrow}(0) - \Lambda_{1\downarrow}(0)\Lambda_{2\uparrow}(0)] + c.c. \right), \quad (4.12)$$

where the upper sign corresponds to the even parity in the system and the lower sign to the odd parity respectively and  $\nu(0)$  is the density of states at the Fermi level in the lead. The details of the calculations leading to this result can be found in App. C. At this point we want to note two things. First, the Majorana wave functions enter Eq. (4.12) in a singlet projection which reflects the singlet character of the Cooper pairs in the  $s$ -wave lead. Second, if the wave function of the more distant MBS does not reach the junction, i.e.  $\Lambda_{2\sigma}(0) = 0$ , we retrieve the results found in Ref. [202] and the  $\varphi$  dependence drops from the eigenenergies and no Josephson current can flow.

In the next step, we want to connect the effective parameters to the microscopic parameters introduced in the previous section. However, because

#### 4. The influence of the Majorana non-locality on the ...

---

the BdG Hamiltonian is of dimension  $4 \times 4$  and it includes a second order derivative there is no closed analytical solution to its eigenvalue problem and we need to resort to approximations in order to solve it. It is possible to find Majorana wave function solutions of  $H_{\text{BdG}}$  in the case of semi-infinite wires analytically [55, 190]. So we calculate these Majorana wave functions and cut them off at position  $L$  to enforce the finite size of the nanowire. The details of this calculation can be found in App. D. We find that the Majorana spinor wave functions have no spin- $y$  component, so that we can parameterize them as

$$\begin{pmatrix} \Lambda_{n\uparrow}(0) \\ \Lambda_{n\downarrow}(0) \end{pmatrix} = i^{n-1} \kappa_n \begin{pmatrix} \cos(\Theta_n/2) \\ \sin(\Theta_n/2) \end{pmatrix}. \quad (4.13)$$

Here,  $\kappa_2 = \kappa_1 e^{-L/\xi}$ , with  $\xi$  being the Majorana localization length and  $\kappa_1$  being a real valued free parameter. We introduced  $\kappa_1$  as another approximation, because strictly speaking the boundary conditions lead to vanishing wave functions at the ends of the wire. The exponential suppression of  $\kappa_2$  with respect to  $\kappa_1$  is due to the exponential decay of the Majorana wave functions along the nanowire. The spin-canting angles at the position of the junction  $\Theta_n$  can be different, because the spin of the Majorana wave function rotates as the wave function traverses the wire because of spin-orbit interaction. We can now insert this parametrization into Eq. (4.12) to find

$$E_{e(o)}^{(2)} = \pm \varepsilon \mp \Gamma \cos(\varphi) \sin\left(\frac{\Theta_1 - \Theta_2}{2}\right) e^{-L/\xi}, \quad (4.14)$$

where  $\Gamma = 4\pi\kappa_1^2 t^2 \nu(0)$  and we assumed that  $t$  is real valued. A close look at Eq. (4.14) reveals that the  $\varphi$ -dependent contribution to the eigenenergies vanishes if the spins of the two MBSs at the junction point in the same direction. In this case, Cooper pairs cannot be transferred from the lead to the nanowire, because the Cooper pairs in the lead are built up from two electrons with different spin. Moreover, we see only the spin-canting angle difference enter in Eq. (4.14), because the lead is spin rotation invariant and we can always choose a spin basis in the lead in which one spin points along the direction of the spin of the nearest MBS. Also, we see an exponential suppression of the  $\varphi$ -dependent contribution to the eigenenergies with the length of the nanowire, because the more distant MBS becomes less accessible for electrons tunneling through the

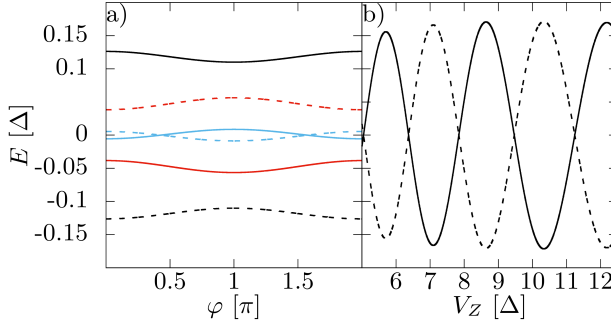


**Figure 4.2.:** a) and b): Effective low-energy spectrum (Eq. (4.14)) as a function of the superconducting phase difference for different applied Zeeman fields (blue:  $V_Z = 5.05\Delta$ , black:  $V_Z = 6.0\Delta$ , red:  $V_Z = 6.5\Delta$ ) (a)) and as a function of the applied Zeeman field for  $\varphi = \pi/2$  (b)). Dashed lines correspond to odd parity states, while full lines correspond to even parity states. The microscopic parameters are  $m^* = 0.015m_e$ ,  $\Delta = 0.2$  meV,  $\mu = 0$ ,  $\alpha = 20$  meV nm,  $\Gamma = 0.004$  meV,  $L = 1.3$   $\mu\text{m}$ . Figure and caption taken from Ref. [140]. ©[2018] American Physical Society.

#### 4. The influence of the Majorana non-locality on the ...

---

junction. In general, because of the particle-hole symmetry the energies of even and odd parity show a zero or  $\pi$ -junction behavior. Depending on the parameters, either the even or odd state can be the ground state of the system. It can also happen that the ground state changes during the evolution of the superconducting phase difference as seen in Fig. 4.2 a). As a function of magnetic field both eigenenergies are oscillating with a rising amplitude for higher Zeeman fields (see Fig. 4.2 b)). This increase in amplitude can be attributed to a larger localization length [76] and thus a bigger spatial overlap of the two MBSs.

The equilibrium Josephson current can be calculated from the ground state energy by taking the derivative with respect to the superconducting phase difference

$$\begin{aligned} I(\varphi) &= \frac{2e}{\hbar} \partial_{\varphi} \min(E_e^{(2)}, E_o^{(2)}) \\ &= I_C(\varphi) \sin(\varphi), \end{aligned} \tag{4.15}$$

where the  $\varphi$  dependency of  $I_C$  only changes its sign, if the two energy levels cross as a function of  $\varphi$ . As shown in Fig. 4.3 a) the critical current oscillates with applied Zeeman field. We can attribute the oscillations to the rotation of the spin-canting angle difference as function of Zeeman field seen in Fig. 4.3 b). It can also be seen that this rotation is nearly completely governed by the more distant MBS, while the closer MBS is spin polarized in the direction of magnetic field. Furthermore, the amplitude of the oscillations is rising with increased applied Zeeman field because of the better accessibility of the second MBS. Also, the critical current jumps at parity crossings as the junction switches between a zero and  $\pi$ -junction or vice versa.

### 4.3. High energy contributions

In the previous section, we focused on the Majorana contributions to the supercurrent, but previous works showed that even in the limit of semi-infinite wires a finite Josephson current can be found [206, 207]. These contributions can only come from higher-energy states of the wire. In order to analyze their contribution in leading order, we calculate the second order corrections to the eigenenergies of the full wire Hamiltonian  $H_{\text{NW}} + H_{\text{BCS}}$  where we again consider  $H_{\text{T}}$  as a perturbation. The phase

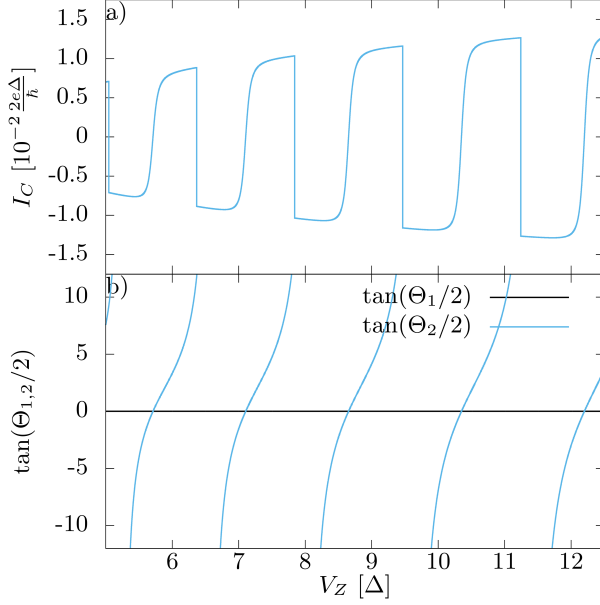


**Figure 4.3.:** a) Critical current ( $I_C(\varphi = \pi/2)$ ) in the ground state of the low-energy model and b) tangent of the spin-canting angles at position  $x = 0$  of the two MBS (1,2) as a function of Zeeman field  $V_Z$ . The other parameters are the same as in Fig. 4.2. The jumps in the supercurrent occur when there is a parity switching of the ground state, while the oscillatory part is due to spin canting rotation of the MBS. When the difference of the spin-canting angles is zero the critical current vanishes. Figure and caption taken from Ref. [140]. ©[2018] American Physical Society.

## 4. The influence of the Majorana non-locality on the ...

---

dependent energy corrections are

$$E_{\varphi}^{(2)} = \sum_n e^{i\varphi} t^2 \left( \alpha_{n\uparrow}(0) \beta_{n\downarrow}^*(0) - \alpha_{n\downarrow}(0) \beta_{n\uparrow}^*(0) \right) f\left(\frac{\varepsilon_n}{\Delta_{BCS}}\right) + c.c., \quad (4.16)$$

where  $f(x) = \nu(0) \int_0^{y_{max}} dy (\sqrt{1+y^2}(\sqrt{1+y^2}+x))^{-1}$  with  $y_{max} = \hbar\omega_D/\Delta_{BCS}$  and with  $\omega_D$  being the Debye frequency. In Eq. (4.16) the function  $f\left(\frac{\varepsilon_n}{\Delta_{BCS}}\right)$  suppresses the contributions of higher energies and because of this suppression it is common to only look out for states at small energies. The wave functions again enter in the form of a spin singlet, because of the singlet Cooper pairs in the BCS lead.

These findings are also consistent with the results of Zazunov and Egger [202] which show that the supercurrent in a Josephson junction between an *s*-wave superconductor and a “pure” *p*-wave superconductor is completely blocked. For a “pure” *p*-wave superconductor the singlet projection of the wavefunction would vanish, i.e.

$$\alpha_{n\uparrow}(0) \beta_{n\downarrow}^*(0) - \alpha_{n\downarrow}(0) \beta_{n\uparrow}^*(0) = 0 \quad \forall n, \quad (4.17)$$

which results in a completely vanishing supercurrent. In general, the analytical calculation of all the wave functions is not possible, therefore we resort to a numerical treatment of the proposed setup in the following section.

### 4.4. Numerical results

In this section, we want to expand our previous analytical analysis of the Josephson junction with numerical results coming from a tight-binding model. We split our analysis in two parts. First, we consider only an isolated finite-size Majorana nanowire to extract some key characteristics, before we calculate the Josephson current numerically using a discretized version of the full Hamiltonian defined in Eq. (4.9).

#### 4.4.1. Finite size Majorana nanowire

As a first step we discretize the full nanowire Hamiltonian in the BdG formalism shown in Eq. (4.4) by replacing the spatial derivative with a difference quotient and the integration with a sum over discrete four component



creation operators in Nambu basis  $\Psi_j^\dagger$ . The discretized Hamiltonian than reads

$$H_{\text{DNW}} = \sum_{j=1}^N \Psi_j^\dagger \left[ \left( \frac{\hbar^2}{m^* a^2} - \mu \right) \tau_z + V_Z \sigma_z + \Delta \tau_x \right] \Psi_j + \Psi_j^\dagger \left[ -\frac{\hbar^2}{2m^* a^2} \tau_z + i \frac{\alpha}{a} \tau_z \sigma_y \right] \Psi_{j-1} + h.c., \quad (4.18)$$

where  $a$  is the spatial spacing  $a = L/N$  with the number of sites  $N$ . Before we focus on the complete Josephson junction we consider the characteristics of the isolated finite size nanowire. We use the python package Kwant [189] to initialize the discretized Hamiltonian from Eq. (4.18) and return it as a sparse matrix. Then we perform a numerically exact diagonalization to calculate the  $4N$  eigenenergies  $E_n$  which we sorted by their value and eigenvectors  $\eta_n$  of the discretized Hamiltonian in matrix form. Because of the particle-hole symmetry, intrinsic to the BdG formalism, the eigenenergies come in pairs  $E_i = -E_{4N-i}$ . The Majorana wave functions can now be extracted from the eigenvectors [210] via  $\gamma_1 = \eta_{2N} + \eta_{2N+1}$  and  $\gamma_2 = i(\eta_{2N} - \eta_{2N+1})$ . The eigenstates  $\eta_{2N}$  and  $\eta_{2N+1}$  are the two eigenstates that have the eigenenergies closest to zero energy.

Using the electronic components of the Majorana wave functions, we can calculate its spin direction which is depicted in Fig. 4.4 a) for the spin at the left end of the wire (the end at which  $\gamma_1$  is mostly localized). The spin shows a qualitative agreement with the effective analytical calculation, because it shows that the spin of the first MBS is nearly constant at high magnetic fields, while the spin of the second MBS rotates as function of Zeeman field. However, the spin rotation of the second MBS shows quantitative deviations which we attribute to the approximation that we just cut off the wave function in order to account for the finite size of the nanowire.

Moreover, we consider the so called Majorana charge [210]

$$Q_M = e \int_0^L dx \sum_{\sigma} u_{\sigma}^1(x) u_{\sigma}^2(x), \quad (4.19)$$

where  $u^{(1,2)}$  are the electron components of the left (1) and right (2) Majorana wave function, respectively. As seen in Fig. 4.4 b), the Majorana

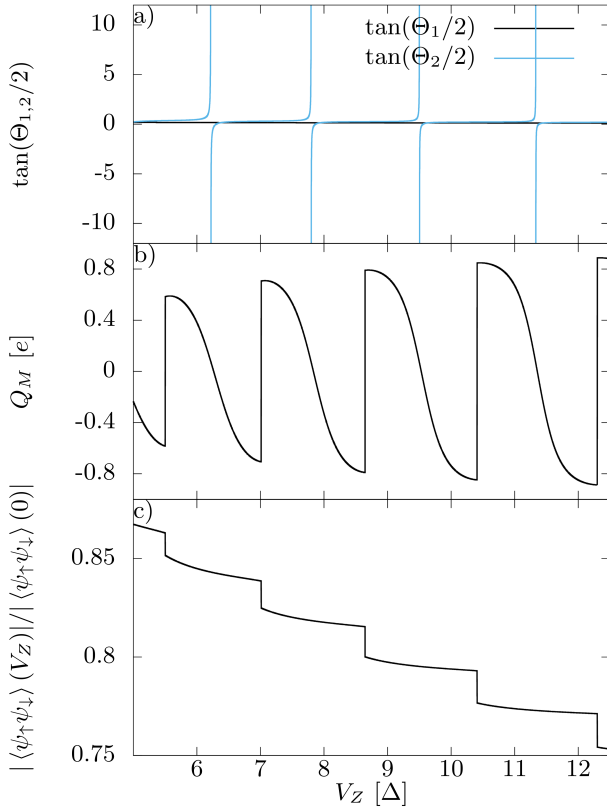


**Figure 4.4.:** a) Tangent of the spin-canting angles, b) Majorana charge and c)  $s$ -wave pairing amplitude at  $x = 0$  as function of Zeeman field for a finite size Majorana wire with length  $L = 1.3 \mu\text{m}$ . The other parameters are as in Fig. 4.2. The spin-canting angle  $\Theta_2$  of the right Majorana shows an oscillatory behavior as a function of the Zeeman field, while  $\Theta_1$  remains nearly constant. The Majorana charge and the  $s$ -wave pairing amplitude exhibit jumps at parity crossings. Figure and caption taken from Ref. [140]. ©[2018] American Physical Society.

charge oscillates as a function of applied Zeeman field. It is maximal at the parity crossings and abruptly changes sign after crossing one of those, which again shows that the crossings seen in the spectrum are indeed parity crossings. The Majorana charge vanishes when the splitting energy is maximal.

Also, we calculate the residual ground state  $s$ -wave pairing in the nanowire

$$|\langle \psi_{\uparrow}(0) \psi_{\downarrow}(0) \rangle| = \left| \sum_n \alpha_{n\uparrow}(0) \beta_{n\downarrow}^*(0) - \alpha_{n\downarrow}(0) \beta_{n\uparrow}^*(0) \right|. \quad (4.20)$$

The pairing amplitude is decreasing with increasing Zeeman field and shows discontinuities at parity crossings (see Fig 4.4 c)). These jumps can be attributed to the contribution of the two overlapping MBSs. It also can be seen that these contributions are smaller than the combined contributions of the higher-energy states.

#### 4.4.2. Josephson current and experimental realization

Now, we introduce the discretized Hamiltonian for the BCS lead with  $M$  sites

$$H_{\text{DBSC}} = \sum_{j=1}^M t_S \sum_{\sigma} c_{j,\sigma}^{\dagger} c_{j-1,\sigma} + \Delta_{\text{BCS}} e^{i\varphi} c_{j,\uparrow} c_{j,\downarrow} + h.c., \quad (4.21)$$

where the hopping parameter  $t_S$  is connected to the bandwidth of the superconductor in the normal state and  $c_{j,\sigma}^{\dagger}$  creates an electron at site  $j$  with spin  $\sigma$ . We also choose to put the chemical potential of the superconductor in the middle of the band. For the tunneling Hamiltonian we consider a point like tunneling from the last site of the BCS lead to the first site of the nanowire with a spin independent tunneling amplitude

$$H_{\text{DT}} = \tilde{t} c_{M,\sigma}^{\dagger} \psi_{1,\sigma} + h.c.. \quad (4.22)$$

In order to calculate the Josephson current we diagonalize the full discretized Hamiltonian  $H_{\text{D}} = H_{\text{DBSC}} + H_{\text{DNW}} + H_{\text{DT}}$  numerically. The ground state Josephson current is then given by

$$I(\varphi) = \frac{2e}{\hbar} \partial_{\varphi} \sum_{E_i < 0} E_i(\varphi), \quad (4.23)$$

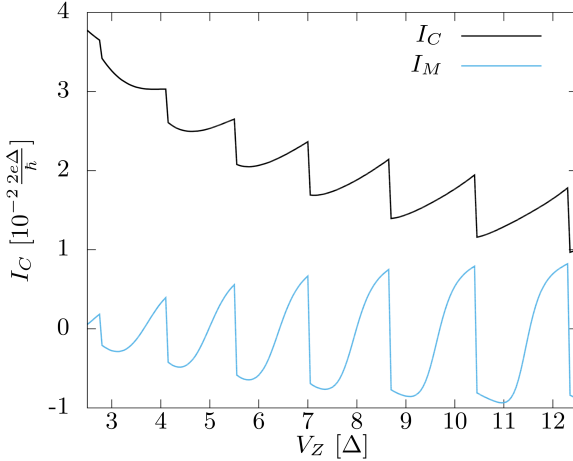


**Figure 4.5.:** Numerically calculated ground state critical current  $I_C$  (black) and Majorana contribution to the critical current  $I_M$  (blue) extracted following the scheme proposed in the main text. Jumps in the critical current occur at parity crossings in the spectrum. The used parameters are  $t_S = 10\Delta$ ,  $\tilde{t} = 2.96$  meV and  $\Delta_{BCS} = \Delta$ . The other parameters are the same as in Fig. 4.2. Figure and caption taken from Ref. [140]. ©[2018] American Physical Society.

and the critical current  $I_C$  is given as

$$I_C = \max_{\varphi} I(\varphi). \quad (4.24)$$

In Fig. 4.5, we show the critical current as function of applied Zeeman. First, we notice that the critical current from the full numerical model and the effective critical current shown in Fig 4.3 have in common that there are discontinuities at parity crossings and an oscillating behavior in between them which we showed to be connected to an oscillation of the Majorana spin-canting angle difference in the low-energy analytical model. However, in contrast to the low-energy model we find that the critical current does not vanish during these oscillations regardless of the spin-canting angle differences and in general is decreasing with increasing

Zeeman field. We attribute these difference between our numerical results and the analytical effective low-energy calculations to the neglected higher energy contributions, because the contributions of the lowest energy level (see Fig 4.3 (blue line)) show a qualitative agreement with the effective model calculations.

As shown in Sec 4.3, the high-energy contributions are suppressed with increasing energy by the factor  $f(\frac{\epsilon_n}{\Delta_{BCS}})$  in Eq. (4.16), yet they conceal the contributions of the MBSs. This is because the Majorana contributions are exponentially suppressed with the length of the wire, because of their wave function localization. However, for a certain set of parameters (very short wires, small BCS gap parameter) it is possible that the low-energy contributions surpass the higher energy contributions. But, in this parameter regime the effective model loses its validity.

Now, the question how to access these Majorana contributions experimentally remains, as they are shadowed by the high-energy contributions in a realistic parameter regime. We propose the following route to extract the Majorana contributions experimentally. First, we propose to measure the critical current  $I_C$  for a fixed set of parameters  $\Delta_Z$ . Within the quasiparticle poisoning time  $T_P \approx 100\mu\text{s}$  [211] the parity of the junction changes which results in a different sign for the Majorana contributions but leaves the higher energy contributions unchanged. Now, the critical current is measured for a second time. The difference between the two critical currents for the two different parities reveals then twice the Majorana contribution  $I_M$ . The suggested experiment is feasible as currents with a sensitivity of  $10^{-2}e\hbar/\Delta$  can be measured on a time scale of  $10\mu\text{s}$ <sup>1</sup>.

## 4.5. Conclusion

In conclusion, we calculated the equilibrium Josephson current in a Josephson junction built from a superconducting *s*-wave lead and a finite sized Majorana nanowire. We set our focus on the influence of the MBS more distant to the junction on the supercurrent.

In an analytical effective low-energy calculation, we showed that the supercurrent is only carried by the MBSs if both of them can be addressed by electron tunneling. Because the Cooper pairs in the lead are spin singlets,

---

<sup>1</sup>Private communication with Cristian Urbina.

#### 4. The influence of the Majorana non-locality on the ...

---

the Majorana wave functions enter the eigenenergies in singlet form. As a function of applied Zeeman field the critical current is oscillating with increasing amplitude for higher Zeeman fields. We can attribute the oscillations to the spin-canting angle difference of the two MBSs, because the spin of the second MBS is rotating as a function of Zeeman field. The increase in amplitude can be explained with a larger Majorana localization length. Also, the critical current changes sign, whenever the parity of the ground state is changed.

Furthermore, we showed that contributions from higher-energy states also enter in spin singlet form. These contributions are suppressed for higher energies. In general, the wave functions of the higher-energy states can have a finite singlet projection, because of the residual *s*-wave pairing from the parent superconductor used to proximity induce the superconductivity in the nanowire.

Moreover, we contrasted our analytical findings with a numerical analysis of the full model. Here, we showed that the high energy contributions conceal the Majorana contributions. Also, we suggest to use quasiparticle poisoning to experimentally extract the Majorana contributions to the Josephson current.

## 5. Summary and Conclusion

This thesis is based on the transport signatures of Majorana bound states (MBSs) that emerge as topological boundary states of *finite size* one dimensional topological superconductors. Special focus was laid on the finite size effects that arise when a lead is tunnel coupled to both MBSs. All in all, three different setups have been considered.

First, we considered a spinless model consisting of a Kitaev chain tunnel coupled to a metallic lead on one side and to a single energy level quantum dot on the other side. To calculate the transport properties we used full counting statistics and found that the only process that contributes to transport are Andreev reflections. In the low-energy regime where we approximated the Kitaev chain by just considering the two MBSs emerging in the topologically non-trivial phase, we could show that pairs of Fano resonances arise in the differential conductance. In the case when the dot and the lead couple to a single MBS each we can describe the differential conductance using the Fano-Beutler formula and show analytically that the particle-hole symmetric property of an isolated MBS is transferred to a mirror symmetry between the two Fano resonances. Moreover, the two Fano resonances are quantized to  $2e^2/h$ . The finite size of the Kitaev chain allows for couplings between the dot and lead and both MBSs, respectively. In general this coupling to both MBSs destroys the symmetry of the two Fano resonances. Also, the resonances are no longer quantized and for equal couplings to both MBSs the transport is completely blocked. To extend the effective low-energy model we considered a full Kitaev chain instead of just the two MBSs. For a chain that is longer than the Majorana localization length, we observed two mirror symmetric Fano resonances. However, if we included extended tunnel couplings to the lead and the dot that allowed us to access both MBS wave functions, we saw the emergence of an asymmetry between the two Fano resonances which is in accordance with the low-energy model.

Second, we considered a spinful model, where we considered a metallic lead coupled to a Majorana nanowire with a quantum dot coupled to the

## 5. Summary and Conclusion

---

other end of the nanowire. Again, we started with a low-energy analysis and allowed for a tunnel coupling to both MBSs, respectively. We calculated the cumulant generating function in order to obtain the transport properties. Like in the previous setup we found that only Andreev reflections contribute to the transport, however due to the spin in the lead they can occur in two different channels. We first focused on a case in which the quantum dot was decoupled from the nanowire. We found that the Andreev reflection probabilities then only depend on the difference of the Majorana spin-canting angles of each MBS at the junction with the lead. We found that depending on the spin-canting angle the differential conductance peaks are not quantized when both MBSs can be accessed by the lead and can take on any value between 0 and  $4e^2/h$ . We showed that in order to differentiate the case of coupling to a single MBS or to both MBSs experiments need to be performed at very low temperatures. The inclusion of the quantum dot leads to a hybridization between the Majorana states and the spinful states on the dot, that heavily depends on the spin-canting angle of the MBS. The differential conductance probes this hybridization, as the resonances correspond to the spectrum of the system without the dot. Finally, we considered a full Majorana nanowire by using a numerical scattering matrix formalism. We have seen that our effective model describes the differential conductance at low bias voltage very well. Without the quantum dot the differential conductance at zero bias voltage showed resonances as a function of applied dot level energy whenever the MBSs are at zero energy. However, these resonance peaks were not quantized which we can attribute to the finite size of the wire and the coupling to the second MBS. The inclusion of the quantum dot showed that the asymmetry within a pair of Fano resonances emerges whenever the Majorana splitting energy is small and vanishes whenever the splitting energy is maximal. This we attributed to the absence of non-local tunnel couplings at high splitting energy.

Lastly, we investigated a Josephson junction consisting of an *s*-wave superconducting lead and a finite size Majorana nanowire. We started our considerations with an effective low-energy Hamiltonian, that we obtained using quasi-degenerate perturbation theory. In this low-energy approach we found that the MBSs only contribute to the equilibrium Josephson current if both of them are tunnel coupled to the lead. Furthermore, we showed that the supercurrent is proportional to the sine of half of the spin-canting angle difference of the two Majorana wave functions at the



---

end of the wire. We approximately calculated the Majorana wave functions to relate the coupling strength to the more distant Majorana and the spin-canting angles to the microscopic parameters of the Majorana nanowire. We showed that as a function of applied Zeeman field the critical current shows three distinct features. First, it is oscillating and these oscillations can be traced back to the rotation of the spin-canting angles. We also found that the spin-canting angle of the more distant MBS is rotating stronger than the spin of the closer MBS. Second, the sign of the critical current changes at parity crossings. And third, the amplitude of the oscillations in the critical current is rising with increased Zeeman field, because the localization length of the MBSs is increased by the larger Zeeman field. In addition to the low-energy contribution, we also looked at the contributions coming from higher-energy states. We have seen that the wave functions of the higher-energy states in the nanowire enter the critical current in a singlet projection because of the  $s$ -wave pairing in the lead. We also performed a numerical tight-binding analysis that included the full nanowire. Here, we found that contributions from the higher-energy states shadow the Majorana contributions. To unveil the Majorana contributions we suggested an experimental scheme involving quasi-particle poisoning.

All of the proposals in this thesis focus on the electrical transport signatures of MBSs. For all three setups we considered what happens to the transport signals when not only one but both MBSs are accessible at the same end of the topological superconductor. Some recent experimental data can be explained by the inclusion of these non-local tunnel couplings. However, more detailed investigations with regards to these finite size effects need to be performed, because a coupling to the second MBS can introduce unwanted errors in topological quantum computation schemes.



# A. Derivation of the Levitov-Lesovik formula

Here, we outline the derivation of the cumulant generating function (CGF) for a system of coupled MBSs including the spin degree of freedom of the charge carriers along the lines of Ref. [116]. For simplicity we perform the calculations using natural units ( $\hbar = e = 1$ ), however the SI units can be restored by dimensional analysis.

The moment generating function is defined as

$$\chi(\lambda) = \langle e^{i\lambda Q} \rangle, \quad (\text{A.1})$$

where the counting field  $\lambda$  is coupled to the transferred charge  $Q = \int_0^{\mathcal{T}} dt I(t)$ . We introduce the auxiliary Hamiltonian

$$H' = H - \frac{1}{2}\lambda(t)I, \quad (\text{A.2})$$

with

$$\lambda(t) = \begin{cases} \lambda & t \in [0, \mathcal{T}] \quad \& \quad t \in \mathcal{C}_- \\ -\lambda & t \in [\mathcal{T}, 0] \quad \& \quad t \in \mathcal{C}_+ , \\ 0 & \text{else} \end{cases} \quad (\text{A.3})$$

where  $\mathcal{C}_{\mp}$  is the forward (backward) part of the Keldysh contour and  $\mathcal{T}$  is the time during which the measurement is performed. With this auxiliary Hamiltonian we can rewrite

$$\begin{aligned} \chi(\lambda) &= \langle T_C \exp \left( -i \int_{\mathcal{C}} dt H'(t) \right) \rangle \\ &= \langle T_C \left( 1 - i \int_{\mathcal{C}} dt [H - (\lambda(t)/2)I] + (\dots) \right) \rangle \\ &= \langle 1 + i\lambda \int_0^{\mathcal{T}} dt I + (\dots) \rangle = \langle e^{i\lambda Q} \rangle. \end{aligned} \quad (\text{A.4})$$

## A. Derivation of the Levitov-Lesovik formula

---

Also, the current operator is the total derivative of the number operator in the lead with respect to time

$$\begin{aligned}
 I &= -\frac{d}{dt}N = -\frac{d}{dt} \int dx \sum_{\sigma} c_{\sigma}^{\dagger}(x) c_{\sigma}(x) \\
 &= i \left[ H, \int dx \sum_{\sigma} c_{\sigma}^{\dagger}(x) c_{\sigma}(x) \right] \\
 &= i \left[ H_T, \int dx \sum_{\sigma} c_{\sigma}^{\dagger}(x) \psi_{\sigma}(x) \right] \\
 &= \sum_{n,\sigma} \gamma_n (t_{L\sigma n} c_{\sigma}^{\dagger}(0) - t_{L\sigma n}^* c_{\sigma}(0)).
 \end{aligned} \tag{A.5}$$

Next we consider the time-dependent unitary transformation  $U_{\lambda} = e^{i\frac{\lambda(t)}{2}N}$  and apply it to  $H$

$$H \rightarrow H_{\lambda} = U_{\lambda} H U_{\lambda}^{\dagger} - i U_{\lambda} \dot{U}_{\lambda}^{\dagger}. \tag{A.6}$$

This leads to

$$H'_{\lambda} = H_{\lambda} - \frac{1}{2} \lambda(t) I = U_{\lambda} H U_{\lambda}^{\dagger}. \tag{A.7}$$

For the calculation of  $U_{\lambda} H_T U_{\lambda}^{\dagger}$  we first point out that  $U_{\lambda}$  commutes with all Majorana operators, so all we need to consider is

$$\begin{aligned}
 U_{\lambda} c_{\sigma}(x) U_{\lambda}^{\dagger} &= e^{i\lambda(t)N/2} c_{\sigma}(x) e^{-i\lambda(t)N/2} \\
 &= c_{\sigma}(x) + \frac{i\lambda(t)}{2} [N, c_{\sigma}(x)] + (\dots) \\
 &= c_{\sigma}(x) - \frac{i\lambda(t)}{2} c_{\sigma}(x) + (\dots)
 \end{aligned} \tag{A.8}$$

Therefore, we find

$$\begin{aligned}
 H'_{\lambda} &= H_L + H'_M + \sum_{n,\sigma} t_{Ln\sigma} e^{i\lambda(t)/2} c_{\sigma}^{\dagger}(0) \gamma_n + t_{Ln\sigma}^* e^{-i\lambda(t)/2} \gamma_n c_{\sigma}(0) \\
 &= H_L + H'_M + H_T^{\lambda},
 \end{aligned} \tag{A.9}$$

where  $H'_M$  is defined in Eq. (3.13) and  $t_{Ln\sigma}$  is defined for  $n = 1, 2$  in Eq. (3.9) and  $t_{Ln\sigma} = 0$  for  $n > 2$ . So we find

$$\chi(\lambda) = \langle T_C \exp \left( -i \int_{\mathcal{C}} ds H_L + H_M + H_T^{\lambda} \right) \rangle. \tag{A.10}$$

We can formulate this moment generating function in the continuum notation as a functional integral. It is important to have in mind that Majorana fermions are described by real field operators and therefore we introduce real Grassmann variables  $\hat{\gamma}$  in order to calculate the functional integral, while we need two mutually independent complex Grassmann variables  $\hat{c}$  and  $\hat{\bar{c}}$  for the electrons in the lead.

The functional integral to calculate the moment generating function is then given as

$$\chi(\lambda) = \int \mathcal{D}[\hat{\gamma}, \hat{c}, \hat{\bar{c}}] e^{iS^\lambda[\hat{\gamma}, \hat{c}, \hat{\bar{c}}]}, \quad (\text{A.11})$$

where  $S^\lambda[\hat{\gamma}, \hat{c}, \hat{\bar{c}}] = S_M[\hat{\gamma}] + S_T^\lambda[\hat{\gamma}, \hat{c}, \hat{\bar{c}}] + S_L[\hat{c}, \hat{\bar{c}}]$  is the Keldysh action, containing the action for the Majorana fermions, the action of the lead and the action describing the tunneling from the lead to the system of Majorana bound states.

These parts are given as

$$\begin{aligned} S_M[\hat{\gamma}] &= \sum_{\alpha\beta} \int_C \int_C ds ds' \hat{\gamma}_\alpha(s) [D^{(0)}(s, s')]^{-1}_{\alpha\beta} \hat{\gamma}_\beta(s') \\ S_T^\lambda[\hat{\gamma}, \hat{c}, \hat{\bar{c}}] &= \sum_{\alpha\sigma} \int_C ds \left[ t_{L\alpha\sigma} e^{\frac{i\lambda(s)}{2}} \hat{\bar{c}}_\sigma(0, s) \hat{\gamma}_\alpha(s) + t_{L\alpha\sigma}^* e^{-\frac{i\lambda(s)}{2}} \hat{\gamma}_\alpha(s) \hat{c}_\sigma(0, s) \right] \\ S_L[\hat{c}, \hat{\bar{c}}] &= \sum_\sigma \int_C \int_C ds ds' \hat{\bar{c}}_\sigma(0, s) [G_\sigma(s, s')]^{-1} \hat{c}_\sigma(0, s'), \end{aligned} \quad (\text{A.12})$$

where,  $D^{(0)}(s, s')$  is the unperturbed Green's function for the Majorana bound states and  $G_\sigma(s, s') = G_\sigma(x' = 0, x = 0, s', s) = -i \langle T_C \hat{c}_\sigma(0, s') \hat{\bar{c}}_\sigma(0, s) \rangle$  is the boundary Green's function for the lead with spin  $\sigma$ . The position integral for  $x \neq 0$  for the lead has already been performed and is neglected because the path integral is normalized in such a way that  $\chi(0) = 1$ . Now the moment generating function only contains Gaussian integrals. We can integrate over the lead degrees of freedom to find

$$\chi(\lambda) = \int \mathcal{D}[\hat{\gamma}] \exp \left( i \sum_{\alpha\beta} \int_C \int_C ds ds' \hat{\gamma}_\alpha(s) [D^\lambda(s, s')]^{-1}_{\alpha\beta} \hat{\gamma}_\beta(s') \right), \quad (\text{A.13})$$

where  $[D^\lambda(s, s')]^{-1} = [D^{(0)}(s, s')]^{-1} - \Sigma^\lambda(s, s')$ , with the counting field

## A. Derivation of the Levitov-Lesovik formula

---

dependent self energy

$$\begin{aligned} \Sigma_{\alpha\beta}^{\lambda}(s, s') = \sum_{\sigma} \left[ -t_{L\alpha\sigma} t_{L\beta\sigma}^* e^{-i\frac{\lambda(s)-\lambda(s')}{2}} G_{\sigma}(s, s') \right. \\ \left. + t_{L\beta\sigma} t_{L\alpha\sigma}^* e^{i\frac{\lambda(s)-\lambda(s')}{2}} G_{\sigma}(s', s) \right]. \end{aligned} \quad (\text{A.14})$$

To evaluate the Gaussian integral for real valued Grassmann fields we follow Ref. [212] and consider

$$J = \int D[a] \exp \left( - \sum_{ij} a_i M_{ij} a_j \right), \quad (\text{A.15})$$

where  $\{a_i\}$  is a set of real valued Grassmann variables and  $M_{ij}$  are the elements of a skew symmetric matrix  $M$ . To evaluate  $J$  we first square it

$$J^2 = \int D[a, b] \exp \left( - \sum_{ij} a_i M_{ij} a_j - b_i M_{ij} b_j \right), \quad (\text{A.16})$$

where  $\{b_i\}$  is also a set of real valued Grassmann variables. We can now define complex Grassmann variables  $\eta_i = \frac{1}{2}(a_i + ib_i)$  and find

$$J^2 = J_G \int D[\eta, \bar{\eta}] \exp \left( - \sum_{ij} \bar{\eta}_j M_{ij} \eta_j \right), \quad (\text{A.17})$$

with  $J_G$  being the Jacobian of the above transformation. Now, we can use the Gaussian integral for Grassmann variables

$$J^2 = J_G \det M, \quad (\text{A.18})$$

and therefore

$$J = \sqrt{J_G} \sqrt{\det M}. \quad (\text{A.19})$$

Because  $[D^{\lambda}(s, s')]_{\alpha\beta}^{-1} = -[D^{\lambda}(s', s)]_{\beta\alpha}^{-1}$  we can apply this to Eq. A.13 which leads to

$$\chi(\lambda) = \frac{\sqrt{\det ([D^{\lambda}]^{-1})}}{\sqrt{\det ([D^{\lambda=0}]^{-1})}}, \quad (\text{A.20})$$

---

where we enforced the normalization by division with  $\sqrt{\det ([D^{\lambda=0}]^{-1})}$ . The determinant has to be calculated with respect to time, Majorana and Keldysh indices. During the long measuring time  $\mathcal{T}$  the counting fields are constant and a Fourier transform diagonalizes the Keldysh Green's function in energy space, so that the determinant with respect to the energy space is just a product and therefore the cumulant generating function, the logarithm of  $\chi$ , is given by

$$\ln \chi(\lambda) = \frac{1}{2} \sum_{\omega} \ln \left[ \frac{\det ([D^{\lambda}]^{-1}(\omega))}{\det ([D^{\lambda=0}]^{-1}(\omega))} \right]. \quad (\text{A.21})$$

Now the determinant has to be taken with respect to Keldysh and Majorana indices. The summation can be transformed into an integration, because the frequencies will be quantized due to the long measuring time which results in the Levitov-Lesovik formula [116, 167, 187]

$$\ln \chi(\lambda) = \frac{\mathcal{T}}{2} \int \frac{d\omega}{2\pi} \ln \left[ \frac{\det ([D^{\lambda}]^{-1}(\omega))}{\det ([D^{\lambda=0}]^{-1}(\omega))} \right]. \quad (\text{A.22})$$





## B. Calculation of the unperturbed Majorana Green's function

In this section we want to describe the calculation of the Majorana Green's function in detail. We start with the Heisenberg equation of motion (EOM) for the Majorana operators with the unperturbed Hamiltonian  $H'_M$  (see Eq. (3.13))

$$\frac{d}{dt}\gamma_\alpha = i[H'_M, \gamma_\alpha] = 2 \sum_\beta A_{\alpha\beta} \gamma_\beta, \quad (\text{B.1})$$

where we used the skew symmetric property  $A_{\alpha\beta} = -A_{\beta\alpha}$ . The solutions to this EOM are

$$\gamma_\alpha(t) = \sum_\beta \mathcal{B}_{\alpha\beta}(t) \gamma_\beta(0), \quad (\text{B.2})$$

with  $\mathcal{B}(t) = \exp(2At)$ . The time dependent unperturbed Majorana Green's function then is

$$D_{\alpha\beta}^{(0)}(t) = -i \langle T_C \gamma_\alpha(t) \gamma_\beta(0) \rangle \quad (\text{B.3})$$

$$\begin{aligned} &= -i \mathcal{B}_{\alpha\beta}(t) (\Theta_C(t) - \Theta_C(-t)) - i \sum_{\nu \neq \beta} \mathcal{B}_{\alpha\nu}(t) e_{\nu\beta} \\ &= -i \mathcal{B}_{\alpha\beta}(t) \begin{pmatrix} \text{sign}(t) & -1 \\ 1 & -\text{sign}(t) \end{pmatrix} \\ &\quad - i \sum_{\nu \neq \beta} \mathcal{B}_{\alpha\nu}(t) e_{\nu\beta} \begin{pmatrix} 1 & 1 \\ 1 & 1 \end{pmatrix}, \end{aligned} \quad (\text{B.4})$$

where  $\Theta_C(t)$  is the Heaviside function on the Keldysh contour and we defined  $e_{\nu\beta} = \langle \gamma_\nu \gamma_\beta \rangle$ . Here, the Keldysh indices are organized as

## B. Calculation of the unperturbed Majorana Green's function

$[(-, -)(+, +)]^T$ . In order to calculate the Fourier transform of  $D_{\alpha\beta}^{(0)}(t)$  we need to consider the Fourier transforms of  $\mathcal{B}(t)$  and  $\mathcal{B}(t)\text{sign}(t)$ . First, we note that we can diagonalize the Hermitian matrix  $-iA = UD_AU^\dagger$  where  $D_A = \text{diag}(\lambda_k)$  with the eigenvalues  $\lambda_k$  where for every positive  $\lambda_k$  there is a  $\lambda_{\bar{k}} = -\lambda_k$  which in our case leads to six  $\lambda_k$  and find

$$\begin{aligned} \int dt e^{i\omega t} \mathcal{B}(t) &= U \int dt e^{i\omega t} e^{iD_A t} U^\dagger \\ &= U \text{diag } 2\pi\delta(\omega - \lambda_k) U^\dagger. \end{aligned} \quad (\text{B.5})$$

In order to calculate the second Fourier integral we find it convenient to use the following change of basis  $2A = QSQ^T$  with

$$S = \begin{pmatrix} 0 & \lambda_1 & 0 & 0 & 0 & 0 \\ -\lambda_1 & 0 & 0 & 0 & 0 & 0 \\ 0 & 0 & 0 & \lambda_2 & 0 & 0 \\ 0 & 0 & -\lambda_2 & 0 & 0 & 0 \\ 0 & 0 & 0 & 0 & 0 & \lambda_3 \\ 0 & 0 & 0 & 0 & -\lambda_3 & 0 \end{pmatrix}, \quad (\text{B.6})$$

which is possible because  $A$  is skew symmetric. Using this we find

$$\begin{aligned} -i \int dt e^{i\omega t} \text{sign}(t) \mathcal{B}(t) &= Q \int dt e^{i\omega t} e^{St} Q^T \\ &= -iQ \int dt \text{sign}(t) e^{i\omega t} \text{diag} \begin{pmatrix} \cos \lambda_k t & \sin \lambda_k t \\ -\sin \lambda_k t & \cos \lambda_k t \end{pmatrix} Q^T \\ &= Q \text{diag} \begin{pmatrix} \frac{2\omega}{\omega^2 - \lambda_k^2} & \frac{-2i\lambda_k}{\omega^2 - \lambda_k^2} \\ \frac{2i\lambda_k}{\omega^2 - \lambda_k^2} & \frac{2\omega}{\omega^2 - \lambda_k^2} \end{pmatrix} Q^T. \end{aligned} \quad (\text{B.7})$$

For  $\omega \neq \lambda_k$  the off diagonal blocks and all terms containing  $e_{\nu\beta}$  in Eq. (B.4) vanish so that  $D_{\alpha\beta}^{(0)}(\omega)$  is block diagonal. For  $\omega = \lambda_k$  the Dirac distribution in Eq. (B.5) as well as the terms in Eq. (B.7) diverge so that the inverse of the corresponding  $\lambda_k$ -block of the Green's function vanishes. It would vanish even if we would neglect the terms coming from Eq. (B.5). So we only need to consider the block diagonal part of  $D_{\alpha\beta}^{(0)}(\omega)$  for its inverse and find

$$[D^{(0)}]^{-1} = \begin{pmatrix} [D^{(0)}]^{-1} & 0 \\ 0 & -[D^{(0)}]^{-1} \end{pmatrix}, \quad (\text{B.8})$$

---

with

$$\begin{aligned}
[D^{(0)---}]^{-1} &= Q \text{diag} \left( \begin{array}{cc} \frac{\omega}{2} & \frac{i\lambda_k}{2} \\ -\frac{i\lambda_k}{2} & \frac{\omega}{2} \end{array} \right) Q^T \\
&= iA + \frac{\omega}{2}I.
\end{aligned} \tag{B.9}$$

Following Ref. [213] the lead boundary Green's function  $G_\sigma(t', t) = G_\sigma(x' = 0, x = 0, t', t) = -i \langle T_C c_\sigma(x' = 0, t') c_\sigma^\dagger(x = 0, t) \rangle$  for spin  $\sigma$  can be written in the Keldysh-rotated basis in matrix form as

$$iG_\sigma(t', t) = \pi\nu(0) \begin{pmatrix} \delta(t - t') & 2F_\sigma(t - t') \\ 0 & -\delta(t - t') \end{pmatrix}, \tag{B.10}$$

where  $\nu(0)$  is the density of states per spin at the Fermi level in the lead and the Fourier transform of the distribution matrix is  $F_\sigma(\omega) = 1 - 2n_\sigma(\omega)$  with the Fermi distribution function  $n_\sigma(\omega) = (1 + e^{\omega/k_B T})^{-1}$ .

After a back rotation and Fourier transform we find

$$G_\sigma(\omega) = i2\pi\nu(0) \begin{pmatrix} n_\sigma(\omega) - \frac{1}{2} & n_\sigma(\omega) \\ n_\sigma(\omega) - 1 & n_\sigma(\omega) - \frac{1}{2} \end{pmatrix}. \tag{B.11}$$



## C. Quasi-degenerate perturbation theory

To start our calculations we use a effective Hamiltonian to describe the Majorana bound states

$$H_M = -i\varepsilon\gamma_1\gamma_2 = 2\varepsilon(\eta_1^\dagger\eta_1 - \frac{1}{2}), \quad (\text{C.1})$$

where the non-local Fermion operator  $\eta_1$  can be extracted from

$$\begin{aligned} \gamma_1 &= \eta_1 + \eta_1^\dagger \\ \gamma_2 &= i(\eta_1^\dagger - \eta_1). \end{aligned} \quad (\text{C.2})$$

The corresponding eigenstates and eigenenergies are

$$\begin{aligned} |0\rangle \quad E_0 &= -\varepsilon \\ |1\rangle &= \eta_1^\dagger |0\rangle \quad E_1 = \varepsilon. \end{aligned} \quad (\text{C.3})$$

The BCS-Hamiltonian can be written in Terms of Bogoliubov operators

$$H_{\text{BCS}} = \sum_{k,\sigma} E_k \gamma_{k,\sigma}^\dagger \gamma_{k,\sigma}, \quad (\text{C.4})$$

with  $E_k = \sqrt{\xi_k^2 + |\Delta_{\text{BCS}}|^2}$  and where the Bogoliubov operators can be obtained by a Bogoliubov transformation

$$\begin{aligned} c_{k\uparrow} &= u_k^* \gamma_{k0} + v_k \gamma_{k1}^\dagger \\ c_{-k\downarrow}^\dagger &= -v_k^* \gamma_{k0} + u_k \gamma_{k1}^\dagger. \end{aligned} \quad (\text{C.5})$$

### C. Quasi-degenerate perturbation theory

---

The tunneling process between BCS-lead and Majorana bound states can now be described with

$$\begin{aligned} H_T &= \sum_{k,\sigma} [t\Lambda_{1\sigma}^*(0)\gamma_1 + t\Lambda_{2\sigma}^*(0)\gamma_2]c_{k,\sigma} + h.c. \\ &= \sum_{k,\sigma} t_{+\sigma}\eta_1^\dagger\gamma_{k\sigma} + t_{-\sigma}\eta_1\gamma_{k\sigma} + h.c.. \end{aligned} \quad (C.6)$$

In this effective description  $\Lambda(x)_{n\sigma}$  corresponds to the Spinor component of MBS  $n$  at position  $x$  with spin  $\sigma$ . In Eq. (C.6) we use

$$\begin{aligned} t_{-0} &= (t\Lambda_{1\uparrow}^*(0)u_k^* - t^*\Lambda_{1\downarrow}(0)v_k^*) - i(t\Lambda_{2\uparrow}^*(0)u_k^* - t^*\Lambda_{2\downarrow}(0)v_k^*) \\ t_{+0} &= (t\Lambda_{1\uparrow}^*(0)u_k^* - t^*\Lambda_{1\downarrow}(0)v_k^*) + i(t\Lambda_{2\uparrow}^*(0)u_k^* - t^*\Lambda_{2\downarrow}(0)v_k^*) \\ t_{-1} &= -(t^*\Lambda_{1\uparrow}(0)v_k^* + t\Lambda_{1\downarrow}^*(0)u_k^*) + i(t^*\Lambda_{2\uparrow}(0)v_k^* + t\Lambda_{2\downarrow}^*(0)u_k^*) \\ t_{+1} &= -(t^*\Lambda_{1\uparrow}(0)v_k^* + t\Lambda_{1\downarrow}^*(0)u_k^*) - i(t^*\Lambda_{2\uparrow}(0)v_k^* + t\Lambda_{2\downarrow}^*(0)u_k^*). \end{aligned} \quad (C.7)$$

Next, we want to integrate out the s-wave superconducting lead, by dismissing the continuum of states and only keeping the BCS ground state. The corresponding projectors therefore are

$$P = |0\rangle_{\text{BCS}} |0\rangle_{\text{M}} \langle 0|_{\text{BCS}} \langle 0|_{\text{M}} + |0\rangle_{\text{BCS}} |1\rangle_{\text{M}} \langle 0|_{\text{BCS}} \langle 1|_{\text{M}} \quad (C.8)$$

$$Q = \sum_{n=0}^1 \sum_{k,\sigma} |k,\sigma\rangle_{\text{BCS}} |n\rangle_{\text{M}} \langle k,\sigma|_{\text{BCS}} \langle n|_{\text{M}}, \quad (C.9)$$

where  $P$  projects into the low energy space and  $Q$  into the high energy space. Here we define

$$|k,\sigma\rangle_{\text{BCS}} |1\rangle_{\text{M}} = \gamma_{k\sigma}^\dagger f^\dagger |0\rangle_{\text{BCS}} |0\rangle_{\text{M}}. \quad (C.10)$$

In order to calculate the Josephson current analytically we use the quasi-degenerate perturbation theory, where we assume the tunneling to be the small perturbation to the unperturbed Hamiltonian  $H_0 = H_{\text{BSC}} + H_{\text{M}}$ . Up to second order in the perturbation the effective low-energy Hamiltonian can be calculated as [214]

$$H = PH_0P + PH_TP + PH_T \frac{Q}{-H_0} H_TP. \quad (C.11)$$

---

For  $PH_0P$  we find in the basis of  $\{|0\rangle_{\text{BCS}}, |0\rangle_{\text{M}}, |0\rangle_{\text{BCS}}, |1\rangle_{\text{M}}\}$

$$PH_0P = \begin{pmatrix} -\varepsilon & 0 \\ 0 & \varepsilon \end{pmatrix}, \quad (\text{C.12})$$

and for  $PH_{\text{T}}\frac{Q}{-H_0}H_{\text{T}}P$  in the same basis

$$PH_{\text{T}}\frac{Q}{-H_0}H_{\text{T}}P = \begin{pmatrix} \sum_{k,\sigma} \frac{|t_{-\sigma}|^2}{-E_k} & 0 \\ 0 & \sum_{k,\sigma} \frac{|t_{+\sigma}|^2}{-E_k} \end{pmatrix}. \quad (\text{C.13})$$

The first order corrections vanish  $PH_{\text{T}}P = 0$ , because every tunneling event brings the low energy system into the high energy sector. By replacing the summation over the momentum in Eq (C.13) with an integration we find

$$\begin{aligned} PH_{\text{T}}\frac{Q}{-H_0}H_{\text{T}}P = & \quad (\text{C.14}) \\ & \begin{pmatrix} -i(\Lambda_{1\downarrow}(0)\Lambda_{2\uparrow}(0) - \Lambda_{1\uparrow}(0)\Lambda_{2\downarrow}(0))\Delta_{\text{eff}}e^{i\varphi} & 0 \\ 0 & i(\Lambda_{1\downarrow}(0)\Lambda_{2\uparrow}(0) - \Lambda_{1\uparrow}(0)\Lambda_{2\downarrow}(0))\Delta_{\text{eff}}e^{i\varphi} \end{pmatrix} \\ & + H.c. \end{aligned}$$

with

$$\Delta_{\text{eff}} = 2t^2\nu(0)|\Delta_{\text{BCS}}| \frac{2(\pi - \arctan(\frac{\varepsilon}{\sqrt{4|\Delta_{\text{BCS}}|^2 - \varepsilon^2}}))}{\sqrt{4|\Delta_{\text{BCS}}|^2 - \varepsilon^2}}. \quad (\text{C.15})$$

And finally in the limit of  $\Delta_{\text{BCS}} \rightarrow \infty$  we find

$$E_{e(o)}^{(2)} = \mp\varepsilon \pm 2\pi\nu(0) (it^2e^{i\varphi}[\Lambda_{1\uparrow}(0)\Lambda_{2\downarrow}(0) - \Lambda_{1\downarrow}(0)\Lambda_{2\uparrow}(0)] + c.c.). \quad (\text{C.16})$$





## D. Calculations of Majorana wave function

In the following, we want to calculate the spinor components for both MBS of a SOCNWs in order to relate the Josephson current to microscopic parameters. For the calculations we closely follow [152]. To start with, we consider a spin orbit coupled nanowire in proximity to a superconductor and an applied Zeeman field. Its BdG Hamiltonian in the Nambu basis is given as

$$H_{\text{BdG}} = \begin{pmatrix} -\frac{\hbar^2}{2m^*} \partial_x^2 - \mu + V_Z & -\alpha \partial_x & \Delta & 0 \\ \alpha \partial_x & -\frac{\hbar^2}{2m^*} \partial_x^2 - \mu - V_Z & 0 & \Delta \\ \Delta & 0 & \frac{\hbar^2}{2m^*} \partial_x^2 + \mu + V_Z & \alpha \partial_x \\ 0 & \Delta & -\alpha \partial_x & \frac{\hbar^2}{2m^*} \partial_x^2 + \mu - V_Z \end{pmatrix}$$

As we search for Majorana like solutions the hole-like and electron-like components of its wave function

$$\alpha^{(L,R)}(x) = \left( u_{\uparrow}^{(L,R)}(x), u_{\downarrow}^{(L,R)}(x), (v_{\downarrow}^{(L,R)})^*(x), -(v_{\uparrow}^{(L,R)})^*(x) \right)^T,$$

have to satisfy

$$(v_{\downarrow\uparrow}^{(L,R)})^* = \lambda u_{\downarrow\uparrow}^{(L,R)}, \quad (\text{D.1})$$

where  $\lambda = \pm 1$  for the left (L) and right (R) MBS and need to be zero energy solutions. Here, we denote the MBS with left and right for clarity. This reduces the four dimensional eigenvalue problem to a two dimensional problem

$$\begin{pmatrix} -\frac{\hbar^2}{2m} \partial_x^2 - \mu + V_Z & -\alpha \partial_x + \lambda \Delta \\ \alpha \partial_x - \lambda \Delta & -\frac{\hbar^2}{2m} \partial_x^2 - \mu - V_Z \end{pmatrix} \begin{pmatrix} u_{\uparrow}^{(L,R)}(x) \\ u_{\downarrow}^{(L,R)}(x) \end{pmatrix} = 0. \quad (\text{D.2})$$

We are now considering two kinds of solutions, a solution for the left MBS which decays exponentially for  $x > 0$  and a solution for the right MBS

## D. Calculations of Majorana wave function

---

at position  $L$  which exponentially decays in the other direction. However, the solutions of Eq. (D.2) which also satisfy the boundary conditions  $u_{\downarrow\uparrow}^{(L,R)}(0) = u_{\downarrow\uparrow}^{(L,R)}(L) = 0$  do not exist. So we consider two independent semi infinite nanowires which range from  $x = 0$  to  $x = \infty$  for the left MBS and from  $x = 0$  to  $x = -\infty$  for the right MBS which leads to the boundary conditions

$$\begin{aligned} u_{\sigma}^L(0) &= u_{\sigma}^L(\infty) = 0 \\ u_{\sigma}^R(0) &= u_{\sigma}^R(-\infty) = 0. \end{aligned} \quad (\text{D.3})$$

We use the ansatz

$$\begin{pmatrix} u_{\uparrow}^{(L,R)}(x) \\ u_{\downarrow}^{(L,R)}(x) \end{pmatrix} \propto \begin{pmatrix} u_{\uparrow}^{(L,R)} \\ u_{\downarrow}^{(L,R)} \end{pmatrix} e^{ax},$$

which leads to

$$\begin{aligned} &\left(\frac{\hbar^2}{2m}\right)^2 (a^{(L,R)})^4 + \left(\alpha^2 + \mu \frac{\hbar}{2m}\right) (a^{(L,R)})^2 \\ &+ 2\lambda\alpha\Delta a^{(L,R)} + \mu^2 + \Delta^2 - B^2 = 0. \end{aligned} \quad (\text{D.4})$$

For the anticipated decay, we need  $\text{Re}[a^L] < 0$  and  $\text{Re}[a^R] > 0$ . For the spinor components we find

$$\begin{pmatrix} u_{\uparrow}^{(L,R)} \\ u_{\downarrow}^{(L,R)} \end{pmatrix} \propto \begin{pmatrix} \frac{\hbar^2}{2m} (a^{(L,R)})^2 + B + \mu \\ a_i^{(L,R)} \alpha - \lambda \Delta \end{pmatrix}. \quad (\text{D.5})$$

For  $B^2 - \Delta^2 - \mu^2 > 0$ , so in the topologically non trivial regime, we find 3 solutions of Eq. (D.4) for both MBS which satisfy the restraints to their real parts. They can be parametrized as

$$\begin{aligned} a_{1/2}^{(L,R)} &= c_1^{(L,R)} \pm i c_2^{(L,R)}, \\ a_3^{(L,R)} &= -c_1^{(L,R)} + \sqrt{(c_1^{(L,R)})^2 + 4(B^2 - \Delta^2 - \mu^2)/((c_1^{(L,R)})^2 + (c_2^{(L,R)})^2)}, \end{aligned} \quad (\text{D.6})$$

---

where  $c_1^{(L,R)}$  and  $c_2^{(L,R)}$  are real valued. The wave functions of the MBS can then be written as

$$\begin{aligned}\Psi_{(L,R)}(x) &= \begin{pmatrix} u_{\uparrow}^{(L,R)}(x) \\ u_{\downarrow}^{(L,R)}(x) \end{pmatrix} \\ &= \sum_{i=1}^3 C_i^{(L,R)} \begin{pmatrix} \frac{\hbar^2}{2m} (a_i^{(L,R)})^2 + B + \mu \\ a_i^{(L,R)} \alpha - \lambda \Delta \end{pmatrix} e^{a_i^{(L,R)} x}\end{aligned}\quad (\text{D.7})$$

Here, the factors  $C_i^{(L,R)}$  follow from the boundary conditions Eqs. (D.3) (4 equations:  $\uparrow, \downarrow, R, L$ ) and normalization (2 equations:  $L, R$ ). To calculate the wave function at  $x = 0$  we neglect the solution corresponding to  $a_3^R$  for the right MBS, because  $|a_3^R|$  is larger than  $|\text{Re}(a_{1/2}^{(L,R)})|$ . The real and imaginary part of  $a_1^{(L,R)}$  then correspond to the Majorana localization length  $\xi$  and the wave number  $k_{F,\text{eff}}$ . To extract the spin canting angle of the MBS at  $x = 0$  we consider

$$\lim_{x \rightarrow 0} \frac{u_{\downarrow}^L(x)}{u_{\uparrow}^L(x)} = \tan\left(\frac{\Theta_1}{2}\right), \quad \frac{u_{\downarrow}^R(-L)}{u_{\uparrow}^R(-L)} = \tan\left(\frac{\Theta_2}{2}\right). \quad (\text{D.8})$$

The arctangent then reveals the spin canting angles of the MBS.



# References

- [1] R. P. Feynman, Int. J. Theor. Phys. **21**, 467 (1982).
- [2] F. Arute, K. Arya, R. Babbush, D. Bacon, J. C. Bardin, R. Barends, R. Biswas, S. Boixo, F. G. S. L. Brandao, D. A. Buell, B. Burkett, Y. Chen, Z. Chen, B. Chiaro, R. Collins, W. Courtney, A. Dunsworth, E. Farhi, B. Foxen, A. Fowler, C. Gidney, M. Giustina, R. Graff, K. Guerin, S. Habegger, M. P. Harrigan, M. J. Hartmann, A. Ho, M. Hoffmann, T. Huang, T. S. Humble, S. V. Isakov, E. Jeffrey, Z. Jiang, D. Kafri, K. Kechedzhi, J. Kelly, P. V. Klimov, S. Knysh, A. Korotkov, F. Kostritsa, D. Landhuis, M. Lindmark, E. Lucero, D. Lyakh, S. Mandrà, J. R. McClean, M. McEwen, A. Megrant, X. Mi, K. Michielsen, M. Mohseni, J. Mutus, O. Naaman, M. Neeley, C. Neill, M. Y. Niu, E. Ostby, A. Petukhov, J. C. Platt, C. Quintana, E. G. Rieffel, P. Roushan, N. C. Rubin, D. Sank, K. J. Satzinger, V. Smelyanskiy, K. J. Sung, M. D. Trevithick, A. Vainsencher, B. Villalonga, T. White, Z. J. Yao, P. Yeh, A. Zalcman, H. Neven, and J. M. Martinis, Nature **574**, 505 (2019).
- [3] J. Preskill, arxiv:1203.5813 (2012).
- [4] M. A. Nielsen and I. L. Chuang, *Quantum Computation and Quantum Information: 10th Anniversary Edition*, (Cambridge University Press, New York, NY, USA 2011), 10th edition.
- [5] D. P. DiVincenzo, Fortschr. Phys. **48**, 771 (2000).
- [6] D. Loss and D. P. DiVincenzo, Phys. Rev. A **57**, 120 (1998).
- [7] A. Imamoglu, D. D. Awschalom, G. Burkard, D. P. DiVincenzo, D. Loss, M. Sherwin, and A. Small, Phys. Rev. Lett. **83**, 4204 (1999).
- [8] D. G. Cory, A. F. Fahmy, and T. F. Havel, Proc. Natl. Acad. Sci. **94**, 1634 (1997).

## References

---

- [9] L. Childress and R. Hanson, MRS Bull. **38**, 134 (2013).
- [10] M. N. Leuenberger and D. Loss, Nature **410**, 789 (2001).
- [11] T. Hayashi, T. Fujisawa, H. D. Cheong, Y. H. Jeong, and Y. Hira-yama, Phys. Rev. Lett. **91**, 226804 (2003).
- [12] J. Koch, T. M. Yu, J. Gambetta, A. A. Houck, D. I. Schuster, J. Majer, A. Blais, M. H. Devoret, S. M. Girvin, and R. J. Schoelkopf, Phys. Rev. A **76**, 042319 (2007).
- [13] J. Clarke and F. K. Wilhelm, Nature **453**, 1031 (2008).
- [14] F. Jazaeri, A. Beckers, A. Tajalli, and J.-M. Sallese, arxiv:1908.02656 (2019).
- [15] J. K. Pachos, *Introduction to Topological Quantum Computation*, (Cambridge University Press 2012).
- [16] P. W. Shor, Phys. Rev. A **52**, R2493 (1995).
- [17] A. M. Steane, Phys. Rev. Lett. **77**, 793 (1996).
- [18] A. Y. Kitaev, Ann. Phys. **303**, 2 (2003).
- [19] S. Bravyi, M. B. Hastings, and S. Michalakis, J. Math. Phys. **51**, 093512 (2010).
- [20] S. Bravyi and A. Y. Kitaev, Phys. Rev. A **71**, 022316 (2005).
- [21] S. Das Sarma, M. Freedman, and C. Nayak, Phys. Rev. Lett. **94**, 166802 (2005).
- [22] C. Nayak, S. H. Simon, A. Stern, M. Freedman, and S. Das Sarma, Rev. Mod. Phys. **80**, 1083 (2008).
- [23] J. Alicea, Rep. Prog. Phys. **75**, 076501 (2012).
- [24] M. Leijnse and K. Flensberg, Semicond. Sci. Technol. **27**, 124003 (2012).
- [25] C. W. J. Beenakker, D. I. Pikulin, T. Hyart, H. Schomerus, and J. P. Dahlhaus, Phys. Rev. Lett. **110**, 017003 (2013).

- 
- [26] R. Aguado, RIV NUOVO CIMENTO **40**, 523 (2017).
- [27] R. M. Lutchyn, E. P. A. M. Bakkers, L. P. Kouwenhoven, P. Krogstrup, C. M. Marcus, and Y. Oreg, Nat. Rev. Mater. **3**, 52 (2018).
- [28] C. W. J. Beenakker, arxiv:1907.06497 (2019).
- [29] A. Y. Kitaev, Phys. Usp. **44**, 131 (2001).
- [30] The Nobel Prize in Physics 2016. NobelPrize.org. Nobel Media AB 2019. Sun. 27 Oct 2019. <<https://www.nobelprize.org/prizes/physics/2016/summary/>>.
- [31] B. A. Bernevig, *Topological Insulators and Topological Superconductors*, (Princeton University Press, Princeton 2013).
- [32] D. J. Thouless, M. Kohmoto, M. P. Nightingale, and M. den Nijs, Phys. Rev. Lett. **49**, 405 (1982).
- [33] M. Kohmoto, Ann. Phys. **160**, 343 (1985).
- [34] K. von Klitzing, Rev. Mod. Phys. **58**, 519 (1986).
- [35] J. E. Avron, R. Seiler, and B. Simon, Phys. Rev. Lett. **51**, 51 (1983).
- [36] A. P. Schnyder, S. Ryu, A. Furusaki, and A. W. W. Ludwig, Phys. Rev. B **78**, 195125 (2008).
- [37] C. L. Kane and E. J. Mele, Phys. Rev. Lett. **95**, 146802 (2005).
- [38] C. L. Kane and E. J. Mele, Phys. Rev. Lett. **95**, 226801 (2005).
- [39] B. A. Bernevig and S.-C. Zhang, Phys. Rev. Lett. **96**, 106802 (2006).
- [40] L. Fu, Phys. Rev. Lett. **106**, 106802 (2011).
- [41] Z. Song, Z. Fang, and C. Fang, Phys. Rev. Lett. **119**, 246402 (2017).
- [42] W. A. Benalcazar, B. A. Bernevig, and T. L. Hughes, Phys. Rev. B **96**, 245115 (2017).
- [43] J. Langbehn, Y. Peng, L. Trifunovic, F. von Oppen, and P. W. Brouwer, Phys. Rev. Lett. **119**, 246401 (2017).

## References

---

- [44] F. Schindler, A. M. Cook, M. G. Vergniory, Z. Wang, S. S. P. Parkin, B. A. Bernevig, and T. Neupert, *Sci. Adv.* **4** (2018).
- [45] N. P. Armitage, E. J. Mele, and A. Vishwanath, *Rev. Mod. Phys.* **90**, 015001 (2018).
- [46] P. G. de Gennes, *Superconductivity Of Metals And Alloys* -, (Avalon Publishing, New York 1999).
- [47] M. Tinkham, *Introduction to Superconductivity: Second Edition*, Dover Books on Physics, (Dover Publications 2004).
- [48] J. Bardeen, L. N. Cooper, and J. R. Schrieffer, *Phys. Rev.* **108**, 1175 (1957).
- [49] E. Majorana, *Nuovo Cimento* **14**, 171 (1937).
- [50] F. Wilczek, *Nat. Phys.* **5**, 614 (2009).
- [51] N. Read and D. Green, *Phys. Rev. B* **61**, 10267 (2000).
- [52] L. Fu and C. L. Kane, *Phys. Rev. Lett.* **100**, 096407 (2008).
- [53] R. M. Lutchyn, J. D. Sau, and S. Das Sarma, *Phys. Rev. Lett.* **105**, 077001 (2010).
- [54] Y. Oreg, G. Refael, and F. von Oppen, *Phys. Rev. Lett.* **105**, 177002 (2010).
- [55] S. Das Sarma, J. D. Sau, and T. D. Stanescu, *Phys. Rev. B* **86**, 220506 (2012).
- [56] H. J. Suominen, M. Kjaergaard, A. R. Hamilton, J. Shabani, C. J. Palmstrøm, C. M. Marcus, and F. Nichele, *Phys. Rev. Lett.* **119**, 176805 (2017).
- [57] M. Marganska, L. Milz, W. Izumida, C. Strunk, and M. Grifoni, *Phys. Rev. B* **97**, 075141 (2018).
- [58] T.-P. Choy, J. M. Edge, A. R. Akhmerov, and C. W. J. Beenakker, *Phys. Rev. B* **84**, 195442 (2011).



- 
- [59] S. Nadj-Perge, I. K. Drozdov, B. A. Bernevig, and A. Yazdani, *Phys. Rev. B* **88**, 020407 (2013).
- [60] J. Klinovaja, P. Stano, A. Yazdani, and D. Loss, *Phys. Rev. Lett.* **111**, 186805 (2013).
- [61] B. Braunecker and P. Simon, *Phys. Rev. Lett.* **111**, 147202 (2013).
- [62] M. M. Vazifeh and M. Franz, *Phys. Rev. Lett.* **111**, 206802 (2013).
- [63] F. Pientka, L. I. Glazman, and F. von Oppen, *Phys. Rev. B* **88**, 155420 (2013).
- [64] F. Pientka, A. Keselman, E. Berg, A. Yacoby, A. Stern, and B. I. Halperin, *Phys. Rev. X* **7**, 021032 (2017).
- [65] M. Hell, M. Leijnse, and K. Flensberg, *Phys. Rev. Lett.* **118**, 107701 (2017).
- [66] S. Park and P. Recher, *Phys. Rev. Lett.* **115**, 246403 (2015).
- [67] B. Jäck, Y. Xie, J. Li, S. Jeon, B. A. Bernevig, and A. Yazdani, *Science* **364**, 1255 (2019).
- [68] A. Murani, B. Dassonneville, A. Kasumov, J. Basset, M. Ferrier, R. Deblock, S. Guéron, and H. Bouchiat, *Phys. Rev. Lett.* **122**, 076802 (2019).
- [69] P. San-Jose, J. L. Lado, R. Aguado, F. Guinea, and J. Fernández-Rossier, *Phys. Rev. X* **5**, 041042 (2015).
- [70] S. Vaitiekenas, G. W. Winkler, B. van Heck, T. Karzig, M.-T. Deng, K. Flensberg, L. I. Glazman, C. Nayak, P. Krogstrup, R. M. Lutchyn, and C. M. Marcus, *Science* **367**, eaav3392 (2020).
- [71] F. Finocchiaro, F. Guinea, and P. San-Jose, *Phys. Rev. Lett.* **120**, 116801 (2018).
- [72] F. de Juan, J. H. Bardarson, and R. Ilan, *SciPost Phys.* **6**, 60 (2019).
- [73] H.-J. Kwon, V. M. Yakovenko, and K. Sengupta, *Low Temp. Phys.* **30**, 613 (2004).

## References

---

- [74] L. Fu and C. L. Kane, Phys. Rev. Lett. **102**, 216403 (2009).
- [75] D. I. Pikulin and Y. V. Nazarov, Phys. Rev. B **86**, 140504 (2012).
- [76] D. Rainis, L. Trifunovic, J. Klinovaja, and D. Loss, Phys. Rev. B **87**, 024515 (2013).
- [77] P. San-Jose, E. Prada, and R. Aguado, Phys. Rev. Lett. **108**, 257001 (2012).
- [78] M. Houzet, J. S. Meyer, D. M. Badiane, and L. I. Glazman, Phys. Rev. Lett. **111**, 046401 (2013).
- [79] P. Virtanen and P. Recher, Phys. Rev. B **88**, 144507 (2013).
- [80] J. Cayao, P. San-Jose, A. M. Black-Schaffer, R. Aguado, and E. Prada, Phys. Rev. B **96**, 205425 (2017).
- [81] J. Cayao, A. M. Black-Schaffer, E. Prada, and R. Aguado, Beilstein J. Nanotechnol. **9**, 1339 (2018).
- [82] L. P. Rokhinson, X. Liu, and J. K. Furdyna, Nat. Phys. **8**, 795 (2012).
- [83] E. Bocquillon, R. S. Deacon, J. Wiedenmann, P. Leubner, T. M. Klapwijk, C. Brüne, K. Ishibashi, H. Buhmann, and L. W. Molenkamp, Nat. Nanotechnol. **12**, 137 (2016).
- [84] J. Wiedenmann, E. Bocquillon, R. S. Deacon, S. Hartinger, O. Herrmann, T. M. Klapwijk, L. Maier, C. Ames, C. Brüne, C. Gould, A. Oiwa, K. Ishibashi, S. Tarucha, H. Buhmann, and L. W. Molenkamp, Nat. Commun. **7**, 10303 (2016).
- [85] E. Bocquillon, J. Wiedenmann, R. S. Deacon, T. M. Klapwijk, H. Buhmann, and L. W. Molenkamp, in *Topological Matter*, (Springer International Publishing 2018), 115–148.
- [86] F. Domínguez, F. Hassler, and G. Platero, Phys. Rev. B **86**, 140503 (2012).

- 
- [87] F. Domínguez, O. Kashuba, E. Bocquillon, J. Wiedenmann, R. S. Deacon, T. M. Klapwijk, G. Platero, L. W. Molenkamp, B. Trauzettel, and E. M. Hankiewicz, *Phys. Rev. B* **95**, 195430 (2017).
- [88] J. Picó-Cortés, F. Domínguez, and G. Platero, *Phys. Rev. B* **96**, 125438 (2017).
- [89] R. S. Deacon, J. Wiedenmann, E. Bocquillon, F. Domínguez, T. M. Klapwijk, P. Leubner, C. Brüne, E. M. Hankiewicz, S. Tarucha, K. Ishibashi, H. Buhmann, and L. W. Molenkamp, *Phys. Rev. X* **7**, 021011 (2017).
- [90] D. Laroche, D. Bouman, D. J. van Woerkom, A. Proutski, C. Murthy, D. I. Pikulin, C. Nayak, R. J. J. van Gulik, J. Nygård, P. Krogstrup, L. P. Kouwenhoven, and A. Geresdi, *Nat. Commun.* **10**, 245 (2019).
- [91] F. Zhang and C. L. Kane, *Phys. Rev. Lett.* **113**, 036401 (2014).
- [92] P. Fendley, *J. Stat. Mech. Theor. Exp.* **2012**, P11020 (2012).
- [93] N. H. Lindner, E. Berg, G. Refael, and A. Stern, *Phys. Rev. X* **2**, 041002 (2012).
- [94] J. Alicea and P. Fendley, *Annu. Rev. Condens. Matter Phys.* **7**, 119 (2016).
- [95] C. J. Bolech and E. Demler, *Phys. Rev. Lett.* **98**, 237002 (2007).
- [96] K. Law, P. Lee, and T. Ng, *Phys. Rev. Lett.* **103**, 237001 (2009).
- [97] K. Flensberg, *Phys. Rev. B* **82**, 180516 (2010).
- [98] V. Mourik, K. Zuo, S. M. Frolov, S. R. Plissard, E. P. A. M. Bakkers, and L. P. Kouwenhoven, *Science* **336**, 1003 (2012).
- [99] M. T. Deng, C. L. Yu, G. Y. Huang, M. Larsson, P. Caroff, and H. Q. Xu, *Nano Lett.* **12**, 6414 (2012).
- [100] A. Das, Y. Ronen, Y. Most, Y. Oreg, M. Heiblum, and H. Shtrikman, *Nat. Phys.* **8**, 887 (2012).

## References

---

- [101] H. O. H. Churchill, V. Fatemi, K. Grove-Rasmussen, M. T. Deng, P. Caroff, H. Q. Xu, and C. M. Marcus, *Phys. Rev. B* **87**, 241401 (2013).
- [102] A. D. K. Finck, D. J. Van Harlingen, P. K. Mohseni, K. Jung, and X. Li, *Phys. Rev. Lett.* **110**, 126406 (2013).
- [103] E. J. H. Lee, X. Jiang, M. Houzet, R. Aguado, C. M. Lieber, and S. D. Franceschi, *Nat. Nanotechnol.* **9**, 79 (2013).
- [104] S. Nadj-Perge, I. K. Drozdov, J. Li, H. Chen, S. Jeon, J. Seo, A. H. MacDonald, B. A. Bernevig, and A. Yazdani, *Science* **346**, 602 (2014).
- [105] R. Pawlak, M. Kisiel, J. Klinovaja, T. Meier, S. Kawai, T. Glatzel, D. Loss, and E. Meyer, *npj Quantum Inf* **2**, 16035 (2016).
- [106] M. T. Deng, S. Vaitiekėnas, E. B. Hansen, J. Danon, M. Leijnse, K. Flensberg, J. Nygård, P. Krogstrup, and C. M. Marcus, *Science* **354**, 1557 (2016).
- [107] J. Chen, P. Yu, J. Stenger, M. Hoesl, D. Car, S. R. Plissard, E. P. A. M. Bakkers, T. D. Stanescu, and S. M. Frolov, *Sci. Adv.* **3**, e1701476 (2017).
- [108] S. Jeon, Y. Xie, J. Li, Z. Wang, B. A. Bernevig, and A. Yazdani, *Science* **358**, 772 (2017).
- [109] F. Nichele, A. C. C. Drachmann, A. M. Whiticar, E. C. T. O'Farrell, H. J. Suominen, A. Fornieri, T. Wang, G. C. Gardner, C. Thomas, A. T. Hatke, P. Krogstrup, M. J. Manfra, K. Flensberg, and C. M. Marcus, *Phys. Rev. Lett.* **119**, 136803 (2017).
- [110] M. Ruby, B. W. Heinrich, Y. Peng, F. von Oppen, and K. J. Franke, *Nano Lett.* **17**, 4473 (2017).
- [111] Önder Gül, H. Zhang, J. D. S. Bommer, M. W. A. de Moor, D. Car, S. R. Plissard, E. P. A. M. Bakkers, A. Geresdi, K. Watanabe, T. Taniguchi, and L. P. Kouwenhoven, *Nat. Nanotechnol.* **13**, 192 (2018).

- 
- [112] J. E. Sestoft, T. Kanne, A. N. Gejl, M. von Soosten, J. S. Yodh, D. Sherman, B. Tarasinski, M. Wimmer, E. Johnson, M. Deng, J. Nygård, T. S. Jespersen, C. M. Marcus, and P. Krogstrup, *Phys. Rev. Mater.* **2**, 044202 (2018).
  - [113] M.-T. Deng, S. Vaitiekėnas, E. Prada, P. San-Jose, J. Nygård, P. Krogstrup, R. Aguado, and C. M. Marcus, *Phys. Rev. B* **98**, 085125 (2018).
  - [114] H. Zhang, C.-X. Liu, S. Gazibegovic, D. Xu, J. A. Logan, G. Wang, N. van Loo, J. D. S. Bommer, M. W. A. de Moor, D. Car, R. L. M. O. het Veld, P. J. van Veldhoven, S. Koelling, M. A. Verheijen, M. Pendharkar, D. J. Pennachio, B. Shojaei, J. S. Lee, C. J. Palmstrøm, E. P. A. M. Bakkers, S. D. Sarma, and L. P. Kouwenhoven, *Nature* **556**, 74 (2018).
  - [115] J. Nilsson, A. Akhmerov, and C. W. J. Beenakker, *Phys. Rev. Lett* **101**, 120403 (2008).
  - [116] L. Weithofer, P. Recher, and T. L. Schmidt, *Phys. Rev. B* **90**, 205416 (2014).
  - [117] Y.-H. Lai, J. D. Sau, and S. Das Sarma, *Phys. Rev. B* **100**, 045302 (2019).
  - [118] H. Zhang, D. E. Liu, M. Wimmer, and L. P. Kouwenhoven, *Nat. Commun.* **10**, 5128 (2019).
  - [119] L. Fu, *Phys. Rev. Lett.* **104** (2010).
  - [120] S. M. Albrecht, A. P. Higginbotham, M. Madsen, F. Kuemmeth, T. S. Jespersen, J. Nygård, P. Krogstrup, and C. M. Marcus, *Nature* **531**, 206 (2016).
  - [121] D. A. Ivanov, *Phys. Rev. Lett* **86**, 268 (2001).
  - [122] A. Stern, F. von Oppen, and E. Mariani, *Phys. Rev. B* **70**, 205338 (2004).
  - [123] J. Alicea, Y. Oreg, G. Refael, F. von Oppen, and M. P. A. Fisher, *Nat. Phys.* **7**, 412 (2011).

## References

---

- [124] C. Tutschku, R. W. Reinthaler, C. Lei, A. H. MacDonald, and E. M. Hankiewicz, *Phys. Rev. B* **102**, 125407 (2020).
- [125] S. Park, H.-S. Sim, and P. Recher, *arxiv:1812.09573* (2018).
- [126] P. Bonderson, M. Freedman, and C. Nayak, *Phys. Rev. Lett.* **101**, 010501 (2008).
- [127] S. Vijay and L. Fu, *Phys. Rev. B* **94**, 235446 (2016).
- [128] F. Hassler, A. R. Akhmerov, and C. W. J. Beenakker, *New J. of Phys.* **13**, 095004 (2011).
- [129] B. van Heck, A. R. Akhmerov, F. Hassler, M. Burrello, and C. W. J. Beenakker, *New J. of Phys.* **14**, 035019 (2012).
- [130] S. D. Sarma, M. Freedman, and C. Nayak, *npj Quantum Inf.* **1**, 15001 (2015).
- [131] D. J. Clarke, J. D. Sau, and S. Das Sarma, *Phys. Rev. X* **6**, 021005 (2016).
- [132] T. Karzig, Y. Oreg, G. Refael, and M. H. Freedman, *Phys. Rev. X* **6**, 031019 (2016).
- [133] S. B. Bravyi and A. Y. Kitaev, *Ann. Phys.* **298**, 210 (2002).
- [134] S. Bravyi, *Phys. Rev. A* **73**, 042313 (2006).
- [135] C. W. J. Beenakker, D. P. DiVincenzo, C. Emary, and M. Kindermann, *Phys. Rev. Lett.* **93**, 020501 (2004).
- [136] O. Zilberberg, B. Braunecker, and D. Loss, *Phys. Rev. A* **77**, 012327 (2008).
- [137] C. Knapp, M. Zaletel, D. E. Liu, M. Cheng, P. Bonderson, and C. Nayak, *Phys. Rev. X* **6**, 041003 (2016).
- [138] A. Schuray, L. Weithofer, and P. Recher, *Phys. Rev. B* **96**, 085417 (2017).
- [139] A. Schuray, M. Rammler, and P. Recher, *Phys. Rev. B* **102**, 045303 (2020).

- [140] A. Schuray, A. L. Yeyati, and P. Recher, Phys. Rev. B **98**, 235301 (2018).
- [141] C. Moore, T. D. Stanescu, and S. Tewari, Phys. Rev. B **97**, 165302 (2018).
- [142] A. Vuik, B. Nijholt, A. R. Akhmerov, and M. Wimmer, SciPost Phys. **7**, 61 (2019).
- [143] C. Moore, C. Zeng, T. D. Stanescu, and S. Tewari, Phys. Rev. B **98**, 155314 (2018).
- [144] C. Reeg, O. Dmytruk, D. Chevallier, D. Loss, and J. Klinovaja, Phys. Rev. B **98**, 245407 (2018).
- [145] B. D. Woods, J. Chen, S. M. Frolov, and T. D. Stanescu, Phys. Rev. B **100**, 125407 (2019).
- [146] J. Chen, B. D. Woods, P. Yu, M. Hocevar, D. Car, S. R. Plissard, E. P. A. M. Bakkers, T. D. Stanescu, and S. M. Frolov, Phys. Rev. Lett. **123**, 107703 (2019).
- [147] **2**, 575 (2020).
- [148] R. Hanson, L. P. Kouwenhoven, J. R. Petta, S. Tarucha, and L. M. K. Vandersypen, Rev. Mod. Phys. **79**, 1217 (2007).
- [149] D. E. Liu and H. U. Baranger, Phys. Rev. B **84**, 201308 (2011).
- [150] M. Leijnse and K. Flensberg, Phys. Rev. B **84**, 140501 (2011).
- [151] E. Vernek, P. H. Penteado, A. C. Seridonio, and J. C. Egues, Phys. Rev. B **89**, 165314 (2014).
- [152] E. Prada, R. Aguado, and P. San-Jose, Phys. Rev. B **96**, 085418 (2017).
- [153] D. J. Clarke, Phys. Rev. B **96**, 201109 (2017).
- [154] A. Ptok, A. Kobiałka, and T. Domański, Phys. Rev. B **96**, 195430 (2017).

## References

---

- [155] D. Chevallier, P. Szumniak, S. Hoffman, D. Loss, and J. Klinovaja, Phys. Rev. B **97**, 045404 (2018).
- [156] C. Fleckenstein, F. Domínguez, N. Traverso Ziani, and B. Trauzettel, Phys. Rev. B **97**, 155425 (2018).
- [157] U. Fano, Phys. Rev. **124**, 1866 (1961).
- [158] A. E. Miroshnichenko, S. Flach, and Y. S. Kivshar, Rev. Mod. Phys. **82**, 2257 (2010).
- [159] J. Göres, D. Goldhaber-Gordon, S. Heemeyer, M. A. Kastner, H. Shtrikman, D. Mahalu, and U. Meirav, Phys. Rev. B **62**, 2188 (2000).
- [160] F. A. Dessotti, L. S. Ricco, M. de Souza, F. M. Souza, and A. C. Seridonio, J. Appl. Phys. **116**, 173701 (2014).
- [161] J.-J. Xia, S.-Q. Duan, and W. Zhang, Nanoscale Res. Lett. **10**, 223 (2015).
- [162] J. Barański, A. Kobińska, and T. Domański, J. Phys. Condens. Matter **29**, 075603 (2016).
- [163] Y. Xiong, Chinese Phys. Lett. **33**, 057402 (2016).
- [164] A. Ueda and T. Yokoyama, Phys. Rev. B **90**, 081405 (2014).
- [165] C. Jiang and Y.-S. Zheng, Solid State Commun. **212**, 14 (2015).
- [166] Q.-B. Zeng, S. Chen, L. You, and R. Lü, Front. Phys. **12**, 127302 (2016).
- [167] L. S. Levitov and M. Reznikov, Phys. Rev. B **70**, 115305 (2004).
- [168] A. Schuray, *Full counting statistics in Majorana fermion networks*, Master's thesis, TU Braunschweig, Braunschweig (2016).
- [169] U. Fano, Nuovo Cimento **12**, 154 (1935).
- [170] F. Peñaranda, R. Aguado, P. San-Jose, and E. Prada, Phys. Rev. B **98**, 235406 (2018).



- [171] E. Prada, P. San-Jose, and R. Aguado, *Phys. Rev. B* **86**, 180503 (2012).
- [172] C.-X. Liu, J. D. Sau, T. D. Stanescu, and S. Das Sarma, *Phys. Rev. B* **96**, 075161 (2017).
- [173] C. Reeg, O. Dmytruk, D. Chevallier, D. Loss, and J. Klinovaja, *Phys. Rev. B* **98**, 245407 (2018).
- [174] J. Avila, F. Peñaranda, E. Prada, P. San-Jose, and R. Aguado, *Commun. Phys.* **2**, 133 (2019).
- [175] T. D. Stanescu and S. Tewari, *Phys. Rev. B* **100**, 155429 (2019).
- [176] G. Kells, D. Meidan, and P. W. Brouwer, *Phys. Rev. B* **86**, 100503 (2012).
- [177] T. D. Stanescu and S. Tewari, *Phys. Rev. B* **87**, 140504 (2013).
- [178] Q. Liu, C. Chen, T. Zhang, R. Peng, Y.-J. Yan, C.-H.-P. Wen, X. Lou, Y.-L. Huang, J.-P. Tian, X.-L. Dong, G.-W. Wang, W.-C. Bao, Q.-H. Wang, Z.-P. Yin, Z.-X. Zhao, and D.-L. Feng, *Phys. Rev. X* **8**, 041056 (2018).
- [179] E. Prada, P. San-Jose, M. W. A. de Moor, A. Geresdi, E. J. H. Lee, J. Klinovaja, D. Loss, J. Nygård, R. Aguado, and L. P. Kouwenhoven, 1911.04512 (2019).
- [180] D. Sticlet, C. Bena, and P. Simon, *Phys. Rev. Lett.* **108**, 096802 (2012).
- [181] M. Serina, D. Loss, and J. Klinovaja, *Phys. Rev. B* **98**, 035419 (2018).
- [182] L. Milz, W. Izumida, M. Grifoni, and M. Marganska, *Phys. Rev. B* **100**, 155417 (2019).
- [183] G. L. R. Anselmetti, E. A. Martinez, G. C. Ménard, D. Puglia, F. K. Malinowski, J. S. Lee, S. Choi, M. Pendharkar, C. J. Palmstrøm, C. M. Marcus, L. Casparis, and A. P. Higginbotham, *Phys. Rev. B* **100**, 205412 (2019).

## References

---

- [184] A. Grivnin, E. Bor, M. Heiblum, Y. Oreg, and H. Shtrikman, *Nat. Commun.* **10**, 1940 (2019).
- [185] G. C. Ménard, A. Mesaros, C. Brun, F. Debontridder, D. Roditchev, P. Simon, and T. Cren, *Nat. Commun.* **10**, 2587 (2019).
- [186] A. Martín-Rodero and A. L. Yeyati, *Adv. Phys.* **60**, 899 (2011).
- [187] Y. V. Nazarov and M. Kindermann, *Eur. Phys. J. B* **35**, 413 (2003).
- [188] C. Ren, Y. Wu, M. Sun, S. Wang, and H. Tian, *J. Phys. Condens. Matter* **31**, 045501 (2018).
- [189] C. W. Groth, M. Wimmer, A. R. Akhmerov, and X. Waintal, *New J. Phys.* **16**, 063065 (2014).
- [190] J. Klinovaja and D. Loss, *Phys. Rev. B* **86**, 085408 (2012).
- [191] B. Josephson, *Physics Letters* **1**, 251 (1962).
- [192] B. Josephson, *Advances in Physics* **14**, 419 (1965).
- [193] S. Shapiro, *Phys. Rev. Lett.* **11**, 80 (1963).
- [194] J. D. Sau and F. Setiawan, *Phys. Rev. B* **95**, 060501 (2017).
- [195] D. M. Badiane, M. Houzet, and J. S. Meyer, *Phys. Rev. Lett.* **107**, 177002 (2011).
- [196] A. Zazunov, R. Egger, and A. L. Yeyati, *Phys. Rev. B* **94**, 014502 (2016).
- [197] Y. Peng, F. Pientka, Y. Vinkler-Aviv, L. I. Glazman, and F. von Oppen, *Phys. Rev. Lett.* **115**, 266804 (2015).
- [198] G. Sharma and S. Tewari, *Phys. Rev. B* **93**, 195161 (2016).
- [199] F. Setiawan, W. S. Cole, J. D. Sau, and S. Das Sarma, *Phys. Rev. B* **95**, 020501 (2017).
- [200] F. Setiawan, W. S. Cole, J. D. Sau, and S. Das Sarma, *Phys. Rev. B* **95**, 174515 (2017).

- [201] M. Ruby, F. Pientka, Y. Peng, F. von Oppen, B. W. Heinrich, and K. J. Franke, *Phys. Rev. Lett.* **115**, 197204 (2015).
- [202] A. Zazunov and R. Egger, *Phys. Rev. B* **85**, 104514 (2012).
- [203] A. Zazunov, R. Egger, M. Alvarado, and A. L. Yeyati, *Phys. Rev. B* **96**, 024516 (2017).
- [204] C. Schrade and L. Fu, *Phys. Rev. Lett.* **120**, 267002 (2018).
- [205] P. A. Ioselevich, P. M. Ostrovsky, and M. V. Feigel'man, *Phys. Rev. B* **93**, 125435 (2016).
- [206] A. Zazunov, A. Iks, M. Alvarado, A. L. Yeyati, and R. Egger, *Beilstein J. Nanotechnol.* **9**, 1659 (2018).
- [207] J. Cayao and A. M. Black-Schaffer, *Eur. Phys. J.-Spec. Top.* **227**, 1387 (2018).
- [208] N. N. Bogoliubov, *Nuovo Cimento (1955-1965)* **7**, 794 (1958).
- [209] J. G. Valatin, *Nuovo Cimento (1955-1965)* **7**, 843 (1958).
- [210] S. D. Escribano, A. L. Yeyati, and E. Prada, *Beilstein J. Nanotechnol.* **9**, 2171 (2018).
- [211] E. C. T. O'Farrell, A. C. C. Drachmann, M. Hell, A. Fornieri, A. M. Whiticar, E. B. Hansen, S. Gronin, G. C. Gardner, C. Thomas, M. J. Manfra, K. Flensberg, C. M. Marcus, and F. Nichele, *Phys. Rev. Lett.* **121**, 256803 (2018).
- [212] M. Swanson, *Path Integrals and Quantum Processes*, Dover Books on Physics, (Dover Publications, Mineola 2014).
- [213] A. Kamenev, *Field Theory of Non-Equilibrium Systems*, (Cambridge University Press, New York 2011).
- [214] F. H. L. Essler, H. Frahm, F. Göhmann, A. Klümper, and V. E. Korepin, *The One-Dimensional Hubbard Model*, (Cambridge University Press, Cambridge 2005).